Exciton-polariton Bose-Einstein condensation

Hui Deng

Department of Physics, University of Michigan, Ann Arbor, Michigan 48109, USA

Hartmut Haug

Institut für Theoretische Physik, Goethe Universität Frankfurt, Max-von-Laue-Street 1, D-60438 Frankfurt am Main, Germany

Yoshihisa Yamamoto

Edward L. Ginzton Laboratory, Stanford University, Stanford, California 94305, USA; National Institute of Informatics, Hitotsubashi, Chiyoda-ku, Tokyo 101-8430, Japan; and NTT Basic Research Laboratories, NTT Corporation, Atsugi, Kanagawa 243-0198, Japan

(Published 12 May 2010)

In the past decade, a two-dimensional matter-light system called the microcavity exciton-polariton has emerged as a new promising candidate of Bose-Einstein condensation (BEC) in solids. Many pieces of important evidence of polariton BEC have been established recently in GaAs and CdTe microcavities at the liquid helium temperature, opening a door to rich many-body physics inaccessible in experiments before. Technological progress also made polariton BEC at room temperatures promising. In parallel with experimental progresses, theoretical frameworks and numerical simulations are developed, and our understanding of the system has greatly advanced. In this article, recent experiments and corresponding theoretical pictures based on the Gross-Pitaevskii equations and the Boltzmann kinetic simulations for a finite-size BEC of polaritons are reviewed.

DOI: 10.1103/RevModPhys.82.1489 PACS number(s): 71.35.Lk, 71.36.+c, 42.50.−p, 78.67.−n

CONTENTS

I. INTRODUCTION

The experimental technique of controlling spontaneous emission of an atom by a cavity is referred to as cavity quantum electrodynamics. It has been studied for a variety of atomic systems (Berman, 1994). In solids, the inhibited and enhanced spontaneous emission was observed for two-dimensional (2D) quantum well (QW) excitons in semiconductor planar microcavities (Yamamoto *et al.*, 1989; Björk *et al.*, 1991). Due to a very strong collective dipole interaction between QW excitons and microcavity photon fields, even with a relatively low-Q cavity, the planar microcavity system features a reversible spontaneous emission and thus normal-mode splitting into an upper and lower branches of polaritons (Weisbuch *et al.*, 1992).[1]

The metastable state of lower polaritons at zero in-plane momentum ($k_{\|}=0$) has recently emerged as a new candidate for observing Bose-Einstein condensation (BEC) in solids (Imamoglu *et al.*, 1996).[2] The experimental advantage of polariton BEC over conventional exciton BEC (Hanamura and Haug, 1977) is twofold. Near $k_{\|}=0$, a polariton has an effective mass of four orders of magnitude lighter than a bare exciton mass, so the critical temperature for reaching polariton BEC is four orders of magnitude higher than that for reaching exciton BEC at the same particle density or equivalently the critical density for reaching polariton BEC is four orders of magnitude lower than that for reaching exciton BEC at the same temperature. The second advantage of this system is that a polariton can easily extend a phase-coherent wave function in space through its photonic component in spite of unavoidable crystal defects and disorders, while a bare exciton is easily localized in a fluctuating potential inside a crystal, which is a notorious enemy to the exciton BEC.

Polaritons have a very short lifetime due to fast photon leakage rate from a microcavity. In most cases, polaritons have a lifetime shorter than the cooling time to the metastable ground state, so that the system remains in a nonequilibrium condition without a well-defined temperature or chemical potential. However, when the cavity-photon resonance is detuned to higher than that of the QW exciton (blue detuning), the lower polariton (LP) has an increased excitonic component, a longer lifetime, and a shorter cooling time, facilitating thermalization. In the limit of a very large blue detuning, the dynamical polariton laser becomes indistinguishable from the thermal-equilibrium exciton BEC. In a recent experiment, a quantum degenerate polariton gas was observed with a chemical potential μ well within the BEC regime, $-\mu/k_BT<0.1$, and at a polariton gas temperature T very close to the lattice (phonon reservoir) temperature of ~4 K (Deng *et al.*, 2006). The excitonic component of polaritons in this experiment is up to 80%. However, the system is still metastable and the quantum degenerate gas exists only for several tens of picoseconds.

The dynamical nature of a polariton condensate places a limitation for studying the standard BEC physics, but it also provides a new experimental tool for studying a nonequilibrium open system consisting of highly degenerate interacting bosons. This is not an easily accessible problem by atomic BEC or superfluid ^{4}He systems. One unique feature of a polariton system, compared to dilute atomic BEC and dense superfluid ^{4}He, is

[1]Since we discuss exclusively exciton polaritons in semiconductors, we abbreviate exciton-polariton as polariton in this paper.

[2]The metastable state of upper polaritons at $k_{\|}=0$ in principle may also undergo BEC. But the fast scattering from the upper to the lower branch makes such a condensation unlikely.

the direct experimental accessibility to the quantum-statistical properties of the condensate. The main decay channel of polaritons is the photon leakage from a cavity in which the energy and in-plane momentum are conserved between an annihilated polariton and a created photon. Through various quantum optical measurements on the leakage photon field, we can easily study the quantum nature of the polariton condensate.

Various signatures of phase transition have been experimentally established in GaAs (Deng *et al.*, 2002, 2003, 2007; Balili *et al.*, 2007; Lai *et al.*, 2007) and CdTe (Richard *et al.*, 2005; Kasprzak *et al.*, 2006, 2008) microcavities. In parallel with the experimental progress, theoretical studies and numerical simulations are developed for describing the thermodynamics (Doan *et al.*, 2005; Sarchi and Savona, 2007a), modified excitation spectrum (Szymanska *et al.*, 2006; Wouters and Carusotto, 2007), spin dynamics (Kavokin *et al.*, 2004; Cao *et al.*, 2008), and particle-particle interactions (Cao *et al.*, 2008) of polariton condensates. Our understanding of the system has greatly advanced in the past few years.

In this article, we review the recent progress on experimental and theoretical studies of polariton condensates. A comprehensive review on theoretical modeling of the polariton system can be found in Keeling *et al.* (2007). Here we adopt the model that treats the polaritons as weakly interacting bosons. The model is valid when the exciton density is well below the Mott transition density and is applicable to most of the experiments on polariton condensation. Since we focus on spontaneous coherence and thermodynamic quantum phase of polaritons, we exclude from the current review the subject of polariton parametric amplification which has been reviewed by, e.g., Ciuti *et al.* (2003) and Keeling *et al.* (2007).

This article is organized as follows. Section II introduces microcavity polaritons, their properties relevant for BEC research, common experimental methodologies, and theoretical tools. In Sec. III, we review the microscopic theory of nonlinear interactions among polaritons and formulate the rate equations of isospin polariton kinetics. Numerical simulations based on these rate equations are used to understand the experiments reviewed in Secs. IV, V, and VII. Section IV reviews cold collision experiments that validate treating polaritons as a dilute Bose gas and reveal polariton-polariton scattering as the microscopic driving force of polariton dynamics. Thermodynamics of polariton condensates, such as relaxation and cooling of the polaritons, and temporal changes of gas temperatures and chemical potential are presented in Sec. V. Section VI extends the theory to include the spin degrees of freedom and reviews the related experiments. Section VII reviews measurements of the coherence functions of polariton condensates, including the first- and second-order temporal coherence and the first-order spatial coherence. Section VIII introduces the Gross-Pitaevskii (GP) equation and applies it to experiments on the ground-state energy, quantum depletion spectra, and vortices of polariton condensates. Finally, the condensation dynamics of polaritons in a single isolated trap and one-dimensional array of traps are presented in Sec. IX. A minimum uncertainty wave packet close to the Heisenberg limit and competition between the *s*- and *p*-orbital superfluid states have been observed. We conclude with some future prospects of the field in Sec. X.

II. SEMICONDUCTOR MICROCAVITY POLARITONS

A "microcavity polariton" is a quasiparticle resulting from strong coupling between matter and light. The "matter" component is a Wannier-Mott exciton consisting of a bound pair of electron and hole. The "light" component is a strongly confined photon field in a semiconductor microcavity. Half-matter, half-light microcavity polaritons emerged as a unique solid-state candidate for research on phase-transition physics, as discussed in this section.

A. Wannier-Mott exciton

A solid consists of 10^{23} atoms. Instead of describing the 10^{23} atoms and their constituents in full detail, the common approaches are to treat the stable ground state of an isolated system as a quasivacuum and to introduce quasiparticles as units of elementary excitations, which only weakly interact with each other. An exciton is a typical example of such a quasiparticle, consisting of an electron and a hole bound by the Coulomb interaction. The quasivacuum of a semiconductor is the state with filled valence band and empty conduction band. When an electron with charge $-e$ is excited from the valence band into the conduction band, the vacancy it leaves in the valence band can be described as a quasiparticle called a "hole." A hole in the valence band has charge $+e$ and an effective mass defined by $-(\partial^2 E/\partial p^2)^{-1}$, E and p denoting the energy and momentum of the hole. A hole and an electron at $p \sim 0$ interact with each other via Coulomb interaction and form a bound pair (an exciton) analogous to a hydrogen atom where an electron is bound to a proton. However, due to the strong dielectric screening in solids and a small effective-mass ratio of the hole to the electron, the binding energy of a semiconductor exciton is on the order of 10–100 meV and its Bohr radius is about 10–100 Å, extending over tens of atomic sites in the crystal (Hanamura and Haug, 1977).

If we define the creation operator of a conduction-band electron of momentum $\boldsymbol{k}$ as $\hat{a}_{\boldsymbol{k}}^{\dagger}$ and a valence-band hole as $\hat{b}_{\boldsymbol{k}}^{\dagger}$, the exciton creation operator can be defined as

$$\hat{e}_{\boldsymbol{K},n}^{\dagger} = \sum_{\boldsymbol{k},\boldsymbol{k}'} \delta_{\boldsymbol{K},\boldsymbol{k}+\boldsymbol{k}'} \phi_n\left(\frac{m_h \boldsymbol{k} - m_e \boldsymbol{k}'}{m_e + m_h}\right) \hat{a}_{\boldsymbol{k}}^{\dagger} \hat{b}_{\boldsymbol{k}'}^{\dagger}. \tag{1}$$

Here m_e and m_h are the electron and hole mass, respectively; $\boldsymbol{K}$ is the center-of-mass momentum of the exciton; $\phi_n(\boldsymbol{k})$ is the wave function of the relative motion of an electron and a hole, which takes the same form as that of an electron and a proton in a hydrogen atom; and n is the quantum number of the relative motion. The exciton

operators obey the following commutation relations:

$$[\hat{e}_{\boldsymbol{K}',n'},\hat{e}_{\boldsymbol{K},n}]=0,$$

$$[\hat{e}^{\dagger}_{\boldsymbol{K}',n'},\hat{e}^{\dagger}_{\boldsymbol{K},n}]=0, \tag{2}$$

$$[\hat{e}_{\boldsymbol{K}',n'},\hat{e}^{\dagger}_{\boldsymbol{K},n}]=\delta_{\boldsymbol{K}\boldsymbol{K}'}\delta_{nn'}-O(n_{\mathrm{exc}}a_B^3).$$

Hence excitons can be considered as bosons when the exciton interparticle spacing is much larger than its Bohr radius: $n_{\mathrm{exc}}\ll a_B^{-3}$.

1. Exciton optical transition

The electron and hole in an exciton form a dipole that interacts with electromagnetic fields of light. The interaction strength with light at angular frequency ω is conventionally described by the exciton oscillator strength f,

$$f=\frac{2m^*\omega}{\hbar}|\langle u_v|\boldsymbol{r}\cdot\boldsymbol{e}|u_c\rangle|^2\frac{V}{\pi a_B^3}. \tag{3}$$

Here $m^*=(m_e^{-1}+m_h^{-1})^{-1}$ is the effective mass of the exciton, $|u_c\rangle$ and $|u_v\rangle$ are the electron and hole Bloch functions, V is the quantization volume, and a_B^3 is the Bohr radius of the exciton. $V/\pi a_B^3$ reflects the enhancement of the interaction due to enhanced electron-hole overlap in an exciton compared to a pair of unbound electron and hole.

2. Quantum-well exciton

A semiconductor QW is a thin layer of semiconductor with a thickness comparable to the exciton Bohr radius, sandwiched between two barrier layers with a much larger band gap. The center-of-mass motion of an exciton in a QW is quantized along the confinement direction. If only one quantized level is concerned, in most cases the lowest-energy level, QW excitons behave as two-dimensional quasiparticles.

The quantum confinement also modifies the valence-band structure and hence the optical transition strength and selection rules. Most significantly, momentum conservation in an optical transition needs to be satisfied only in the QW plane but not along the confinement direction. Thus excitons in a QW couple to light with the same in-plane wave number $k_{\parallel}$ and arbitrary transverse wave number $k_{\perp}$. QWs are much more optically accessible than bulk materials.

Moreover, due to the confinement, a QW exciton has a smaller Bohr radius and larger binding energy compared to a bulk exciton, leading to an enhancement of the oscillator strength by $(a_B^{3\mathrm{D}}/a_B^{2\mathrm{D}})^3$. This enhancement is often offset by a reduction in the overlap between the light field and the exciton because the transverse coherence length of the photon field is usually much longer than the QW thickness. Hence to achieve stronger exciton-photon coupling, it is necessary to also confine the photon field in the z direction by introducing a microcavity.

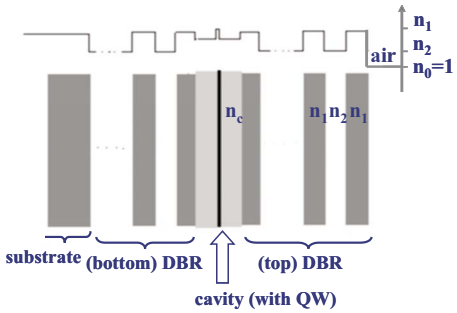

FIG. 1. (Color online) Sketch of a semiconductor $\lambda/2$ microcavity.

B. Semiconductor microcavity

Figure 1 shows a typical structure of a semiconductor microcavity consisting of a $\lambda_c/2$ cavity layer sandwiched between two distributed Bragg reflectors (DBRs). A DBR is made of layers of alternating high and low refraction indices, each layer with an optical thickness of $\lambda/4$. Light reflected from each interface destructively interfere, creating a stop band for transmission. Hence the DBR acts as a high-reflectance mirror when the wavelength of the incident light is within the stop band. When two such high-reflectance DBRs are attached to a layer with an optical thickness integer times of $\lambda_c/2$, a cavity resonance is formed at λ_c, leading to a sharp increase of the transmission T at λ_c,

$$T=\frac{(1-R_1)(1-R_2)}{[1-\sqrt{R_1R_2}]^2+4\sqrt{R_1R_2}\sin^2(\phi/2)}. \tag{4}$$

Here ϕ is the cavity round-trip phase shift of a photon at λ_c and R_1 and R_2 are the reflectances of the two DBRs. The corresponding cavity quality factor Q is

$$Q\doteq\frac{\lambda_c}{\Delta\lambda_c}\simeq\frac{\pi(R_1R_2)^{1/4}}{1-(R_1R_2)^{1/2}}, \tag{5}$$

where $\Delta\lambda_c$ is the width of the resonance. An ideal cavity has $Q=\infty$. If the cavity length is $\lambda/2$, Q is the average number of round trips a photon travels inside the cavity before it escapes. Figure 2(a) gives an example of the reflection spectrum of a cavity with $Q\simeq 4000$ at normal incidence. Figure 2(b) shows the field intensity distribution $|E(z)|^2$ of the resonant mode. The field is concentrated around the center of the cavity; its amplitude is enhanced by ~20 times compared to the free space value. Unlike in a metallic cavity, the field penetration depth into the DBRs is much larger. The effective cavity length is extended in a semiconductor microcavity as

$$L_{\mathrm{eff}}=L_c+L_{\mathrm{DBR}},$$

$$L_{\mathrm{DBR}}\approx\frac{\lambda_c}{2n_c}\frac{n_1n_2}{|n_1-n_2|}. \tag{6}$$

Here n_1 and n_2 are the refraction indices of the DBR layers, as shown in Fig. 1

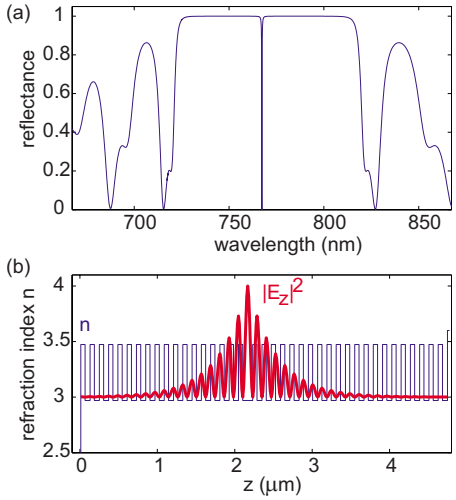

FIG. 2. (Color online) Properties of a high quality microcavity. (a) Reflectance of an empty $\lambda/2$ microcavity. (b) The cavity structure and field intensity distribution $|E_z|^2$ of the resonant TE mode.

The planar DBR cavity confines the photon field in the z direction but not in the x-y plane. The incident light from a slant angle θ relative to the z axis has a resonance at $\lambda_c/\cos\theta$. As a result, the cavity has an energy dispersion versus the in-plane wave number $k_\parallel$,

$$E_{\rm cav} = \frac{\hbar c}{n_c}\sqrt{k_\perp^2 + k_\parallel^2}, \tag{7}$$

where $k_\perp = n_c(2\pi/\lambda_c)$. And there is a one-to-one correspondence between the incidence angle θ and each resonance mode with in-plane wave number $k_\parallel$,

$$k_\parallel = n_c\frac{2\pi}{\lambda_c}\tan\left[\sin^{-1}\left(\frac{\sin\theta}{n_c}\right)\right] \approx \frac{2\pi}{\lambda_c}\theta \quad \text{when } k_\parallel \ll k_\perp. \tag{8}$$

In the region $k_\parallel \ll k_\perp$, we have

$$E_{\rm cav} \approx \frac{\hbar c}{n_c}k_\perp\left(1 + \frac{k_\parallel^2}{2k_\perp^2}\right) = E_{\rm cav}(k_\parallel = 0) + \frac{\hbar^2 k_\parallel^2}{2m_{\rm cav}}. \tag{9}$$

Here the cavity-photon effective mass is

$$m_{\rm cav} = \frac{E_{\rm cav}(k_\parallel = 0)}{c^2/n_c^2}. \tag{10}$$

It is typically on the order of $10^{-5}m_e$.

C. Quantum-well microcavity polariton

1. The Hamiltonian

When the GaAs QWs are placed at the antinodes of the resonant field of a semiconductor microcavity, the $J=1$ heavy-hole exciton doublet strongly interacts with the confined optical field of the cavity. If the rate of energy exchange between the cavity field and excitons becomes much faster than the decay and decoherence rates of both the cavity photons and the excitons, an excitation in the system is stored in the combined system of photons and excitons. Thus the elementary excitations of the system are no longer excitons or photons but a new type of quasiparticles called the polaritons.

Using the rotating wave approximation, the linear Hamiltonian of the system is written in the second quantization form as

$$\begin{aligned}\hat{H}_{\rm pol} &= \hat{H}_{\rm cav} + \hat{H}_{\rm exc} + \hat{H}_I \\ &= \sum E_{\rm cav}(k_\parallel, k_c)\hat{a}_{\boldsymbol{k}_\parallel}^\dagger \hat{a}_{\boldsymbol{k}_\parallel} + \sum E_{\rm exc}(k_\parallel)\hat{b}_{\boldsymbol{k}_\parallel}^\dagger \hat{b}_{\boldsymbol{k}y} \\ &\quad + \sum g_0(\hat{a}_{\boldsymbol{k}_\parallel}^\dagger \hat{b}_{\boldsymbol{k}_\parallel} + \hat{a}_{\boldsymbol{k}_\parallel}\hat{b}_{\boldsymbol{k}_\parallel}^\dagger).\end{aligned} \tag{11}$$

Here $\hat{a}_{\boldsymbol{k}_\parallel}^\dagger$ is the photon creation operator with an in-plane wave number $k_\parallel$ and longitudinal wave number $k_c = \boldsymbol{k}\cdot\hat{\boldsymbol{z}}$ determined by the cavity resonance. $\hat{b}_{\boldsymbol{k}_\parallel}^\dagger$ is the exciton creation operators with an in-plane wave number $\boldsymbol{k}_\parallel$. g_0 is the exciton-photon dipole interaction strength; it is nonzero only between modes with the same $\boldsymbol{k}_\parallel$. The above Hamiltonian can be diagonalized by the transformations

$$\hat{P}_{\boldsymbol{k}_\parallel} = X_{\boldsymbol{k}_\parallel}\hat{b}_{\boldsymbol{k}_\parallel} + C_{\boldsymbol{k}_\parallel}\hat{a}_{\boldsymbol{k}_\parallel}, \tag{12}$$

$$\hat{Q}_{\boldsymbol{k}_\parallel} = -C_{\boldsymbol{k}_\parallel}\hat{b}_{\boldsymbol{k}_\parallel} + X_{\boldsymbol{k}_\parallel}\hat{a}_{\boldsymbol{k}_\parallel}. \tag{13}$$

Then $\hat{H}_{\rm pol}$ becomes

$$\hat{H}_{\rm pol} = \sum E_{\rm LP}(k_\parallel)\hat{P}_{\boldsymbol{k}_\parallel}^\dagger \hat{P}_{\boldsymbol{k}_\parallel} + \sum E_{\rm UP}(k_\parallel)\hat{Q}_{\boldsymbol{k}_\parallel}^\dagger \hat{Q}_{\boldsymbol{k}_\parallel}. \tag{14}$$

Here $(\hat{P}_{\boldsymbol{k}_\parallel}, \hat{P}_{\boldsymbol{k}_\parallel}^\dagger)$ and $(\hat{Q}_{\boldsymbol{k}_\parallel}, \hat{Q}_{\boldsymbol{k}_\parallel}^\dagger)$ are the creation and annihilation operators of the new quasiparticles or eigenmodes of the system. They are called the lower polariton (LP) and upper polariton (UP), corresponding to the two branches of lower and higher eigenenergies, respectively. Thus a polariton is a linear superposition of an exciton and a photon with the same in-plane wave number $\boldsymbol{k}_\parallel$. Since both excitons and photons are bosons, so are the polaritons. The exciton and photon fractions in each LP and UP are given by the amplitude squared of $X_{k_\parallel}$ and $C_{k_\parallel}$ which are referred to as the Hopfield coefficients (Hopfield, 1958). They satisfy

$$|X_{k_\parallel}|^2 + |C_{k_\parallel}|^2 = 1. \tag{15}$$

Let $\Delta E(k_\parallel) = E_{\rm exc}(k_\parallel) - E_{\rm cav}(k_\parallel, k_c)$; $X_{k_\parallel}$ and $C_{k_\parallel}$ are given by

$$\begin{aligned}|X_{k_\parallel}|^2 &= \frac{1}{2}\left(1 + \frac{\Delta E(k_\parallel)}{\sqrt{\Delta E(k_\parallel)^2 + 4g_0^2}}\right), \\ |C_{k_\parallel}|^2 &= \frac{1}{2}\left(1 - \frac{\Delta E(k_\parallel)}{\sqrt{\Delta E(k_\parallel)^2 + 4g_0^2}}\right).\end{aligned} \tag{16}$$

At $\Delta E = 0$, $|X|^2 = |C|^2 = \frac{1}{2}$, LP and UP are exactly half photon half exciton.

The energies of the polaritons, which are the eigenenergies of the Hamiltonian (14), are deduced from the diagonalization procedure as

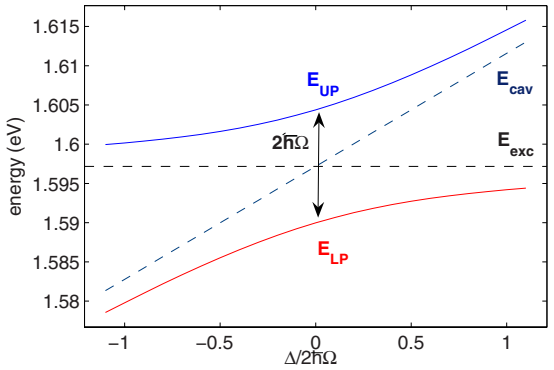

FIG. 3. (Color online) Anticrossing of LP and UP energy levels when tuning the cavity energy across the exciton energy, calculated by the transfer-matrix method.

$$E_{\mathrm{LP,UP}}(k_\parallel) = \tfrac{1}{2}[E_{\mathrm{exc}} + E_{\mathrm{cav}} \pm \sqrt{4g_0^2 + (E_{\mathrm{exc}} - E_{\mathrm{cav}})^2}]. \tag{17}$$

When the uncoupled exciton and photon are at resonance, $E_{\mathrm{exc}}=E_{\mathrm{cav}}$, LP and UP energies have the minimum separation $E_{\mathrm{UP}}-E_{\mathrm{LP}}=2g_0$, which is often called the normal-mode splitting in analogy to the Rabi splitting of a single-atom cavity system. Due to the coupling between the exciton and photon modes, the new polariton energies anticross when the cavity energy is tuned across the exciton energy. This is one of the signatures of "strong coupling" (Fig. 3). When $|E_{\mathrm{cav}}-E_{\mathrm{exc}}| \gg g_0$, polaritons quickly become indistinguishable from a photon or exciton. Unless otherwise specified, the detuning is assumed to be comparable to or less than the coupling strength in our discussions.

2. Polariton dispersion and effective mass

We define Δ_0 as the exciton and photon energy detuning at $k_\parallel=0$,

$$\Delta_0 \doteq E_{\mathrm{cav}}(k_\parallel = 0) - E_{\mathrm{exc}}(k_\parallel = 0). \tag{18}$$

Given Δ_0, Eq. (17) gives the polariton energy-momentum dispersions. In the region $\hbar^2 k_\parallel^2/2m_{\mathrm{cav}} \ll 2g_0$, the dispersions are parabolic,

$$E_{\mathrm{LP,UP}}(k_\parallel) \simeq E_{\mathrm{LP,UP}}(0) + \frac{\hbar^2 k_\parallel^2}{2m_{\mathrm{LP,UP}}}. \tag{19}$$

The polariton effective mass is the weighted harmonic mean of the mass of its exciton and photon components,

$$\frac{1}{m_{\mathrm{LP}}} = \frac{|X|^2}{m_{\mathrm{exc}}} + \frac{|C|^2}{m_{\mathrm{cav}}}, \tag{20}$$

$$\frac{1}{m_{\mathrm{UP}}} = \frac{|C|^2}{m_{\mathrm{exc}}} + \frac{|X|^2}{m_{\mathrm{cav}}}, \tag{21}$$

where X and C are the Hopfield coefficients given by Eq. (16). m_{exc} is the effective exciton mass of its center-of-mass motion and m_{cav} is the effective cavity-photon mass given by Eq. (10). Since $m_{\mathrm{cav}} \ll m_{\mathrm{exc}}$,

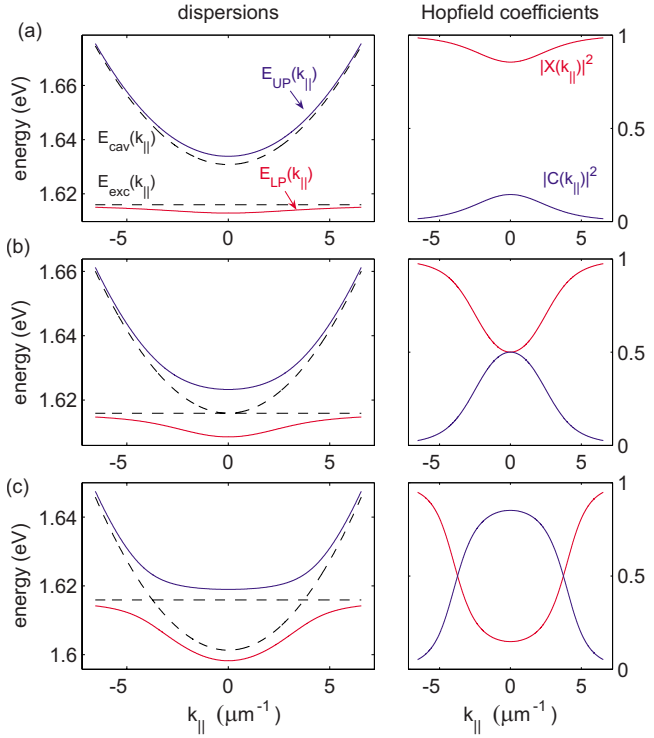

FIG. 4. (Color online) Polariton dispersions and corresponding Hopfield coefficients at (a) $\Delta=2g_0$, (b) $\Delta=0$, and (c) $\Delta=-2g_0$.

$$m_{\mathrm{LP}}(k_\parallel \sim 0) \simeq m_{\mathrm{cav}}/|C|^2 \sim 10^{-4} m_{\mathrm{exc}},$$
$$m_{\mathrm{UP}}(k_\parallel \sim 0) \simeq m_{\mathrm{cav}}/|X|^2. \tag{22}$$

The very small effective mass of LPs at $k_\parallel \sim 0$ makes possible the very high critical temperature of phase transitions for the system. At large $k_\parallel$ where $E_{\mathrm{cav}}(k_\parallel) - E_{\mathrm{exc}}(k_\parallel) \gg g_0$, dispersions of the LP and UP converge to the exciton and photon dispersions, respectively, and LP has an effective mass $m_{\mathrm{LP}} \sim m_{\mathrm{exc}}$. Hence the LP's effective mass changes by four orders of magnitude from $k_\parallel \sim 0$ to large $k_\parallel$. This peculiar shape has important implications in the energy relaxation dynamics of polaritons, as discussed in Sec. IV. A few examples of the polariton dispersion with different Δ_0 are given in Fig. 4.

3. Polariton decay

When taking into account the finite lifetime of the cavity photon and QW exciton, the eigenenergy (17) is modified as

$$E_{\mathrm{LP,UP}}(k_\parallel) = \tfrac{1}{2}\{E_{\mathrm{exc}} + E_{\mathrm{cav}} + i(\gamma_{\mathrm{cav}} + \gamma_{\mathrm{exc}}) \pm \sqrt{4g_0^2 + [E_{\mathrm{exc}} - E_{\mathrm{cav}} + i(\gamma_{\mathrm{cav}} - \gamma_{\mathrm{exc}})]^2}\}. \tag{23}$$

Here γ_{cav} is the out-coupling rate of a cavity photon due to imperfect mirrors and γ_{exc} is the nonradiative decay rate of an exciton. Thus the coupling strength must be larger than half of the difference in decay rates to exhibit anticrossing, i.e., to have polaritons as the new eigenmodes. In other words, an excitation must be able

TABLE I. Parameter comparison of BEC systems.

Systems	Atomic gases	Excitons	Polaritons
Effective mass m^*/m_e	10^3	10^{-1}	10^{-5}
Bohr radius a_B	10^{-1} Å	10^2 Å	10^2 Å
Particle spacing: $n^{-1/d}$	10^3 Å	10^2 Å	1 μm
Critical temperature T_c	1 nK–1 μK	1 mK–1 K	1–>300 K
Thermalization time/Lifetime	1 ms/1 s$\sim 10^{-3}$	10 ps/1 ns$\sim 10^{-2}$	(1–10 ps)/(1–10 ps)=0.1–10

to coherently transfer between a photon and an exciton at least once. When $g_0 \gg (\gamma_{cav}-\gamma_{exc})/2$, we call the system in the strong-coupling regime. In the opposite limit when excitons and photons instead are the eigenmodes, the system is called to be in the weak-coupling regime, and the radiative decay rate of an exciton is given by the optical transition matrix element. We are mostly interested in microcavities with $\gamma_{exc} \ll \gamma_{cav} \ll g_0$; then Eq. (17) gives a good approximation of the polariton energies.

As a linear superposition of an exciton and a photon, the lifetime of the polaritons is directly determined by γ_{exc} and γ_{cav} as

$$\gamma_{LP} = |X|^2\gamma_{exc} + |C|^2\gamma_{cav}, \tag{24}$$

$$\gamma_{UP} = |C|^2\gamma_{exc} + |X|^2\gamma_{cav}. \tag{25}$$

In typical high quality semiconductor samples available today, $\gamma_{cav}=1-10$ ps and $\gamma_{exc}\sim 1$ ns, hence the polariton lifetime is mainly determined by the cavity-photon lifetime: $\gamma_{LP}\simeq|C|^2\gamma_{cav}$. Polariton decays in the form of emitting a photon with the same $k_\parallel$ and total energy $\hbar\omega = E_{LP,UP}$. The one-to-one correspondence between the internal polariton mode and the external out-coupled photon mode lends convenience to experimental access to the system (see Sec. II.E.4).

4. Very strong-coupling regime

The definition of polariton operators in Eqs. (11)–(14) follows the procedure to first diagonalize the electron-hole Hamiltonian by exciton operators and then diagonalize the exciton-photon Hamiltonian by polariton operators, treating the excitons as structureless quasiparticles. When the exciton-photon coupling is so strong as to become comparable to exciton binding energy, the question arises whether or not the above procedure is still valid. A more rigorous approach is to treat the electron, hole, and photon on equal footing, and one finds that the LPs then consist of excitons with an even smaller effective Bohr radius and larger binding energy, while the opposite holds for UPs. This is called the very strong-coupling effect (Khurgin, 2001; Citrin and Khurgin, 2003). It is a consequence of sub-band mixing of higher-orbital excitons (mixing with $1s,2s,2p,\ldots$ exciton levels).

D. Polaritons for quantum phase research

As composite bosons with not only fermionic but also photonic constituents, polaritons constitute a unique system for exploring both cavity QED and many-body physics.

A variety of quantum phases is predicted for polaritons, including BEC, superfluidity, Berezinskii-Kosterlitz-Thouless (BKT) (Malpuech *et al.*, 2003), and Bardeen-Cooper-Schrieffer (BCS) states (Keldysh and Kozlov, 1968; Comte and Nozières, 1982; Malpuech *et al.*, 2003; Littlewood *et al.*, 2004; Sarchi and Savona, 2006, 2007a). Table I compares the basic parameters of polaritons to semiconductor excitons and cold atoms, which consist of the major table-top Bose systems for quantum phase studies.

The parameter scales of these systems differ by many orders of magnitude. Even for the same type of quantum phase, the polariton system has distinct characteristics and requires dedicated theoretical frameworks. In particular, we discuss two important fundamental issues pertaining to the ground state of a degenerate polariton gas: the possibility of BEC and BKT phases of polaritons as two-dimensional systems and the BEC-BCS crossover or Mott transition in the high-density regime of polaritons as a system of composite bosons. Due to the short lifetime of polaritons compared to their thermalization time, the excitation spectra of a polariton condensate differ from their atomic gas counterparts, as discussed in Sec. VIII.

On the experimental side, the polariton is a most accessible system, especially due to the high critical temperature associated with its light effective mass and the one-to-one correspondence between each polariton and each leakage cavity photon. These and some other aspects of the experimental advantages of polaritons are summarized later in this section.

1. Critical densities of 2D quasi-BEC and BKT phase transitions

A uniform 2D system of bosons does not have a BEC phase transition at finite temperatures in the thermodynamic limit since long-wavelength thermal fluctuations destroy long-range order (Mermin and Wagner, 1966; Hohenberg, 1967).

If the Bose gas is confined by a spatially varying potential $U\sim r^\eta$ (Bagnato and Kleppner, 1991; Griffin *et al.*,

1995), the constant density of states (DOS) of the uniform 2D system is dramatically modified by the potential, and a BEC phase at finite temperature is recovered. A few experimental implementations of transverse confinement potential in polariton systems will be discussed in Sec. IX.

Practically, any experimental system has a finite size and a finite number of single-particle states. With discrete energy levels ε_i $(i=1,2,\ldots)$ and size $S=L^2$, the critical condition for quasi-BEC in a finite 2D system can be defined as

$$\mu = \varepsilon_1 \quad \text{(chemical potential)}, \tag{26}$$

$$n_c = \frac{1}{S}\sum_{i\geqslant 2} \frac{1}{e^{\varepsilon_i/k_BT}-1} \quad \text{(critical 2D density)}. \tag{27}$$

In a 2D box system of size L, the critical condition can be fulfilled at $T_c>0$ at a critical density,

$$n_c = \frac{2}{\lambda_T^2}\ln\left(\frac{L}{\lambda_T}\right). \tag{28}$$

If the particle number N is sufficiently large and/or the temperature is sufficiently low, the phase transition shows similar features as a BEC phase transition defined at the thermodynamic limit (Ketterle and van Druten, 1996).

In addition to the quasi-BEC phase, formation of vortices drives another phase transition unique to the 2D system—the BKT transition (Berezinskii, 1971, 1972; Kosterlitz and Thouless, 1972, 1973). At low temperatures, thermally excited vortices may form in the system which may support a local order. With further cooling of the system to below a critical temperature T_{BKT}, the bound pair of oppositely circulating vortices form, which stabilize the phase to a power-law decay versus distance and support finite superfluid density. The critical temperature of the BKT transition is

$$k_B T_{\mathrm{BKT}} = n_s \frac{\pi\hbar^2}{2m^2}, \tag{29}$$

where n_s is the superfluid density. Equation (29) can also be written in terms of the thermal de Broglie wavelength λ_T (Khalatnikov, 1965),

$$\lambda_T(T) \doteq \sqrt{\frac{2\pi\hbar^2}{mk_BT}}, \tag{30}$$

$$n_s\lambda_T(T_c)^2 = 4. \tag{31}$$

In most experiments discussed in this review, the system size is small enough such that a finite-size BEC phase transition is expected before a BKT transition (Kavokin *et al.*, 2003). However, the nature of the ground state and its excitation spectra, as well as the dependence of the BEC and BKT critical densities on the system parameters, are not yet well understood at present. Observations of phonon modes, superfluidity, and single and bound pair of vortices is discussed in Sec. VIII. Understanding of these observations may provide a venue to our further understanding of 2D quantum phases. For a recent review of the ground-state properties of a 2D Bose gas in general, see Posazhennikova (2006).

2. Quantum phases at high excitation densities

An important parameter not listed in Table I is the particle-particle interaction strength or the scattering length a. For atomic gasses, a is usually much less than the particle spacing, satisfying the diluteness condition. In diatomic gases where each diatomic molecule consists of two fermionic atoms, a can be defined for the interaction between two Fermi atoms and has a hyperbolic dependence on an external magnetic field. The magnetic field tunes a from a small negative value ($a<0$, $k_f|a| \ll 1$, k_f is the wave vector at the Fermi surface) to a very large negative or positive value at the unitary condition ($k_f|a| \gg 1$) near the Feshbach resonance and then to a small positive value (Feshbach, 1962). Correspondingly, below a critical temperature, the system exhibits a crossover from a degenerate Fermi gas described by the standard BCS theory to a degenerate Bose gas with a BEC phase.

A similar BEC to BCS crossover is also possible in exciton and polariton systems (Comte and Nozières, 1982; Eastham and Littlewood, 2001). Here the pairing is between an electron and a hole, and the crossover is controlled by the density of the electrons and holes n_{exc}. The density n_{exc} tunes both the interparticle spacing $n_{\mathrm{exc}}^{-1/d}$ and, through Coulomb screening, the exciton-exciton interaction strength and exciton-photon coupling. The polariton gas behaves as a weakly interacting Bose gas when the density is low ($n_{\mathrm{exc}} \ll n_{\mathrm{Mott}}$), with the scattering length approximated by the exciton Bohr radius a_B. Increasing n_{exc} to n_{Mott}, the BEC-BCS crossover may take place, where degenerate Fermi gasses of electrons and holes are paired in the momentum space with a Bohr radius comparable to the particle spacing. At very high densities, we have an electron and hole plasma with screened Coulomb interactions, which coherently couple to a cavity-photon field. Inhomogeneity in exciton energy and inelastic scattering at crystal defects, however, may suppress the BCS gap and reduce the system to an incoherent electron and hole plasma. Detailed studies of the phase diagrams at high excitation densities and effects of dephasing can be found in Eastham and Littlewood (2001), Szymanska *et al.* (2003), and Littlewood *et al.* (2004).

In the current review, we focus on the BEC regime of LPs, where the excitation density is below the exciton saturation density and excitons and LPs can be well described as interacting bosons.

3. Experimental advantages of polaritons for BEC study

Beside as a unique system of fundamental interest, polaritons also possess many experimental advantages for BEC research. Most notable is the light effective mass of polaritons in the region $k_\parallel \ll k_c$ (see Sec. II.C.2.).

Taking into account the excitonlike dispersion at higher $k_{\parallel}$, the critical temperatures of polariton condensation range from cryogenic temperature of a few kelvin up to room temperature and higher.[3] Not only does this simplify enormously the experimental setups for polariton research but it also makes polaritons a natural and practical candidate for quantum device applications.

A common enemy against quantum phase transitions in solids is the unavoidable compositional and structural disorders. By dressing the excitons with a microcavity vacuum field, extended coherence is maintained in the combined excitation in a microcavity polariton system, and the detrimental effects of disorders are largely suppressed.

Saturation and phase-space filling are another two obstacles against BEC of composite bosons in solids. In a microcavity polariton system, multiple QWs can be used to dilate the exciton density per QW for a given total polariton density: $n_{\mathrm{exc}}^{\mathrm{QW}}=n_{\mathrm{LP}}/N_{\mathrm{QW}}$, where N_{QW} is the number of QWs.

A main challenge for realizing a thermodynamic phase transition and spontaneous coherence has been efficient cooling of hot particles. It is especially so for relatively short-lived quasiparticles in solids. The small effective mass, hence small energy DOS of polaritons, comes to rescue here. Due to the small DOS, a quantum degenerate seed of low-energy polaritons is relatively easy to achieve. Hence the bosonic final-state stimulation effect is pronounced, which accelerates energy relaxation of the polaritons.

Finally, the cavity-photon component of a polariton couples out of the cavity at a fixed rate while conserving energy and in-plane momentum. Many essential properties of the polariton gas can be directly measured through the leakage photon field with well-developed spectroscopic and quantum optical techniques, including coherence functions (Deng *et al.*, 2002, 2007; Kasprzak *et al.*, 2006, 2008), population distributions in both coordinate (Deng *et al.*, 2003, 2007; Kasprzak *et al.*, 2006) and configuration space (Deng *et al.*, 2003; Kasprzak *et al.*, 2006), vortices (Lagoudakis *et al.*, 2008; Roumpos, Hoefling, *et al.*, 2009), and transport properties (Utsunomiya *et al.*, 2008; Amo *et al.*, 2009). In comparison, complicated and often indirect techniques are required to probe those properties in matter systems. Hence the polariton system also offers a unique opportunity for studying new and open questions in quantum phase research.

E. Experimental methodology

1. Typical material systems

An optimal microcavity system for polariton BEC has the following: (1) high quality cavity, hence long cavity photon and polariton lifetime; (2) large polariton-phonon and polariton-polariton scattering cross sections, hence efficient polariton thermalization; (3) small exciton Bohr radius and large exciton binding energy, hence high exciton saturation density; and (4) strong exciton-photon coupling, hence robust strong coupling; it requires both large QW exciton oscillator strength and large overlap of the photon field and the QWs.

The choice of a direct band-gap semiconductor depends first on the fabrication technology. The best fabrication quality of both quantum well and microcavity has been achieved via molecular-beam epitaxy growth of $Al_xGa_{1-x}As$-based samples ($0\leqslant x\leqslant 1$), thanks to the close match of the lattice constants a_{lat} of AlAs and GaAs and a relatively large difference between their band-gap energies E_g. At 4 K, GaAs has $a_{\mathrm{lat}}=5.64$ Å and $E_g=1.519$ eV and AlAs has $a_{\mathrm{lat}}=5.65$ Å and $E_g=3.099$ eV. Nearly strain and defect-free GaAs QWs are now conventionally grown between $Al_xGa_{1-x}As$. Inhomogeneous broadening of exciton energy is limited mainly by monolayer QW thickness fluctuation. Nearly defect-free microcavity structures can be grown with more than 30 pairs of AlAs/GaAs layers in the DBRs and with a cavity quality factor Q exceeding 10^5 (Reitzenstein *et al.*, 2007). Many signatures of polariton condensation were first obtained in GaAs-based systems (Deng *et al.*, 2002, 2003, 2007; Balili *et al.*, 2007; Lai *et al.*, 2007).

Another popular choice is the CdTe-based II-IV system, with CdTe QWs and $Mg_xCd_{1-x}Te$ and $Mn_xCd_{1-x}Te$ barrier and DBR layers. The larger lattice mismatch is compensated by larger binding energy and larger oscillator strength, as well as larger refractive index contrast (hence less layers needed in the DBRs). The smaller Bohr radius of CdTe excitons, on the one hand, allows a larger saturation density and, on the other hand, reduces the polariton and acoustic phonon scattering. Hence the energy relaxation bottleneck is more persistent in this system, which prevented condensation in the LP ground state in early experiments (Huang *et al.*, 2002; Richard *et al.*, 2005). By adjusting the detuning to facilitate thermalization, partially localized polariton condensation into the ground state was finally observed by Kasprzak *et al.* (2006).

In recent years, there has been intense interest in developing certain wide-band-gap material systems with small lattice constants. In these materials, the exciton binding energy and oscillator strength are large enough, so that a polariton laser may survive at >300 K, operating at visible to ultraviolet wavelengths. However, fabrication techniques for these materials are not as mature as for GaAs- or CdTe-based systems. The structures of wide-band-gap materials suffer a higher concentration of impurities and crystal defects. Integration of the QWs with microcavities is challenging due to the lack of lattice matched DBR layers. Though the strong-coupling regime is still hard to reach or reproduce at present, there have been a few promising reports on the observation of polaritons in ZnSe (Pawlis *et al.*, 2002), GaN (Tawara *et al.*, 2004; Butte *et al.*, 2006), and ZnO (Shimada *et al.*, 2008; Chen *et al.*, 2009). Lasing of GaN po-

[3]Note that other constrains on the condensation temperature T_c apply. For example, k_BT_c must be smaller than the exciton binding energy or half of the LP-UP splitting.

laritons at room temperature was reported (Christopoulos *et al.*, 2007; Christmann *et al.*, 2008). Also active research is conducted on Frenkel exciton polaritons in organic materials (Lidzey *et al.*, 1998, 1999; Schouwink *et al.*, 2001; Takada *et al.*, 2003; Kena-Cohen *et al.*, 2008).

2. Structure design considerations

To achieve maximum exciton-photon coupling, a short cavity is generally preferred with (multiple) narrow QWs placed at the antinode(s) of the cavity field. A $\lambda/2$ cavity gives the largest field amplitude at the cavity center for given reflectance of the DBRs. An optimal QW thickness, often between 0.5 and 1 Bohr radius of a bulk exciton, leads to smaller Bohr radius and enhanced oscillator strength. To increase the field-exciton overlap, one can use multiple closely spaced narrow QWs and even put QWs in the two antinodes next to the central one, leading to an increased total coupling strength $g_0 \propto \sqrt{N_{\mathrm{QW}}}$. The difference in the field amplitude E at each QW has an effect similar to inhomogeneous broadening of the QW exciton linewidth (Pau, Björk, *et al.*, 1996). Using multiple QWs has another important benefit—an increased saturation density of LPs, which scales with N/a_B^2. When g_0 is increased to become comparable with the exciton binding energy, the strong-coupling effect further reduces exciton Bohr radius in the LP branch and increases the exciton saturation density.

3. *In situ* tuning parameters

The microcavity system of a given composition and structure has a few useful parameters that can be adjusted *in situ* during the experiments: detuning Δ of the uncoupled cavity resonance relative to the QW exciton resonance, density of the polaritons, and temperature of the host lattice.

Tapering of the cavity thickness by special sample growth techniques enables tuning of Δ across the sample. Changing Δ changes the exciton and photon fractions in the LPs, hence the dispersions and lifetimes of the LPs. It has important implications in LP dynamics which is discussed in Sec. V.

The density of the polaritons is directly controlled by the excitation density. A polariton density well into the BCS limit is within reach with commercial lasers. The density dependence of various properties of the system allows systematic studies of the its phase-transition physics.

The temperature of the acoustic phonon reservoir is readily tuned by thermoelectric heaters from cryogenic temperature up to room temperature or higher. The lattice temperature influences the dynamics of the polaritons. However, the short-lived LPs are often not at the same temperature as the lattice or do not have a well-defined temperature.

4. Measurement techniques

From the measurement viewpoints, the microcavity polariton is a most accessible BEC system. There exists a one-to-one correspondence between an internal polariton in mode $k_\parallel$ and an external photon with the same energy and in-plane wave number (Houdré *et al.*, 1994). The internal polariton is coupled to the external photon via its photonic component with a fixed coupling rate [see Eq. (25)]. Hence information on the internal polaritons can be directly measured via the external photon fields. At the same time, due to the steep dispersion of polaritons, polariton modes with different $k_\parallel$ and $E_{\mathrm{LP}}(k_\parallel)$ are well resolved with conventional optics. It is mainly through the external photon field that we learn about the polaritons.

The basic properties of a polariton system can be characterized through reflection or transmission measurements using a weak light source. For instance, from a measured reflection spectrum, one extracts the resonances of the microcavity system, the widths of the resonances, as well as the cavity stop-band structure. Since most microcavities have a tapered cavity length, a serial of reflection measurement at various positions on the sample reveals the characteristic anticrossing (crossing) of the eigenenergies and thus verifies strong (weak) coupling between the cavity and exciton modes. Dispersion of the resonances may also be measured by angle-resolved reflection, although photoluminescence (PL) is often more convenient for this purpose.

Polaritons are conveniently excited, resonantly or nonresonantly, by optical pumping. By changing the collection angle of the PL, $k_\parallel$-dependent spectra are obtained, which map out the energy-momentum dispersion as well as momentum distribution of the polaritons. Complementary to momentum-resolved PL, near-field imaging of the sample surface maps out the spatial distribution of LPs. Quantum optics measurement on the PL reveals the quantum statistics of LPs. Time-resolved PL or imaging measurements map out the dynamics and transport of LPs.

F. Theoretical methods

We describe the main theoretical tools considered for studying polariton condensation. Some references for relevant methods and concepts are given, but are by no means comprehensive.

1. Semiclassical Boltzmann kinetics

Since polaritons are quasiparticles with a lifetime of 1–100 ps, polariton condensation in general involves injection, relaxation, and decay of the polaritons and thus is a transient phenomena described by the kinetics of the condensation. The semiclassical Boltzmann rate equations have been well adapted to describe the polariton kinetics (Tassone *et al.*, 1997; Ciuti *et al.*, 1998; Tassone and Yamamoto, 1999; Malpuech *et al.*, 2002; Porras *et al.*, 2002; Kavokin *et al.*, 2004; Doan *et al.*, 2005). Numerical simulations based on the Boltzmann equations have interwound with experimental works to understand the interactions in the polariton system, the mechanisms of

polariton relaxation, and the statistical properties of the system, which are reviewed in Secs. II.F.2–II.F.4.

Limitations of this semiclassical approach exist, however, when the system is above the condensation threshold. The random-phase approximation of the Boltzmann equations is no longer valid when coherence emerges within the ground state as well as between the ground state and its low-energy excitations. Moreover, the condensate and the excited states see different mean-field energy shifts; the spectrum of low-energy excitations changes from a free-particle spectrum with finite effective mass to a linear Bogoliubov spectrum. These properties are not explained with the Boltzmann equations. The appropriate tool is quantum kinetics.

To account for the difference of a condensed state compared to a normal state and to help understand the coherence properties of the condensate, various models have been developed that go beyond the conventional Boltzmann equations. Two common approximations in these models are to take advantage of the peculiar energy-momentum dispersion of the LPs and to divide the system into two regions in the momentum space. For states with relative large momentum and negligible quantum coherence, the semiclassical kinetics is used. For the ground state and a small set of states with smaller momenta and significant photonic fractions, the correlation between the ground state and excitations is examined in greater detail. For example, Laussy *et al.* (2004) and Doan, Cao, *et al.* (2008) introduced a stochastic extension of Langevin fluctuations to the Boltzmann equations. The method enables estimation of the first- and second-order coherence functions of the condensate, which are reviewed in Sec. VII. Sarchi and Savona (2007a) extended the Boltzmann equations under the Bogoliubov approximation to include virtual excitations between the condensate and excited states and calculated the first-order coherence function of the system.

2. Quantum kinetics

A complete and self-consistent description of the condensation physics requires quantum kinetics. Quantum kinetics can be developed either on the basis of nonequilibrium Keldysh Green's functions (Haug and Jauho, 2008) or on the basis of a truncated hierarchy of equations for reduced density matrices (Kuhn, 1997). The quantum kinetics description of condensation includes the equation of motion for the order parameter, i.e., the expectation values of the ground-state polariton annihilation operator, as well as an equation for the population of the excited states. The Dyson equation formulated in the time regime will couple density matrices which are functions of only one-time argument to two-time scattering self-energies and two-time Green's functions. One can express these off-diagonal quantities in the time arguments by two-time spectral functions and one-time density matrices. The full set of kinetic equations thus includes the equations for the spectral functions, i.e., the retarded and advanced Green's functions. Through these spectral functions, the polariton spectra—which change during the condensation—are introduced self-consistently in the condensation kinetics. A full quantum kinetic simulation of polariton condensation is computationally intensive and presently not yet available.[4]

3. Equilibrium and steady-state properties

If the polariton lifetime is long compared to the relaxation time, a condensed polariton system can be considered as in quasiequilibrium, and thus the static properties may be approximated by a mean-field theory based on the Gross-Pitaevskii equation (Pethick and Smith, 2001; Pitaevskii and Stringari, 2003). We introduce the Gross-Pitaevskii equations in Sec. VIII and apply it to experiments on the spectral properties and superfluidity of polariton condensation.

When a short-lived polariton system is under continuous-wave pumping, a steady state may be reached. Properties of a steady-state polariton condensate have been calculated by linearizing a generalized Gross-Pitaevskii equation around the steady state (Wouters and Carusotto, 2007) and also by a Keldysh Green's function approach (Szymanska *et al.*, 2006). Due to constant pumping and decay of the polaritons, the low-energy excitations are expected to be diffusive, manifested as a flat dispersion near the ground state. A vortex induced during the relaxation process at local disorder potential was also observed (Lagoudakis *et al.*, 2008).

4. System size

The two-dimensional polariton systems typically have a (transverse) size of 10–100 μm across. The finite size leads to an energy gap $\delta E \simeq 3\hbar^2/(2m_{\mathrm{eff}}S)$ between the ground state and first-excited states. Given a typical GaAs polariton mass of $m_{\mathrm{eff}}=5\times10^{-5}m_e$ (here m_e is the free-electron mass), ΔE is about 0.2 meV. This gap results in a finite-size BEC, and the condensate density increases with decreasing system size. However, the real transverse extension in experiments is not known accurately as it is often given by the spot size of the pumping laser. This uncertainty in the spatial extension imposes a specific problem in numerical simulations of the polariton kinetics.

III. RATE EQUATIONS OF POLARITON KINETICS

As elementary excitations of the microcavity system, polaritons are most conveniently created by a laser pump pulse, after which they relax and under appropriate conditions accumulate at least partly in the ground

[4]Currently a simplified model of quantum kinetics is given by Wouters and Savona (2009).

state of the LP branch, before they completely decay. In order to study a spontaneous phase transition, pumping should be incoherent, so that there are no phase relations between the pump light and the condensate. One speaks about a quantum statistically degenerate state if the number of polaritons n_0 in the ground state is much larger than 1. In this case, stimulated relaxation processes dominate over the spontaneous ones by a factor $1+n_0$. The main interactions which drive the relaxation and eventually the condensation stem from the exciton-phonon interactions and the Coulomb interactions between excitons. The exchange Coulomb interactions dominate over the direct Coulomb interactions between two excitons and give rise to a repulsive interaction between two polaritons with an identical spin. This interaction provides the fastest scattering mechanism which thermalizes the polariton gas, but the temperature of the gas can only be lowered by coupling to the cold acoustic phonon reservoir.

Much of the physics of the polariton relaxation and condensation can be described with the semiclassical Boltzmann rate equations,[5] which we formulate in this section. We include the scattering due to the LP-phonon and LP-LP interactions as discussed. For most experiments to date, the cavity-photon linewidth is on the order of 1 meV. The spectral change due to condensation is not extended enough to have a substantial influence on the condensation kinetics. Hence we use only the free-particle spectrum to calculate the scattering rates. These rate equations yield results in good agreement with the experimental observations in Secs. IV.A and IV.B.

The rate equations calculate only the number of the LPs in the ground and excited states. However, we show in Sec. VII that a stochastic extension of the Boltzmann kinetics can calculate at least approximately first- and second-order coherence properties.

A. Polariton-phonon scattering

The relevant interaction between excitons and longitudinal-acoustic phonons is provided by the deformation-potential coupling with the electron and hole D_e and D_h, respectively. This interaction Hamiltonian between the LPs and phonons is (Pau, Jacobson, *et al.*, 1996; Piermarocchi *et al.*, 1996)

$$H_w^{\text{LP-ph}} = \sum_{\vec{k},\vec{q},q_z} X_k^* X_{|\vec{k}+\vec{q}|} \langle k|H_w^{x\text{-ph}}|k+q\rangle \times (c_{\vec{q},q_z} - c_{-\vec{q},-q_z}^\dagger) b_{\vec{k}+\vec{q}}^\dagger b_{\vec{k}}, \tag{32}$$

where X_k are again the exciton Hopfield coefficients of the polariton. The phonons are taken to be the bulk phonons with a wave vector $q\vec{e}_\parallel + q_z\vec{e}_z$. Only the in-plane vector component is conserved. The quantum well $1s$-exciton envelope function is given by

$$\chi(\vec{r}_\parallel, z_e, z_h) = \sqrt{\frac{2}{\pi a_B^2}} e^{-r_\parallel/a_B} f_e(z_e) f_h(z_h), \tag{33}$$

where a_B is the 2D Bohr radius and $f_{e,h}(z_{e,h})$ are the quantum well envelope functions. Evaluating the exciton-phonon interaction matrix element with this envelope function, one finds

$$G(\vec{q},q_z) = i\sqrt{\frac{\hbar(q^2+q_z^2)^{1/2}}{2\rho V u}} [D_e I_e^\parallel(q) I_e^z(q_z) - D_h I_h^\parallel(q) I_h^z(q_z)]. \tag{34}$$

Here ρ is the density, u is the sound velocity, and V is the microcavity volume. The superposition integrals for the electron (e) or hole (h) are given by

$$I_{e,h}^\parallel(q) = \left[1 + \left(\frac{m_{h,e}}{2M} q a_B\right)^2\right]^{-3/2}, \tag{35}$$

$$I_{e,h}^z(q_z) = \int_0^{L_{\text{QW}}} dz f_{e,h}^2(z) e^{iq_z z}. \tag{36}$$

These integrals cut off the sums for $q > a_B^{-1}$ and for $q_z > 2\pi/L_{\text{QW}}$.

With this interaction matrix element, the transition rates for the LPs can be written as

$$W_{\vec{k}\to\vec{k}'=\vec{k}-\vec{q}}^{\text{LP-ph}} = \frac{2\pi}{\hbar} \sum_{q_z} X_k^2 X_{k-q}^2 G(q,q_z) \times \delta(E_{k-q} - E_k \pm \hbar\omega_{q,q_z}) \times \left(N_B(\hbar\omega_{q,q_z}) + \frac{1}{2} \pm \frac{1}{2}\right), \tag{37}$$

where $N_B(\hbar\omega_q) = 1/[\exp(\hbar\omega_q) - 1]$ is the thermal phonon Bose distribution function. Here the small correction of the phonon confinement is neglected.

B. Polariton-polariton scattering

1. Nonlinear polariton interaction coefficients

The LP-LP interaction Hamiltonian generally has the form

$$\hat{H}_I = \tfrac{1}{2} U(\boldsymbol{k}_1, \boldsymbol{k}_2, \boldsymbol{q}) \hat{P}_{\boldsymbol{k}_1}^+ \hat{P}_{\boldsymbol{k}_2}^+ \hat{P}_{\boldsymbol{k}_1+\boldsymbol{q}} \hat{P}_{\boldsymbol{k}_2-\boldsymbol{q}}, \tag{38}$$

where $\hat{P}_k$ is the creation operator of a LP with the in-plane wave vector $\boldsymbol{k}$. The dependence of $U(\boldsymbol{k}_1, \boldsymbol{k}_2, \boldsymbol{q})$ on $\boldsymbol{k}_1$, $\boldsymbol{k}_2$, and $\boldsymbol{q}$ can be neglected if the momentum exchange $\boldsymbol{q}$ is small. In this case we replace $U(\boldsymbol{k}_1, \boldsymbol{k}_2, \boldsymbol{q})$ by $U_k = U(k, k, 0)$.

[5]For an introduction of other approaches, see Sec. II.F and Keeling *et al.* (2007).

For a spin-polarized polariton system, the nonlinear interaction parameter U_k can be further simplified and calculated as

$$U_k = \frac{1}{2}\delta E_X + \sqrt{g_0^2 + \frac{\Delta^2}{4}} - \sqrt{g(n)^2 + \frac{(\Delta - \delta E_X)^2}{4}},$$

$$\delta E_X = E_B \frac{n}{n_S}, \quad n_S = \frac{S}{2.2\pi a_B^{*2}|X|^2}, \tag{39}$$

$$g(n) = g_0\left(1 - \frac{n}{n_S'}\right), \quad n_S' = \frac{S}{4\pi a_B^{*2}|X|^2}.$$

Here $\Delta = E_{\mathrm{cav}}(k) - E_{\mathrm{exc}}(k)$ is the detuning between the cavity and exciton energies at given k, E_B is the exciton binding energy, a_B is the exciton Bohr radius, $2g_0$ is the normal-mode splitting at $\Delta = 0$, and S is the cross-sectional area of the system. $|X|^2 = \frac{1}{2}(1 + \Delta/\sqrt{4g_0^2 + \Delta^2})$ is the excitonic fraction of the polariton at k. δE_X represents the repulsive fermionic exchange interaction between QW excitons of the same spin (Ciuti *et al.*, 1998; Rochat *et al.*, 2000). $g(n)$ is the reduced normal-mode splitting due to phase-space filling and fermionic exchange interactions (Schmitt-Rink *et al.*, 1985).

If a polariton system consists of two helicity (spin) components, the biexcitonic attractive interaction between two excitons with opposite helicities (spins) plays a crucial role in its relaxation dynamics. A frequency-domain degenerate four-wave mixing (FD-DFWM) technique was used for such a system to evaluate relative magnitudes of the phase-space filling effect and the two-body attractive and repulsive interaction between excitons. As shown in Fig. 5(a), a pump beam excites two counterpropagating photon fields with amplitudes α_1 and α_2 and a test beam excites a probe field with an amplitude α_3. The elastic scattering conserving energy and momentum produces a phase-conjugate signal with an amplitude α_4. The nonlinear Hamiltonian of this elastic scattering has three terms,

$$\hat{H}_n = \hat{H}_1 + \hat{H}_2 + \hat{H}_3 + \mathrm{H.c.},$$

$$\hat{H}_1 = W(\hat{b}_{4+}^+ \hat{b}_{3-}^+ \hat{b}_{2+} \hat{b}_{1-} + \hat{b}_{4+}^+ \hat{b}_{3-}^+ \hat{b}_{2-} \hat{b}_{1+} + \hat{b}_{4-}^+ \hat{b}_{3+}^+ \hat{b}_{2+} \hat{b}_{1-} + \hat{b}_{4-}^+ \hat{b}_{3+}^+ \hat{b}_{2-} \hat{b}_{1+}),$$

$$\hat{H}_2 = R \sum_{\sigma=+,-} \hat{b}_{4\sigma}^+ \hat{b}_{3\sigma}^+ \hat{b}_{2\sigma} \hat{b}_{1\sigma}, \tag{40}$$

$$\hat{H}_3 = g\nu \sum_{\sigma=+,-} [\hat{b}_{4\sigma}^+ \hat{b}_{3\sigma}^+ \hat{b}_{2\sigma} \hat{a}_{1\sigma} + \hat{b}_{4\sigma}^+ \hat{a}_{3\sigma}^+ \hat{b}_{2\sigma} \hat{a}_{1\sigma}].$$

Here $\sigma = \pm$ represents the Z component of the angular momentum and $\hat{a}_\sigma$ and $\hat{b}_\sigma$ are the annihilation operators of the cavity photon and QW excitons, respectively. $\hat{H}_1$ represents attractive interactions between two excitons with opposite spins ($W < 0$). $\hat{H}_2$ represents the repulsive interaction between two excitons with the same spin. $\hat{H}_3$ represents the reduction of the exciton-photon coupling. In the presence of an exciton population $\langle \hat{b}^+ \hat{b} \rangle$, the exciton-photon coupling strength g is reduced to $g(1 - \nu\langle \hat{b}^+ \hat{b} \rangle)$, here $\nu > 0$.

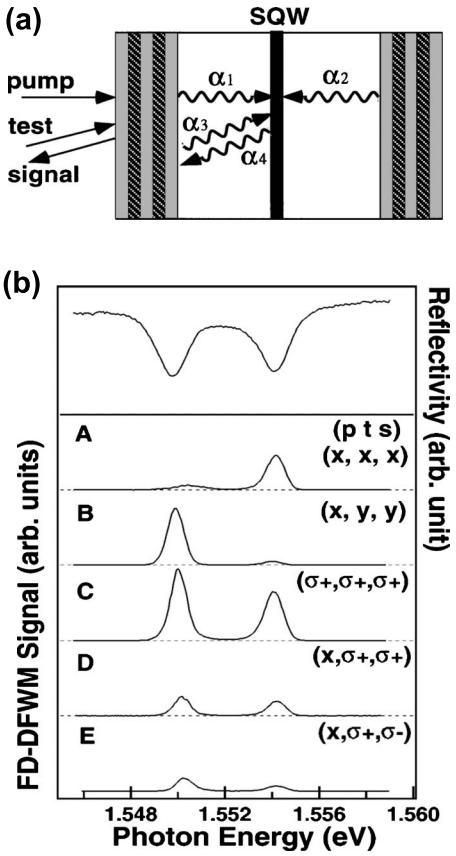

FIG. 5. Self-pumped four-wave mixing (phase conjugation) experiment. (a) Schematic of the experiment. Two initial fields provided by the pump beam are elastically scattered into two outgoing fields conserving energy and momentum. (b) Spectra of FD-DFWM at zero detuning for various polarization configurations. Adapted from Kuwata-Gonokami *et al.*, 1997.

Figure 5(b) shows the DFWM spectra at $\Delta = 0$ for different polarization configurations of the pump, test, and signal beams. When all three beams have the same linear polarization [in configuration (A)], a strong signal is observed at the UP resonance, while the signals at UP and LP resonances are expected to be proportional to $|W/4 + (R/2 - g\nu)|^2$ and $|W/4 + (R/2 + g\nu)|^2$, respectively. When the pump beam has a polarization orthogonal to that of the test and signal beams [in (B)], a strong signal appears at the LP resonance, where the signals at UP and LP resonances should be proportional to $|W/4 - (R/2 - g\nu)|^2$ and $|W/4 - (R/2 + g\nu)|^2$. In (C) and (D), the test and signal beams have the same helicity, so only H_2 and H_3 are effective. In (E) the two beams have opposite helicities so that only H_1 contributes to the scattering. The data are explained by a microscopic theory for nonlinear interaction coefficients based on an electron-hole Hamiltonian (Inoue *et al.*, 2000).

2. Polariton-polariton scattering rates

For a nonpolarized LP gas, following Tassone and Yamamoto (1999), we further simplify the scattering coefficient as

$$M \simeq 2\sum_{k,k'} V_{\vec{k}-\vec{k}'}\varphi_k\varphi_{k'}(\varphi_k^2 - \varphi_k\varphi_{k'}) \simeq 6E_0\frac{a_B^2}{S}, \tag{41}$$

where φ_k and E_0 are the screened 2D $1s$-exciton wave function and binding energy, respectively. $V_k = 2\pi/\epsilon_0 Sk$ is the 2D Coulomb potential and ϵ_0 is the dielectric function.

The corresponding LP transition probability is then

$$W^{\text{LP-LP}}_{k,k';k_1,k_2} = \frac{\pi}{\hbar}\frac{S^2}{(2\pi)^4} \times \frac{\Delta E^2 |M|^2 X_k^2 X_{k'}^2 X_{k_1}^2 X_{k_2}^2}{[\partial E(k')/\partial k'^2][\partial E(k_1)/\partial k_1^2][\partial E(k_2)/\partial k_2^2]} \times R(k,k',k_1,k_2). \tag{42}$$

A uniform energy grid is adopted with an energy spacing ΔE. The terms proportional to the 2D density of states $\partial E(k')/\partial k'^2$ stem from the conversion of integration over momenta to summation over energies. The term R is given by

$$R(k,k',k_1,k_2) = \int \frac{dq^2}{\sqrt{[(k+k_1)^2 - q^2][q^2 - (k-k_1)^2][(k'+k_2)^2 - q^2][q^2 - (k'-k_2)^2]}}. \tag{43}$$

The integration is taken over the range in which all four terms under the square root are non-negative. Energy conservation is built in by taking $k_2 = k(E_2 = E_k + E_{k'} - E_{k_1})$ and summing over the $E_{k'}$ and E_{k_1}.

C. Semiclassical Boltzmann rate equations

With these transition rates we formulate the semiclassical Boltzmann equations of the polariton distribution. This approach has been used before, for example, to describe the exciton condensation kinetics by Bányai *et al.* (2000), Tran Thoai and Haug (2000), and Bányai and Gartner (2002) and to describe the cavity polariton relaxation by Tassone *et al.* (1996, 1997), Bloch and Marzin (1997), Tassone and Yamamoto (1999), Cao *et al.* (2004), and Doan *et al.* (2005). In the latter two references the importance of a finite size for the 2D condensation kinetics has been shown.

The Boltzmann equations for the population of the excited states $n_k(t)$ and the ground-state population $n_0(t)$ are

$$\frac{\partial}{\partial t}n_{\vec{k}} = P_{\vec{k}}(t) - \frac{n_{\vec{k}}}{\tau_{\vec{k}}} + \left.\frac{\partial}{\partial t}n_{\vec{k}}\right|_{\text{LP-LP}} + \left.\frac{\partial}{\partial t}n_{\vec{k}}\right|_{\text{LP-}ph}, \tag{44}$$

$$\frac{\partial}{\partial t}n_0 = -\frac{n_0}{\tau_0} + \left.\frac{\partial}{\partial t}n_0\right|_{\text{LP-LP}} + \left.\frac{\partial}{\partial t}n_0\right|_{\text{LP-}ph}. \tag{45}$$

Note that a separate equation is needed for the ground-state LP population n_0 so as to properly account for the gap between the ground state and the lowest excited-state energies due to a finite size of the system. In the following, we assume cylindrical symmetry such that n_k depends only on the amplitude of $\vec{k}$, and we drop the vector notation for simplicity. $P_{\vec{k}}(t)$ is the time-dependent incoherent pump rate and $\tau_{\vec{k}}$ is the LP lifetime introduced by Bloch and Marzin (1997). For small transverse momenta $0 < k < k_{\text{cav}} = 8\ \mu\text{m}^{-1}$ we use $1/\tau_k = C_k^2/\tau_c$ given the photon Hopfield coefficient C_k. The cavity lifetime τ_c is only a few picoseconds for most microcavities. In the range $k_{\text{cav}} < k < k_{\text{rad}} = n_{\text{cav}}E_{\text{cav}}/\hbar c$, we use the nanosecond exciton lifetime τ^x, i.e., $1/\tau_k = 1/\tau_x$, and finally for large momenta $k > k_{\text{rad}}$ the exciton lifetime is infinite, i.e., $1/\tau_k = 0$.

The LP-phonon scattering rate is given by

$$\left.\frac{\partial}{\partial t}n_{\vec{k}}\right|_{\text{LP-}ph} = -\sum_{\vec{k}'}[W^{\text{LP-}ph}_{\vec{k}\to\vec{k}'}n_{\vec{k}}(1+n_{\vec{k}'}) - W^{\text{LP-}ph}_{\vec{k}'\to\vec{k}}(1+n_{\vec{k}})n_{\vec{k}'}]. \tag{46}$$

The LP-phonon scattering provides a dissipative cooling mechanism for the LP gas. It can reduce the excess energy introduced in the LP gas with the nonresonant optical excitation.

The LP-LP scattering rate is given by

$$\left.\frac{\partial}{\partial t}n_{\vec{k}}\right|_{\text{LP-LP}} = -\sum_{\vec{k}',\vec{k}_1,\vec{k}_2} W^{\text{LP-LP}}_{\vec{k},\vec{k}',\vec{k}_1,\vec{k}_2}[n_{\vec{k}}n_{\vec{k}'}(1+n_{\vec{k}_1}) \times (1+n_{\vec{k}_2}) - n_{\vec{k}_1}n_{\vec{k}_2}(1+n_{\vec{k}})(1+n_{\vec{k}'})], \tag{47}$$

where $\vec{k}_1 = \vec{k} + \vec{q}$ and $\vec{k}_2 = \vec{k}' - \vec{q}$. LP-LP scattering is rather fast; it thermalizes the LP gas in a few picoseconds but cannot reduce the total energy of the LP gas. Thus both scattering processes have their own distinct roles in the condensation kinetics of the LPs.

We emphasize again that the factor $1+n_0$ expresses the stimulated scattering into the ground state enhanced by the final-state occupation n_0, which are the essential driving forces of LP condensation. Once the condensate is degenerately populated with $n_0 \gg 1$, the escape of the

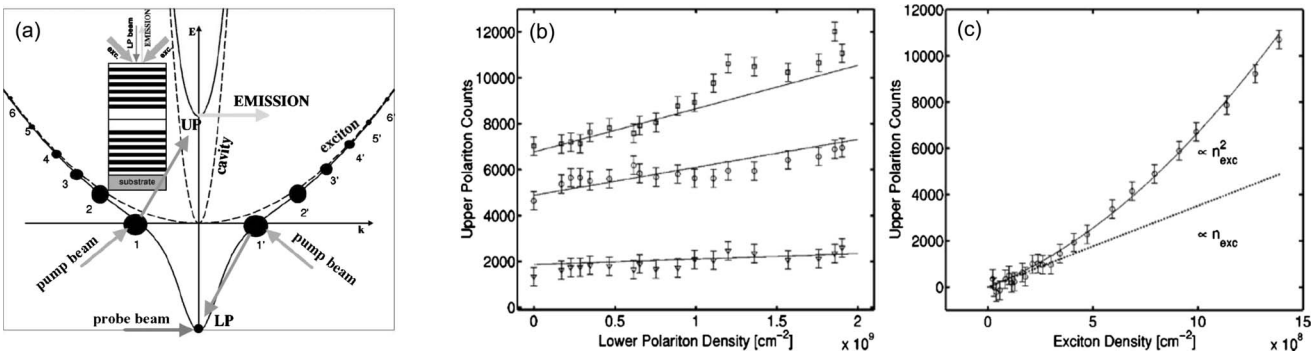

FIG. 6. A cold collision experiment of polaritons. (a) Schematic of the experiment. The size of the solid circles depicts the population in the LP states. Inset: The cross section of the microcavity structure and the experimental excitation scheme. (b) The integrated UP emission intensity as a function of probe density n_{LP} for varying exciton density n_{exc}. Symbols are the experimental data and solid lines are the theoretical prediction. The exciton densities are $n_{\mathrm{exc}}=1.5\times10^9$ (squares), 1.2×10^9 (circles), and 5.4×10^8 cm^{-2} (triangles). (c) The integrated UP emission intensity as a function of n_{exc} for a fixed $n_{\mathrm{LP}}=1.1\times10^9$ cm^{-2}. The dotted line indicates the acoustic phonon-scattering contribution to the UP intensity. Adapted from Huang *et al.*, 2000.

macroscopic coherent polariton wave is rather classical and given by the photon leakage out of the cavity.

To study spontaneous condensation, we keep the pump energy high enough to avoid the possibility where two LPs at the pumped mode can resonantly scatter into the ground state and a higher lying state (Savvidis *et al.*, 2000). The pump pulse is assume to be of the form

$$P_k(t) = P_k \times \begin{cases} e^{-2\ln[(2t/t_p)^2]} \\ \tanh(t/t_0) \end{cases} \tag{48}$$

with

$$P_k = P_0 e^{-\hbar^2(k-k_p)^2/2m_{\mathrm{exc}}\Delta E} \tag{49}$$

for pulse and stationary excitations, respectively.

For GaAs QW and microcavities, the material parameters we used are (Bockelmann, 1993; Pau *et al.*, 1995; Bloch and Marzin, 1997; Cao *et al.*, 2004) $E_0^x=1.515$ eV, $m_e=0.067m_0$, $m_h=0.45m_0$, $a_B=10$ nm, the index of refraction $n_{\mathrm{cav}}=3.43$, the normal-mode splitting $g_0=5$ meV, the deformation potentials $D_e=-8.6$ eV, $D_h=5.7$ eV, $u=4.81\times10^5$ cm/s, and $\rho=5.3\times10^3$ kg/m^3.

IV. STIMULATED SCATTERING, AMPLIFICATION, AND LASING OF EXCITON POLARITONS

In this section we describe cold collision experiments which demonstrate the bosonic final-state stimulation, matter-wave amplification, and lasing of polaritons. Through those experiments we investigate the nonlinear interactions of polaritons, which are at the heart of polariton condensation and the excitation spectrum discussed later.

A. Observation of bosonic final-state stimulation

One distinct feature of a system of identical bosonic particles is the final-state stimulation: the presence of N particles in a final state enhances the scattering rate into that final state by a factor of $1+N$. Final-state stimulation is the driving mechanism behind photon lasers and amplifier and is expected to be crucial to the formation of BEC. It is of great interest to demonstrate the final-state stimulation for a massive composite particle, to confirm its bosonic nature, and to clarify the role of final-state stimulation in the BEC physics.

Due to the strong coupling between excitons and photons, the energy DOS of the LPs decreases steeply by four orders of magnitude from a state at large in-plane wave number $k>k_{\mathrm{bot}}\sim0.1k_0$ to states at $k_\parallel\sim0$. Here we assume a moderate detuning and k_0 is the wave number of the cavity photon at $k_\parallel=0$. As a result of the reduced DOS, cooling of the LPs by acoustic phonon emission is slowed down at k_{bot}. At the same time, the lifetime of the LPs at k_{bot} states is typically two orders of magnitude longer than that of LPs at $k_\parallel\sim0$. The two effects together cause an accumulation of incoherent exciton population at k_{bot}—the so-called energy relaxation "bottleneck" (Pau *et al.*, 1995; Tassone *et al.*, 1996).

In an experiment on binary exciton scattering (Tassone and Yamamoto, 1999; Huang *et al.*, 2000), the bottleneck effect is utilized to study the bosonic final-state stimulation. As shown in Fig. 6(a), two pump beams create incoherent excitonlike LPs at $\boldsymbol{k}_\parallel=\pm\boldsymbol{k}_{\mathrm{bot}}$. Due to the long lifetime and slow relaxation rate at k_{bot}, the injected excitons form an incoherence reservoir. Then the LPs at $\boldsymbol{k}_\parallel=\pm\boldsymbol{k}_{\mathrm{bot}}$ may elastically scatter into LP and UP at $k_\parallel\sim0$. If a LP at $k_\parallel\sim0$ is optically populated, the exciton-exciton scattering rate is enhanced by the bosonic stimulation factor. The other final state of the scattering, the otherwise unpopulated $k_\parallel\sim0$ UPs, provides a background-free measurement window.

The sample used in this experiment is a single GaAs QW embedded in a planar AlAs/$Al_xGa_{1-x}As$ microcavity. A mode-locked Ti:Al_2O_3 laser with a bandwidth of 16 meV is spectrally filtered to obtain the pump and probe pulses which have a bandwidth of 0.4 meV and are separated in energy by half of the LP-UP splitting of 2 meV. The pump pulse is split into two beams and incident on the sample at ±45° from the sample normal.

The probe beam incidents on the sample at 3° in order to excite the LPs at $k_{\|}\sim 0$, while the UP emission is detected in the normal direction [Fig. 6(a)].

The time-integrated intensity of the UP emission N_{UP} increases linearly with the probe intensity [Fig. 6(b)], which is the signature of the final-state stimulation. N_{UP} also increases quadratically with the reservoir exciton density n_{exc} [Fig. 6(c)] due to the binary exciton-exciton scattering. The results are described quantitatively by a rate equation [solid lines in Figs. 6(b) and 6(c)], where the dominant term for populating the UPs is $\propto(1+N_{\mathrm{LP}})n_{\mathrm{exc}}^2$,

$$\frac{dN_{\mathrm{UP}}}{dt}=-\frac{N_{\mathrm{UP}}}{\tau_{\mathrm{UP}}}+a_{\mathrm{UP}}n_{\mathrm{exc}}+[b_{\mathrm{UP}}+b'(1+N_{\mathrm{LP}})]n_{\mathrm{exc}}^2. \tag{50}$$

Here τ_{UP} is the radiative lifetime of the UP and N_{LP} is the $k_{\|}\sim 0$ LP population determined by the probe beam intensity. The coefficient a_{UP} represents the scattering rate of a bottleneck exciton to an UP by acoustic phonon absorption and has been calculated by applying Fermi's golden rule to the Hamiltonian of the deformation-potential scattering. b_{UP} is the scattering rate of two excitons to one UP and another exciton (e.g., $1+6'\rightarrow \mathrm{UP}+4'$). b' is the scattering rate of two bottleneck excitons at opposite in-plane momenta $\pm k_{\|}$ to UP and LP both at $k_{\|}\approx 0(1+1'\rightarrow \mathrm{UP}+\mathrm{LP})$. b_{UP} and b' have been calculated via Fermi's golden rule rate applied to the Hamiltonian for exciton-exciton scattering.

In this cold collision experiment, real population of excitons at $\pm\vec{k}_{\mathrm{bot}}$ are excited by the pump laser and forms incoherent reservoirs. This is evident from the observed exponential decay of a luminescence from those exciton states with a time constant of $\tau_{\mathrm{exc}}\sim 190$ ps, which is much longer than the pump pulse duration of ~9 ps. Moreover, N_{UP} due to the stimulated scattering decays with a time constant of $\tau_{\mathrm{UP}}\sim 96$ ps. The difference of a factor of 2 between τ_{exc} and τ_{UP} stems from the n_{exc}^2 dependence of the stimulated scattering rate.

By contrast, the polariton parametric amplification experiment first performed by Savvidis *et al.* (2000) is a coherent optical mixing process. In this latter case, the pump beam creates virtual LP population at a magic wave number k_p, which coherently scatters to the two final states: LPs at $k_{\|}\sim 0$ and excitons at $\sim 2k_p$. The scattering conserves both in-plane momentum and energy between the initial and final states. In this coherent parametric process, the stimulated scattered signal appears only when the pump beam is present, and the signal intensity increases linearly with the pump intensity. In this sense, the process can be interpreted as coherent optical four-wave mixing resonantly enhanced by the LP resonances.

B. Polariton amplifier

A standard photon laser pumped just below its oscillation threshold is often used as a regenerative linear optical amplifier for an input light signal. It is a negative-conductance amplifiers based on incoherent (or resistive) gain elements. A second common type of amplifier is a nonlinear susceptance amplifier, the gain of which is based on coherent (or reactive) multiwave mixing between a pump, signal, and idler. A parametric amplifier is a classic example. This second type of amplifier has been demonstrated with matter waves using both BEC of alkali atoms (Inouye *et al.*, 1999; Kozuma *et al.*, 1999) and coherent polaritons produced by a pump laser (Savvidis *et al.*, 2000). Utilizing the stimulated scattering of bottleneck polaritons, Huang *et al.* (2002) demonstrated a matter-wave amplifier of the first type with a polariton system. The fundamental difference between a photon laser amplifier and a polariton amplifier is that, in the latter system, there is no population inversion between conduction and valance bands. Therefore the standard stimulated emission of photons cannot provide a gain. Instead, amplifications of the injected polaritons are achieved through elastic LP-LP scattering. Such a polariton amplifier is a matter-wave amplifier based on stimulated scattering of massive particles rather than a photon amplifier based on stimulated emission of photons. A negative-conductance amplifier for matter waves is attractive from a practical viewpoint because electrically injected incoherent excitons can eventually realize an amplifier for an optical signal without requiring population inversion between conduction and valence bands.

The sample used in the experiment by Huang *et al.* (2002) is a $\lambda/2$ $Cd_{0.6}Mg_{0.4}Te$ cavity with two CdTe QWs. A pump laser incident from a slant angle resonantly excites excitons at $k_{\|}\sim 3.5\ \mu\mathrm{m}^{-1}$. When this initial population increases to above about $N_p=7\times 10^{10}\ \mathrm{cm}^{-2}$, a quantum degeneracy threshold is reached at a bottleneck state with $k_{\|}=2\ \mu\mathrm{m}^{-1}$. N_p is nearly one order of magnitude smaller than the saturation density of $5\times 10^{11}\ \mathrm{cm}^{-2}$ for CdTe QW excitons. The measured LP population distribution versus energy and in-plane momentum is shown in Fig. 7(a). When pumped above threshold, the maximum of the LP emission continually shifts toward smaller $k_{\|}$. This behavior of bottleneck condensation is predicted by the rate equation theory (Tassone and Yamamoto, 1999). A slight blueshift of the LP energy at $k_{\|}\simeq 0$ and $\gtrsim 3\ \mu\mathrm{m}^{-1}$ is due to the repulsive interaction between nondegenerate LPs and the quantum degenerate bottleneck LPs at $k_{\|}\simeq 2\ \mu\mathrm{m}^{-1}$. The same feature is manifested in Bogoliubov excitation spectra as discussed in Sec. VIII.

When a probe pulse, with a narrow bandwidth of about 0.6 meV, selectively excites the bottleneck LPs, amplification of the probe beam is observed [Fig. 7(b)]. The dynamics of the bottleneck LP population N_{LP} is modeled by Ciuti *et al.* (1998),

$$\frac{dN_{\mathrm{LP}}}{dt}=P_{\mathrm{LP}}-\frac{N_{\mathrm{LP}}}{\tau_{\mathrm{LP}}}+a_{\mathrm{LP}}N_{\mathrm{EP}}(1+N_{\mathrm{LP}})+b_{\mathrm{LP}}N_{\mathrm{EP}}^2(1+N_{\mathrm{LP}}). \tag{51}$$

Here τ_{LP} is the bottleneck LP lifetime, P_{LP} is the external injection rate of the LP by the probe-laser pulse,

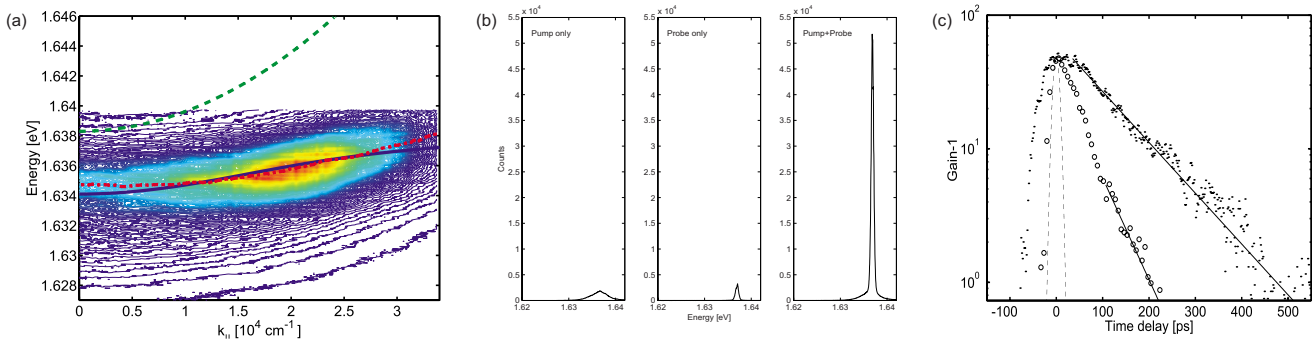

FIG. 7. (Color online) A negative conductance polariton amplifier. (a) The LP emission intensity taken as a function of energy and in-plane wave vector. The system is above the quantum degeneracy threshold at the bottleneck. The solid line and the dashed line indicate the theoretical dispersion of a single LP and cavity photon, respectively. The dashed line indicates the measured LP dispersion. (b) Observed probe emission for pump only, probe only, and simultaneous pump and probe excitation. (c) Gain −1 as a function of the time delay between pump and probe pulses (open circles). In the same plot, the intensity of bottleneck LP emission at a low pumping intensity is shown as solid dots. Solid lines indicate exponential decay curves of 57 and 114 ps. The dashed line indicates the convolution of the pump and the probe pulse envelopes for comparison. Adapted from Huang *et al.*, 2002.

$a_{\mathrm{LP}}=47\ \mathrm{s}^{-1}$ is the scattering rate between acoustic phonons and LPs, and $b_{\mathrm{LP}}=0.45\ \mathrm{s}^{-1}$ is the LP-LP scattering rate of an incoherent LP population.

The increase of the measured gain G with the reservoir population N_{EP} agrees quantitatively with the rate equation simulation, that is, $G\propto\exp(\mathrm{const}\times N_{\mathrm{EP}}^2)$ in the high-gain regime and $G-1\propto(\mathrm{const}\times N_{\mathrm{EP}}^2)$ in the low-gain regime. The time dependence of the gain is characterized by a fast rise followed by a slow exponential decay. The decay time of ~57 ps corresponds to about half of the separately measured decay time of bottleneck LPs [Fig. 7(c)], which is consistent with the quadratic dependence of the gain on N_{EP}. These results all confirm the gain mechanism by two-body scattering of incoherent reservoir LPs.

C. Polariton lasing versus photon lasing

1. Experiment

The LP-LP scattering enhanced by the bosonic final-state stimulation gives rise to large nonlinearity in the microcavity system. This large nonlinearity has been exploited to implement polariton amplifiers of incoherent type (Huang *et al.*, 2000) and of coherent type (Savvidis *et al.*, 2000) and polariton lasers in the bottleneck regime (Huang *et al.*, 2002). First-order coherence (Richard *et al.*, 2005) was also observed for a bottleneck polariton laser. However, such a system is always far from thermal equilibrium. There is a large number of degenerate lasing modes at the bottleneck, and it is difficult to characterize the thermodynamic properties of the LP gas. With the improvement of fabrication techniques and optimization of the experimental conditions, quantum degeneracy and lasing at the $k_{\parallel}=0$ LP ground state have been observed first with GaAs-based devices (Deng *et al.*, 2002, 2003; Balili *et al.*, 2007) and later with CdTe-based devices (Kasprzak *et al.*, 2006) and GaN-based devices (Christopoulos *et al.*, 2007).

GaAs excitons have a relatively larger Bohr radius, hence the advantage of relatively large scattering cross sections. To cope with the relatively lower saturation density and maintain the strong-coupling regime, Deng *et al.* (2002) used a microcavity with 12 QWs. Multiple QWs, on the one hand, reduced the exciton density per QW for a given total LP density and, on the other hand, increased the exciton-photon coupling to reach the very strong-coupling regime (Khurgin, 2001), which leads to reduced exciton Bohr radius for the LP branch hence further increased exciton saturation density.

The experimental scheme is depicted in the left panel of Fig. 10. A pump laser resonantly excites hot LPs at $k_{\parallel}=5-6\ \mu\mathrm{m}^{-1}$ so as to minimize the excitation of free electrons and holes, which usually increase the exciton decoherence rate. The value $k_{\parallel}=5-6\ \mu\mathrm{m}^{-1}$ is well above the magic angle corresponding to $k_{\parallel}\sim 2\ \mu\mathrm{m}^{-1}$, so that the coherent LP parametric amplification (Savvidis *et al.*, 2000) is avoided.

A typical lasing behavior is observed in the input-output relationship, i.e., the pump power dependence of the emission intensity of the LP ground state (Fig. 8). It features a sharp superlinear increase around a threshold pumping density P_{th}, corresponding to an injected carrier density of $n_{\mathrm{QW}}\approx 3\times 10^9\ \mathrm{cm}^{-2}$ per pulse per QW for a spot of $D\approx 15\ \mu\mathrm{m}$ in diameter. n_{QW} is 30 times smaller than the saturation density and two orders of magnitude smaller than the Mott density $n\sim 1/\pi a_B^2\sim 3\times 10^{11}\ \mathrm{cm}^{-2}$ electron-hole pairs per QW. At the threshold, the $k_{\parallel}=0$ LP population N_{LP} is estimated to be of the order of unity, which coincides with the onset of the stimulated scattering of LPs into the $k_{\parallel}\sim 0$ LP state.

To confirm that LPs remain as the normal modes of the system above threshold, the energy-momentum dispersion was measured and was found to agree with the LP dispersion instead of the cavity-photon dispersion. The LP energy remains well below the bare QW exciton energy in spite of a small blueshift due to the Coulomb

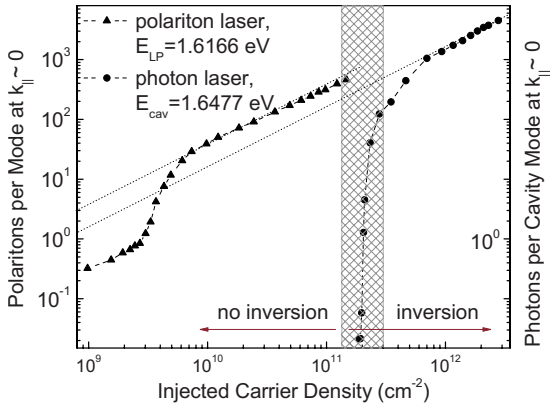

FIG. 8. (Color online) Number of LPs and cavity photons per mode vs injected carrier density for a polariton condensate (triangles, the scheme in the left panel of Fig. 10) and a photon laser (circles, the scheme in the right panel of Fig. 10), respectively. The gray zone marks the population inversion densities from band edge to 15 meV above the band edge. From Deng *et al.*, 2003.

exchange interaction and phase-space filling effect. The subject will be discussed in Sec. VIII.

To distinguish the polariton laser from a coherent polariton parametric amplifier, the time evolution of the LP ground-state population was measured. There was a clear delay between the peak of the LP emission and the pump pulse, which should be absent in the polariton parametric amplifier and oscillator (Savvidis *et al.*, 2000) see Fig. 9.

Using the same sample and experimental setup, a direct comparison has been made with a conventional photon laser (Deng *et al.*, 2003). Since the sample's cavity layer thickness is tapered by growth, detuning Δ of the cavity resonance changes across the sample. To establish photon lasing, the sample is pumped at a position with the cavity mode bluedetuned to 15 meV above the GaAs QW band edge. The pump energy is tuned accordingly to be resonant with the cavity mode energy at $k_{\parallel}=5.33\times10^4$ cm^{-1}. The experimental scheme is depicted in the right panel of Fig. 10.

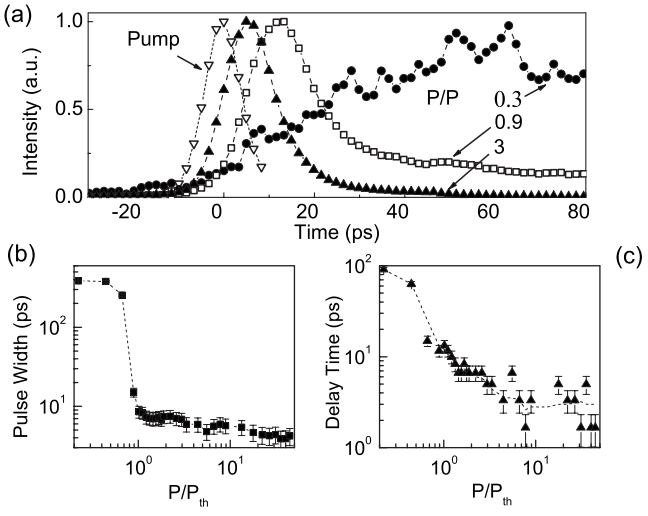

FIG. 9. Dynamic properties of the emission. (a) The time evolution of the $k_{\parallel}=0$ LP emission intensity. "a.u." in the y-axis label denotes "arbitrary units." (b) Pulse FWHM ΔT_p vs pump intensity $P/P_{\rm th}$. (c) Turn-on delay time of the emission pulse vs $P/P_{\rm th}$. From Deng *et al.*, 2002.

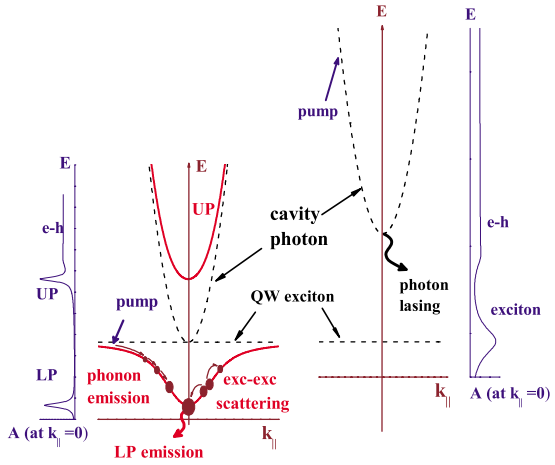

FIG. 10. (Color online) Schematics of the experimental principles for a photon laser (right panel) compared to LP condensation (left panel).

The emission in this case follows the cavity-photon dispersion, and a photon lasing threshold is observed at $k_{\parallel}=0$ (Fig. 8). Here the injected carrier density at threshold is $n'_{\rm QW}\approx3\times10^{11}$ cm^{-2} per pulse per QW, exactly identical to the density required for electronic population inversion at 15 meV above the band edge. This result agrees with the standard photon laser mechanism. That is, when the spontaneous emission coupling constant is large enough, the threshold of a semiconductor laser is solely determined by the electronic inversion condition (Björk *et al.*, 1994). The cavity-photon number per mode is estimated to be of the order of unity at threshold, which coincides with the onset of the stimulated emission of photons into the $k_{\parallel}=0$ cavity-photon mode.

A photon laser results from stimulated "emission" of photons into cavity modes with an occupation number larger than 1. The quantum degeneracy threshold of polaritons is triggered by the same principle of bosonic final-state stimulation, yet the physical process is different—it is stimulated "scattering" of massive quasiparticles (the LPs) from nonlasing states at $k_{\parallel}>0$ into the lasing state at $k_{\parallel}=0$. The nonlinear increase of the photon flux is an outcome of the leakage of the LPs via cavity mirrors. Hence the observed threshold of the polariton system requires no electronic population inversion. The threshold density is of the order of $\sim1/\lambda_T^2$ and three to four orders of magnitude lower than that of a photon laser threshold given by $\sim1/a_B^2$. It serves as a proof of principle demonstration to use polariton systems as a new energy efficient source of coherent light. The difference in the operational principles of polariton

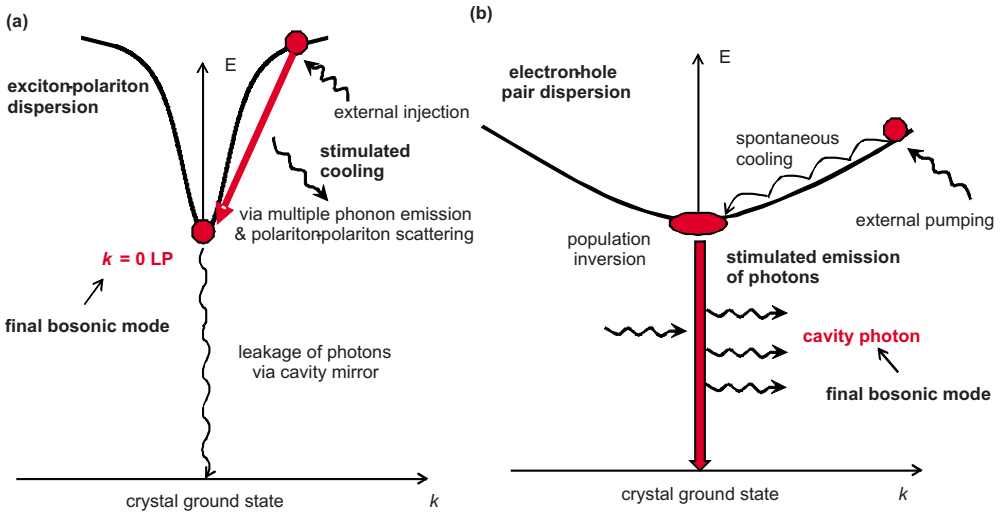

FIG. 11. (Color online) The operational principles of (a) polariton BEC and (b) photon laser. From Imamoglu *et al.*, 1996.

laser and photon laser is shown schematically in Fig. 11 (Imamoglu *et al.*, 1996).

If the pump power for a polariton lasing system is continuously increased, the 2D carrier density eventually exceeds the saturation density where the polariton system undergoes a transition from strong to weak coupling. When this transition happens, the leaking mode energy, which is approximately equal to the LP energy except for a continuous blueshift, suddenly jumps to the bare cavity resonant energy. Such behavior is shown in Fig. 12 for a 12-QW GaAs microcavity (Roumpos, Hoefling, *et al.*, 2009). In this particular experiment, continuous-wave pumping is used at an energy above the band gap. The first threshold is that of a polariton laser. Whether the second threshold is that of a simple photon laser (Bajoni *et al.*, 2008) or a new ordered state involving a BCS-type correlation is unresolved at this time.

2. Numerical simulation with quasistationary and pulsed pumping

Numerical solutions of the Boltzmann equation reproduced the above experimental results when both LP-phonon and LP-LP scattering are considered (Doan *et al.*, 2005). By quasistationary pumping above the bottleneck, a quantum statistically degenerate population of the ground state with $n_0 \gg 1$ is generated. This is shown in Fig. 13 where the ground-state population n_0 is plotted versus the total LP density n_{tot} taken as a measure of the pump rate for various values of the detuning Δ. It is seen that above the LP lasing threshold, the ground state is degenerate with 10^3–10^4 LPs. The total LP density n_{tot} at threshold is about 5×10^9 cm^{-2} for a detuning of 6 meV, which is well below the exciton saturation density $n_s=1.5\times10^{11}$ cm^{-2} (Schmitt-Rink *et al.*, 1985). The criteria for the validity of the boson approximation for polaritons are relaxed compared to those for excitons by the square of the exciton Hopfield coefficient. In experiments, the total LP density is distributed in several QWs which have no direct interaction. The condensation threshold density $n_{\mathrm{tot},c}=5\times10^{-9}$ cm^{-2} agrees with the experimental values (Deng *et al.*, 2003).

In Fig. 13 the important influence of the detuning parameter Δ on the condensation threshold is clearly dem-

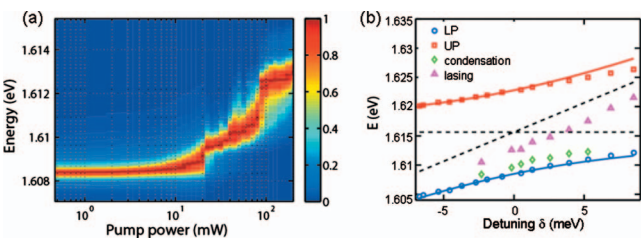

FIG. 12. (Color) Polariton lasing and photon lasing. (a) The emission energy vs pump power for a $N=12$ multi-QW planar microcavity. (b) The dispersion characteristics of polariton BEC (green diamond) and photon lasing (pink triangle) as well as the linear dispersion of UP (red square) and LP (blue circle) at low pump power. From Roumpos, Hoefling, *et al.*, 2009.

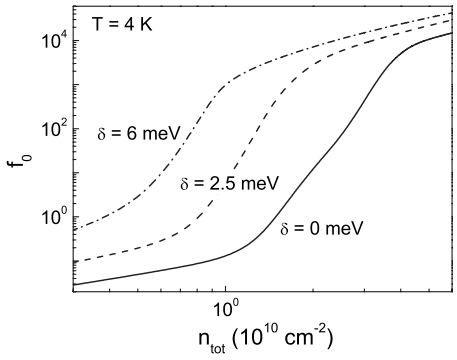

FIG. 13. Theoretical condensate population $f_0=n_0$ vs the total LP density n_{tot} for quasistationary pumping and the combined LP-LP and LP-phonon scattering for the bath temperatures of $T=4$ K for various values of the detuning: $\delta=0$ (full line), 2.5 (dashed line), and 6 meV (dash-dotted line). From Doan *et al.*, 2005.

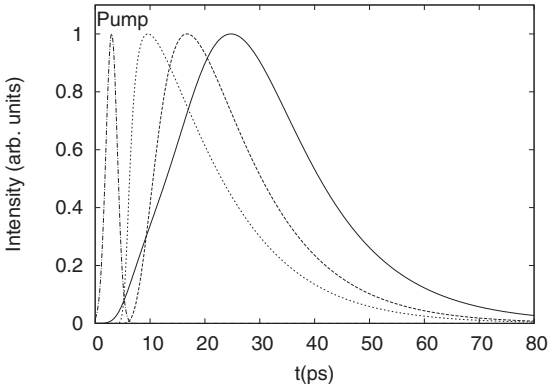

FIG. 14. Calculated buildup and decay of the ground-state emission in the laser mode above and below threshold at the pump powers $P/P_{\mathrm{th}}=0.87$ (solid line), 1.87 (dashed line), and 3.0 (dotted line), respectively. The dash-dotted line shows the pump pulse. From Doan *et al.*, 2005.

onstrated: If the cavity mode is slightly detuned in the order of a few meV above the exciton resonance, the exciton component of the LPs increases. Because all interactions relevant for the relaxation kinetics are provided by the exciton component, the LPs can relax more efficiently toward the ground state, so that the condensation threshold is reached at lower densities.

Under a pulse excitation below threshold, a relatively slow buildup and decay of the perpendicular emission are also obtained numerically. Above threshold the output rises faster due to the stimulated scattering (see Fig. 14). The decay is faster too because now an increasing fraction of the particles is in the ground state where the lifetime is the shortest. These results of the Boltzmann kinetics are in good agreement with the observation shown in Fig. 9 (Deng *et al.*, 2002; Weihs *et al.*, 2003).

V. THERMODYNAMICS OF POLARITON CONDENSATION

In Sec. IV, we show that stimulated scattering of LPs overcomes the bottleneck effect above a threshold pumping density; the population in the $k_{\parallel}=0$ LP ground state increases nonlinearly with the pump and quickly builds up quantum degeneracy. Quantum degeneracy is often associated with a transition to a macroscopic quantum state, such as a BEC state. To search for direct manifestation of such a phase transition, quantum statistics of the polariton gas has been studied by two types of measurements. One is the momentum-space distribution of polaritons, which reveals the evolution and formation of a condensate and its thermodynamic properties. It is the focus of this section. The other is coherence functions, specifically, first-order spatial and temporal coherence and second-order spatial and temporal coherence. These will be reviewed in Sec. VII. Other manifestations of the macroscopic phase include superfluidity, vortices, and phase locking among polariton arrays, as discussed later.

A. Time-integrated momentum distribution

As reviewed in Sec. II.E.4, a microcavity polariton system has the unique advantage that the momentum distribution of LPs can be directly measured via angle-resolved PL. Early studies revealed an energy relaxation bottleneck at relatively low excitation densities when the LP-phonon scattering was the dominant relaxation mechanism (Tassone *et al.*, 1997; Muller *et al.*, 1999; Tartakovskii *et al.*, 2000). With increasing excitation density, the bottleneck migrated toward smaller $k_{\parallel}$ state (Tartakovskii *et al.*, 2000). Later, in a GaAs-based 12-QW microcavity, the energy relaxation bottleneck became largely absent at zero or positive cavity detunings, and quantum degeneracy was achieved in the $k_{\parallel}=0$ LP ground state above certain excitation density P_{th} (Deng *et al.*, 2002). Following this experiment, Deng *et al.* (2003) measured the momentum distribution and compared it with Bose-Einstein (BE) statistics.

In the experiment of Deng *et al.* (2003), the microcavity system was pumped by a 3 ps pulsed laser on resonance with excitonlike states at large $k_{\parallel}$. The time-integrated momentum distribution of LPs was measured. For excitation densities between P_{th} and $2P_{\mathrm{th}}$, the LP ground state reached quantum degeneracy where stimulated scattering was pronounced; the energy relaxation time was close to but still longer than the lifetime of the ground-state LPs. Thus the LP distribution does not change significantly within the LP lifetime, while at the same time the duration of the emission pulse is comparable to their lifetime. In this regime, the time-integrated measurement approximates the instantaneous momentum distribution of the LPs. The measured momentum distribution agrees well with the quantum-mechanical BE distribution except for an extra population in the condensed $k_{\parallel}\sim 0$ state [Fig. 15(a)]. The quantum degeneracy parameter, the ratio of the chemical potential and temperature $\alpha=-\mu/k_B T_{\mathrm{LP}}$, decreases rapidly when the excitation density increased from below to above the threshold, reaching a minimum of $\alpha\sim 0.02$ at $P=1.7P_{\mathrm{th}}$ [Fig. 15(b)]. This demonstrates that the LPs form a quantum degenerate Bose gas and establish quasiequilibrium among themselves via efficient stimulated LP-LP scattering.

The fitted effective LP temperature T_{LP}, however, is higher than the lattice temperature of 4 K, and it increases with increasing pump rate [inset of Fig. 15(b)]. This implies that the LP-phonon scattering does not provide sufficient cooling to the injected hot excitons, and thermal equilibrium with the phonon bath is not reached.

At $P\gg P_{\mathrm{th}}$, the LP-LP interaction becomes strong. Therefore, the condensate begins to be depleted. At the same time, the dynamics becomes faster and the time-integrated data are no longer a good approximation of the instantaneous distribution.

B. Time constants of the dynamical processes

Whether or not LPs can be sufficiently cooled to reach thermal equilibrium with the phonon bath requires fur-

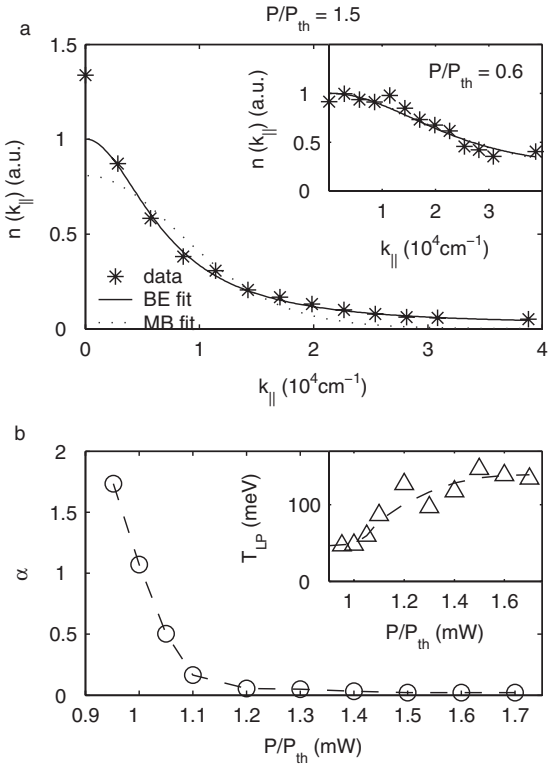

FIG. 15. Momentum space distribution of LPs. (a) The measured LP population per state vs $k_{\parallel}$ (stars), compared with BE (solid line) and MB (dotted line) distribution functions at pump rates $P/P_{\mathrm{th}}=1.5$ and 0.6 (inset). At $P/P_{\mathrm{th}}=0.6$, the fitted BE and MB distribution curves almost overlap. (b) The quantum degeneracy parameter α vs pump rate P/P_{th} and the fitted effective LP temperature T_{LP} vs pump rate (inset). The dashed lines are guides for the eye. From Deng *et al.*, 2003.

ther investigation of the dynamical processes of the system. As discussed in Sec. III, there are mainly three dynamical processes of the LP system: (1) LP decay via the out coupling of its photon component, (2) LP-LP scattering, and (3) LP-phonon scattering.

LP decay is characterized by the decay time $\tau_{\mathrm{LP}}=\tau_{\mathrm{cav}}/|C_{k_{\parallel}}|^2$, where $|C_{k_{\parallel}}|^2$ is the photon fraction of the LP defined in Eq. (16). The cavity lifetime is $\tau_{\mathrm{cav}}=1-100$ ps. For a given cavity, τ_{LP} increases with decreasing photon fraction. τ_{LP} is the shortest time scale for most microcavities at low pumping densities, leaving the system in nonequilibrium, sometimes with a relaxation bottleneck.

LP-LP scattering is a nonlinear process; its time scale $\tau_{\mathrm{LP\text{-}LP}}$ shortens with increasing LP density. When $\tau_{\mathrm{LP\text{-}LP}}$ becomes shorter than τ_{LP}, LPs overcome the energy relaxation bottleneck and reach quantum degeneracy threshold. Due to the efficient LP-LP scattering among states below the bottleneck, these LPs thermalize among themselves before they decay, establish quasiequilibrium, and form quantum degenerate BE distribution as presented in Sec. V.A. However, LP-LP scattering conserves the total energy of the LPs and thus does not reduce the temperature of the LP gas.

The only mechanism to cool the LPs is the LP-phonon scattering. The linear LP-phonon scattering is a rather slow energy relaxation process with a more or less fixed time scale $\tau_{\mathrm{phonon}}=10-50$ ps. Fortunately, in the quantum degenerate regime of $n_{k\sim 0}>1$, LP-phonon scattering can be significantly enhanced by the bosonic final-state stimulation. If τ_{phonon} shortens to less than τ_{LP}, LPs may have enough time to reach thermal equilibrium with the phonon bath within their lifetime.

C. Detuning and thermalization

To facilitate LP thermalization and eventually reach thermal equilibrium with the lattice, we need faster LP-phonon scattering and slower LP decay. For this purpose, there exists a simple and useful controlling parameter for the microcavity system: the detuning $\Delta=E_{\mathrm{cav}}-E_{\mathrm{exc}}$. At positive Δ, the excitonic fraction $X_{k_{\parallel}}$ increases, the LP effective mass is heavier, and the energy density of states $\rho(E)\propto(1-|X_{k_{\parallel}}|^2)^{-1}$ increases. Hence LP-phonon-scattering rates to low-energy states $[\propto X_{k_{\parallel},i}X_{k_{\parallel}\sim 0}\rho(E_i)]$ as well as LP-LP scattering rates to low-energy states $[\propto X_{k_{\parallel},i_1}X_{k_{\parallel},i_2}X_{k_{\parallel},f_1}X_{k_{\parallel}\sim 0}\rho(E_{i_1})\rho(E_{i_2})\times\rho(E_{f_1})]$ become larger. The flatter dispersion also requires less phonon-scattering events to thermalize the LPs below bottleneck. At the same time, the LP lifetime $\tau_{\mathrm{LP}}\approx\tau_{\mathrm{cav}}/(1-|X_{k_{\parallel}}|^2)$ becomes longer. All these are favorable for LPs to reach thermal equilibrium.

The compromise is a higher critical density due to a heavier effective mass, stronger exciton localization, and shorter dephasing time of the LPs. At very large positive detunings, these detrimental effects prevent clear observation of polariton condensation.

D. Time-resolved momentum distribution

Along this line, Deng *et al.* (2006) measured how the LP momentum distribution depends on the cavity detuning and obtained evidence of a thermal-equilibrium LP condensation at moderate positive detunings. In the experiment, a GaAs-based microcavity with 12 QWs and a 3 ps pulsed laser excitation were adopted. Time-resolved momentum distribution was measured by a streak camera with a time resolution of ~4 ps. From the time evolution of the LP ground-state population $N_{\mathrm{LP}}(k_{\parallel}=0)$, the energy relaxation time τ_{relax} of the LP system was extracted based on a two-mode rate equation model. The instantaneous momentum distribution $N_{\mathrm{LP}}(k,t)$ is compared with BE and MB distributions (Fig. 16).

The relaxation time τ_{relax} decreases sharply near the quantum degeneracy threshold, reflecting the onset of stimulated scattering into the LP ground state. At positive detunings and at pump levels above the quantum degeneracy threshold, τ_{relax} shortens to one-tenth of the lifetime $\tau_{\mathrm{LP}}(0)$ of the LP ground state, and thermal equilibrium with the phonon bath is established for a period of about 20 ps, with a chemical potential μ_{LP} of about $-0.1k_BT$. Near resonance ($|\Delta|<1$ meV), τ_{relax} is comparable to $\tau_{\mathrm{LP}}(0)$. The stimulated LP-LP scattering is still

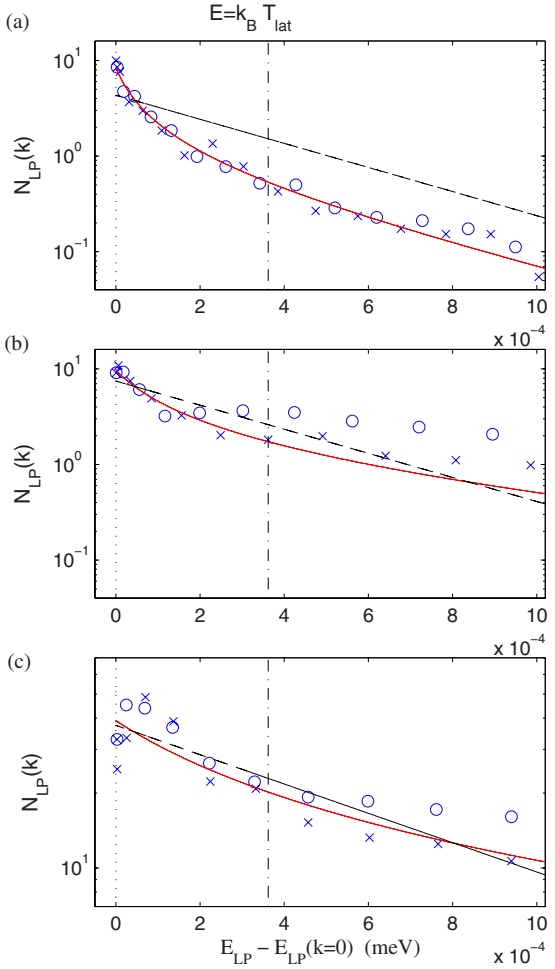

FIG. 16. (Color online) LP population per state $N(t,E)$ vs LP kinetic energy $E-E_0$ for different detunings at a time when T_{LP} reaches T_{min}: (a) $\Delta=6.7$ meV, $P\approx 4P_{\mathrm{th}}$; (b) $\Delta=-0.9$ meV, $P\approx 4P_{\mathrm{th}}$; and (c) $\Delta=-3.85$ meV, $P\approx 6P_{\mathrm{th}}$. Crosses are data taken from the incidence direction of the pump, open circles are from the reflection direction, solid lines are fitting by BE distribution, and dashed lines by MB distribution. Parameters for the curves are the following: (a) $T_{\mathrm{MB}}=4$ K, $T_{\mathrm{BE}}=4.4$ K, $\mu_{\mathrm{BE}}=-0.04$ meV; (b) $T_{\mathrm{MB}}=4$ K, $T_{\mathrm{BE}}=8.1$ K, $\mu_{\mathrm{BE}}=-0.13$ meV; and (c) $T_{\mathrm{MB}}=8.5$ K, $T_{\mathrm{BE}}=182$ K, $\mu_{\mathrm{BE}}=-0.4$ meV. From Deng *et al.*, 2003.

effective to achieve a quasiequilibrium BE distribution among LPs in $k_{\parallel}<1\ \mu\mathrm{m}^{-1}$ at a temperature T_{LP} significantly higher than the lattice temperature T_{lat} with a chemical potential $\mu_{\mathrm{LP}}=-0.01$ to $-0.1k_BT$. Finally, at large negative detunings, τ_{relax} is longer than $\tau_{\mathrm{LP}}(0)$, so the system never reaches equilibrium.

A quantum degenerate LP system, capable of reaching thermal equilibrium, is also valuable for studying the evolution from nonequilibrium to equilibrium phases, the distinction between classical and quantum systems, and the formation and dynamics of the order parameter of a quantum phase.

E. Numerical simulations

Numerical studies show that, with certain parameters, the kinetically calculated momentum distributions $n_k(t)$ of LPs can indeed be fitted by thermal distributions about 20–40 ps after the excitation, i.e., by the Maxwell-Boltzmann or Bose-Einstein distributions below or above threshold (Doan *et al.*, 2005; Doan, Thien Cao, *et al.*, 2008). Figure 17 shows a typical distribution calculated for 45 ps after the excitation pulse and with a lattice temperature of 4.2 K. Also plotted is a fit with a BE distribution. From the fit we obtain $T=5.5$ K and a degeneracy parameter $-\mu/kT=4.6\times10^{-3}$. The goodness of the fit shows that the LP gas has reached quasiequilibrium with well-defined temperature and chemical potential. These results agree with the experiments above (Deng *et al.*, 2006).

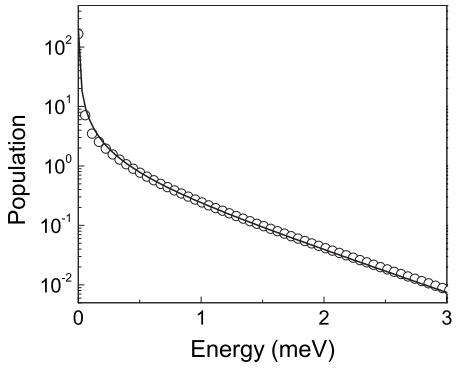

FIG. 17. Snapshot of the calculated LP energy distribution (circles) at 45 ps after the pulse excitation for a detuning of 4.5 meV. The full line shows the fit with a Bose-Einstein distribution with the temperature of 5.5 K and a chemical potential with the value $\mu=-2.8\times10^{-3}$ meV. From Doan, Thien Cao, *et al.*, 2008.

From the fits of the measured and calculated distributions one also obtains the still slowly varying parameters of the thermal distributions, namely, the temperature of the LP gas $T(t)=T_{\mathrm{pol}}$ and its chemical potential $\mu(t)$. Using these fits with a cavity lifetime of $\tau_c=2$ ps and a pump rate $P/P_{\mathrm{th}}=2$, the evolution of the LP temperature $T_{\mathrm{pol}}(t)$ normalized to the lattice temperature T_{lat} is shown in Fig. 18 for various values of the detuning. One sees that the temperature of LP gas reaches for a detuning of $\delta=4.5$ meV after about 60 ps. For lager times T_{pol} increases again because the low-energy LPs have a

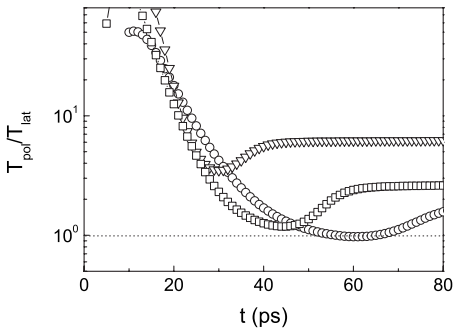

FIG. 18. Calculated normalized temperature vs time for three values of the detuning. $\delta=-1$ (triangles), 3 (squares), and 4.5 meV (circles). From Doan, Thien Cao, *et al.*, 2008.

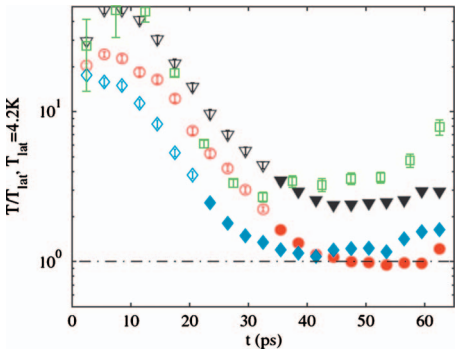

FIG. 19. (Color) Measured normalized temperature vs time for various values of the detuning for GaAs microcavities with a Rabi splitting of 14.4 meV and a normalized pump power $P/P_{\mathrm{th}}=3$ for a lattice temperature of 4.2 K. $\delta=-0.9$ (squares), 3.6 (triangles), 6.6 (diamonds), and 9.0 meV (circles). For the open symbols a full local equilibrium is not yet reached. From Deng *et al.*, 2006.

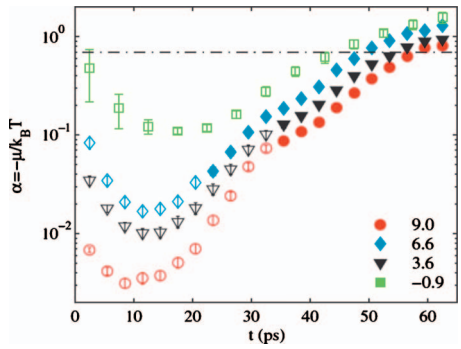

FIG. 21. (Color) Measured degeneracy parameter vs time for various values of the detuning measured for GaAs microcavities with a Rabi splitting of 14.4 meV and a normalized pump power $P/P_{\mathrm{th}}=3$ for a lattice temperature of 4.2 K. $\delta=-0.9$ (squares), 3.6 (triangles), 6.6 (diamonds), and 9.0 meV (circles). For the open symbols, a full local equilibrium is not yet reached. The dash-dotted line is the limit of quantum degeneracy with a ground-state population of 1. From Deng *et al.*, 2006.

smaller lifetime. This calculated relaxation kinetics of T_{pol} can be compared directly to the corresponding measurements of Deng *et al.* (2006), as shown in Fig. 19. Only where full symbols are shown, the gas was in good thermal equilibrium. The measured temperature of the LP gas also shows an improved temperature relaxation with increasing detuning. With a detuning of 6.6 meV the lattice temperature is reached after about 40 ps. Even with a detuning of 9 meV the lattice temperature is reached, while the numerical studies yield for this large detuning a less effective relaxation. This difference is mainly due to the larger Rabi splitting of the real system compared to the model system. In most other respects, e.g., the final increase of the temperature, the measured and calculated transient temperatures show the same trends.

For the same parameters the calculated degeneracy parameter $-\mu(t)/kT_{\mathrm{pol}}(t)$ is shown in Fig. 20 and the measured degeneracy parameters are shown in Fig. 21. Although quantum degeneracy is reached for smaller detunings at a slightly shorter delay, it stays much longer for larger blue detunings. The temporal range in which degeneracy exists extends over about 60 ps. The degeneracy is lost because the LP density decreases due to

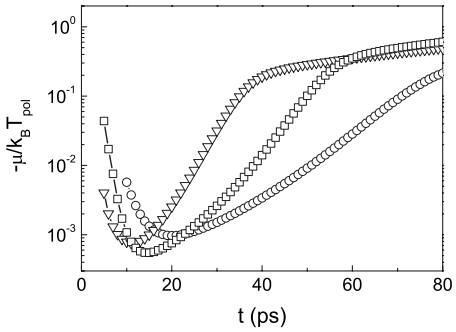

FIG. 20. Calculated degeneracy parameter vs time for three values of the detuning. $\delta=-1$ (triangles), 3 (squares), and 4.5 meV (circles). From Doan, Thien Cao, *et al.*, 2008.

emission from the ground state. The calculated pump dependences of the temperature and of the degeneracy parameter have been shown to agree qualitatively well with the corresponding measurements of Deng *et al.* (2006). These findings show that for favorable parameters a finite-size thermal-equilibrium BEC of LPs is possible.

F. Steady-state momentum distribution

Steady-state condensation of LPs was first reported in a CdTe/CdMgTe microcavity with 16 QWs, operating also at positive detunings (Kasprzak *et al.*, 2006). In this experiment, the excitation pulse duration of 1 μs is four orders of magnitude longer than the decay and energy relaxation times of the LPs. Therefore the time-integrated measurement reflects the steady-state properties of the system. Above the quantum degeneracy threshold, the high-energy tail of the time-integrated momentum distribution decays exponentially, indicating quasiequilibrium among LPs at an effective temperature of ~19 K (the lattice temperature is 5 K if neglecting heating by the excitation laser). The low-energy LP distributions are not described by a simple model, which is attributed to the relatively strong LP-LP interactions. A similar measurement was later performed with a GaAs-based microcavity, where an in-plane harmonic potential was implemented and LPs condense into the potential minimum. An effective LP temperature of ~100 K was measured (Balili *et al.*, 2007).

VI. ANGULAR MOMENTUM AND POLARIZATION KINETICS

Up to now, the spin and orbital angular momenta of excitons have not been considered explicitly. In this section, we formulate a pseudospin formalism and review experiments with circularly and linearly polarized pump-

ings and polarization dependent detection (Deng *et al.*, 2003; Renucci *et al.*, 2005; Kasprzak *et al.*, 2006).

A. Formulation of the quasispin kinetics

Shelykh *et al.* (2005) reviewed the theory of the exciton angular-momentum Boltzmann kinetics in microcavities. The spin kinetics was numerically evaluated taking into account the LP-phonon scattering, but the even more important LP-LP scattering was omitted. Recently Krizhanovskii *et al.* (2006) and Solnyshkov *et al.* (2007) studied spin kinetics including the LP-LP scattering for the case of resonant excitations. Here we formulate the kinetic equations for a nonresonantly pumped polariton system.

We consider only optically active exciton states (bright excitons) with the total angular momentum $m=\pm 1$. The 2×2 reduced density matrix $\rho_{k,ij}$ can be composed conveniently using the Pauli matrices σ_{ij}^{l},

$$\rho_{k,ij}(t) = \langle b_{k,j}^{\dagger}(t) b_{k,i}(t)\rangle \tag{52}$$

$$= \frac{N_k(t)}{2}\delta_{ij} + \sum_{l} S_k^{l}(t)\sigma_{i,j}^{l}, \tag{53}$$

$$\sigma^x = \begin{pmatrix} 0 & 1 \\ 1 & 0 \end{pmatrix}, \quad \sigma^y = \begin{pmatrix} 0 & -i \\ i & 0 \end{pmatrix}, \quad \sigma^z = \begin{pmatrix} 1 & 0 \\ 0 & -1 \end{pmatrix}. \tag{54}$$

The diagonal elements of $\rho_{k,ij}$ corresponds to the distribution functions $\rho_{k,ii}(t)=n_{k,i}(t)$ and we have

$$N_k(t) = \sum_{i=1}^{2} n_{k,i}(t), \tag{55}$$

$$S_k^z(t) = \frac{1}{2}[n_{k,1}(t) - n_{k,2}(t)]. \tag{56}$$

The off-diagonal elements give the x and y components of the spin-polarization amplitude,

$$S_k^x(t) = \frac{1}{2}[\rho_{k,12}(t) + \rho_{k,21}(t)], \tag{57}$$

$$S_k^y(t) = \frac{i}{2}[\rho_{k,12}(t) - \rho_{k,21}(t)]. \tag{58}$$

According to Cao *et al.* (2008), the Hamiltonian of the system is given by

$$\begin{aligned} H = {} & \sum_{k,s} e_k b_{k,s}^{\dagger} b_{k,s} + \frac{1}{2}\sum_{k} (\Omega_k b_{k,1}^{\dagger} b_{k,2} + \text{H.c.}) + \sum_{q,q_z} \omega_{q,q_z} a_{q,q_z}^{\dagger} a_{q,q_z} + \sum_{k,q,q_z,s} G(k,q,q_z)(a_{q,q_z}^{\dagger} + a_{-q,q_z}) b_{k+q,s}^{\dagger} b_{k,s} \\ & + \frac{1}{4}\Bigg\{ \sum_{k,k',q,s} V(k+q,k'-q,k,k')(b_{k,s}^{\dagger} b_{k',s}^{\dagger} b_{k'-q,s} b_{k+q,s}) + \sum_{k,k',q,s\neq s'} U(k+q,k'-q,k,k')(b_{k,s}^{\dagger} b_{k',s'}^{\dagger} b_{k'-q,s'} b_{k+q,s} \\ & + b_{k,s}^{\dagger} b_{k',s'}^{\dagger} b_{k'-q,s} b_{k+q,s'}) + \text{H.c.}\Bigg\}, \end{aligned} \tag{59}$$

where $a_{q,q_z}^{\dagger}$, a_{q,q_z} are the creation and annihilation operators of acoustic phonons, respectively. e_k is the dispersion of the LP branch. Ω_k is a complex energy, related to the TE-TM splitting of the microcavity. ω_{q,q_z} is the frequency of the acoustic phonon, with the in-plane wave number q and the wave number q_z perpendicular to the quantum well layers. $G(k,q,q_z)$ is the LP-phonon coupling constant. The matrix elements $V(k,k',k'-q,k+q)$ and $U(k,k',k'-q,k+q)$ describe scattering of LPs in the relative triplet and singlet configurations, respectively. They are given by (Shelykh *et al.*, 2005)

$$V(k,k',k'-q,k+q) = 6E_B a_B^2 X_{k+q} X_{k'-q} X_{k'} X_k,$$

$$\begin{aligned} U(k,k',k'-q,k+q) & \\ = -\alpha V(k,k',k'-q,k+q), & \quad \alpha > 0, \end{aligned} \tag{60}$$

$$T(k,k',k'-q,k+q) = V(k,k',k'-q,k+q) \times U(k,k',k'-q,k+q),$$

where E_B and a_B are the binding energy and Bohr radius of the exciton in two dimensions, respectively. Using the x and y components, we define a 2D polarization vector

$$\vec{S}_k = (S_k^x, S_k^y), \tag{61}$$

$$2\vec{S}_k\vec{S}_{k'} = \rho_{k,21}\rho_{k',12} + \rho_{k,12}\rho_{k',21}. \tag{62}$$

Similarly we decompose the TE-TM splitting into x and y components which form an effective 2D magnetic field (we absorb the g factor and magnetic moment in this effective field),

$$\Omega_k = \Omega_k^x + i\Omega_k^y, \tag{63}$$

$$\vec{\Omega}_k = (\Omega_k^x, \Omega_k^y),$$

where the components of the splitting field have been given by Kavokin *et al.* (2004, 2005) as

$$\Omega_k^x = \Omega_k \frac{k_x^2 - k_y^2}{k^2} = \Omega_k \cos(2\phi),$$
$$\Omega_k^y = \Omega_k \frac{2k_x k_y}{k^2} = \Omega_k \sin(2\phi). \tag{64}$$

Here ϕ is the polar angle of the in-plane momentum vector, i.e., $k_x = k\cos(\phi)$, $k_y = k\sin(\phi)$. The momentum dependence of the splitting field (64) is due to the TE-TM splitting of the microcavity modes, together with the momentum dependence of the optical matrix elements of the exciton longitudinal-and-transverse splitting. From the equations of the motion, we get the kinetic equations of the distribution function $n_{k,i}$ and in-plane pseudospin $\vec{S}_k$. For $n_{k,j}$,

$$\frac{\partial n_{k,j}}{\partial t} = -\frac{n_{k,j}}{\tau_k} + \left.\frac{\partial n_{k,j}}{\partial t}\right|_{S\text{-}F} + \left.\frac{\partial n_{k,j}}{\partial t}\right|_{mf\text{-}s\text{-}s} + \left.\frac{\partial n_{k,j}}{\partial t}\right|_{\text{scatt}}^{\text{LP-ph}} + \left.\frac{\partial n_{k,j}}{\partial t}\right|_{\text{scatt}}^{\text{LP-LP}} + \frac{1}{2}p_j P(k,t), \quad j = 1,2. \tag{65}$$

Here the changes due to the splitting field are given by

$$\left.\frac{\partial n_{k,j}}{\partial t}\right|_{S\text{-}F} = -\frac{1}{\hbar}(-1)^j \vec{e}_z[\vec{S}_k \times \vec{\Omega}_k]. \tag{66}$$

The mean-field term due to the interaction of singlet LPs is given by

$$\left.\frac{\partial n_{k,j}}{\partial t}\right|_{mf\text{-}s\text{-}s} = \frac{2}{\hbar}(-1)^j \sum_q U(k,q,k,q)|\vec{S}_k \times \vec{S}_q|. \tag{67}$$

For $\vec{S}_k$,

$$\frac{\partial \vec{S}_k}{\partial t} = -\frac{\vec{S}_k}{\tau_{ks}} + \left.\frac{\partial \vec{S}_k}{\partial t}\right|_{S\text{-}F} + \left.\frac{\partial \vec{S}_k}{\partial t}\right|_{mf\text{-LP-LP}} + \left.\frac{\partial \vec{S}_k}{\partial t}\right|_{\text{scatt}}^{\text{LP-ph}} + \left.\frac{\partial \vec{S}_k}{\partial t}\right|_{\text{scatt}}^{\text{LP-LP}} + \frac{1}{2}\vec{e}_p P(k,t). \tag{68}$$

Here the mean-field term due to the LP-LP interaction is

$$\left.\frac{\partial \vec{S}_k}{\partial t}\right|_{mf\text{-LP-LP}} = \frac{2}{\hbar}\sum_q [V(k,q,k,q) - U(k,q,k,q)] \times (f_{q,1} - f_{q,2})[\vec{e}_z \times \vec{S}_k], \tag{69}$$

where $\vec{e}_z$ is the unit vector along the growth axis and p_j and $\vec{e}_p$ denote components of the pump polarization in the z direction and (x,y) plane, respectively. $p_1 = 2$, $p_2 = 0$ for the circular pump and $p_1 = p_2 = 1$ for the linear pump. The changes of the in-plane polarization due to the splitting field are given by

$$\left.\frac{\partial \vec{S}_k}{\partial t}\right|_{S\text{-}F} = \frac{1}{\hbar}\left(\frac{f_{k,1} - f_{k,2}}{2}\right)\vec{e}_z \times \vec{\Omega}_k. \tag{70}$$

The in-plane pseudospin lifetime can be estimated as $\tau_{ks}^{-1} = \tau_k^{-1} + \tau_{sl}^{-1}$, where τ_{sl} is the characteristic time of the spin-lattice relaxation. The scattering terms in Eqs. (65) and (68) in the cylindrical approximation are put together in the Appendix according to Cao *et al.* (2008).

As a simplifying approximation, we follow Cao *et al.* (2008) and assume a cylindrical symmetry (Kavokin *et al.*, 2004) so that the polarization has only the radial component $\vec{S}_k = S_k^r \vec{e}_r$ and the splitting field is taken to be orthogonal to the polarization vector. This assumption does not take into account certain directional properties of the splitting field, but such effects are relatively small with respect to the presently investigated aspects of the spin kinetics. Using this cylindrical symmetry we obtain the following set of equations for $n_{k,j}$ and the radial component S_k^r of the in-plane spin polarization:

$$\frac{\partial n_{k,j}}{\partial t} = -\frac{n_{k,j}}{\tau_k} + \left.\frac{\partial n_{k,j}}{\partial t}\right|_{S\text{-}F} + \left.\frac{\partial n_{k,j}}{\partial t}\right|_{\text{scatt}}^{\text{LP-ph}} + \left.\frac{\partial n_{k,j}}{\partial t}\right|_{\text{scatt}}^{\text{LP-LP}} + \frac{1}{2}p_j P(k,t), \quad j = 1,2, \tag{71}$$

$$\frac{\partial S_k^r}{\partial t} = -\frac{S_k^r}{\tau_{ks}} + \left.\frac{\partial S_k^r}{\partial t}\right|_{S\text{-}F} + \left.\frac{\partial S_k^r}{\partial t}\right|_{\text{scatt}}^{\text{LP-ph}} + \left.\frac{\partial S_k^r}{\partial t}\right|_{\text{scatt}}^{\text{LP-LP}} + \frac{1}{2}|\vec{e}_p|P(k,t), \tag{72}$$

where the splitting field terms reduce to

$$\left.\frac{\partial n_{k,j}}{\partial t}\right|_{S\text{-}F} = -\frac{1}{\hbar}(-1)^j S_k^r \Omega_k \tag{73}$$

and

$$\left.\frac{\partial S_k^r}{\partial t}\right|_{S\text{-}F} = \frac{1}{\hbar}\left(\frac{n_{k,1} - n_{k,2}}{2}\right)\Omega_k. \tag{74}$$

The mean-field terms due to the LP-LP interactions (67) and (69) vanish in the cylindrical approximation due to the angle integration. For the scattering terms in Eqs. (71) and (72) in the cylindrical approximation we refer to the appendix of Cao *et al.* (2008).

B. Time-averaged and time-resolved experiments and simulations

To compare with experiments, we use $\tau^x = 30$ ps, $\tau^c = 2$ ps, and $\tau_{sl} = 15$ ps. The smallness parameter of the interaction between excitons in the relative singlet state is $\alpha = 5\times10^{-2}$. The bath temperature is $T = 4$ K. The detuning between the cavity mode and the exciton resonance is assumed to be zero. The pump is centered at $k_p = 1.7\times10^5$ cm^{-1} with a linewidth $\Delta E = 0.1$ meV. The pump pulse width is as in the experiment of Deng *et al.* (2003), $t_p = 3$ ps.

First we examine the time-averaged ground-state LP population for a circularly polarized pump pulse. Here we use the total number of injected LPs as a measure of the pump power. As expected, the LP population at $k_\parallel$

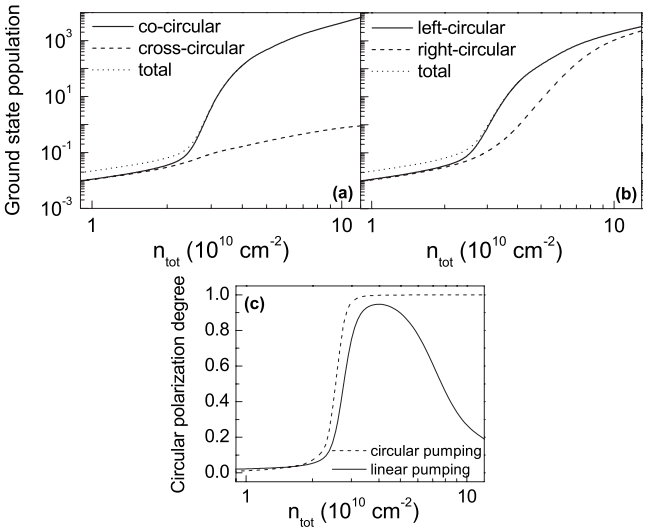

FIG. 22. LP ground-state population vs total LP density under pumping (a) with circularly polarized and (b) with linearly polarized light at $T=4$ K in a GaAs microcavity. The sum of the two ground-state populations is given by the dotted line, the spin-up LP population by the solid line, and the spin-down population by the dashed line. (c) Circular degree of polarization of light emitted from the ground state. For linearly polarized pumping the light intensity is given by the solid line for circularly polarized pumping by the dashed line. From Cao *et al.*, 2008.

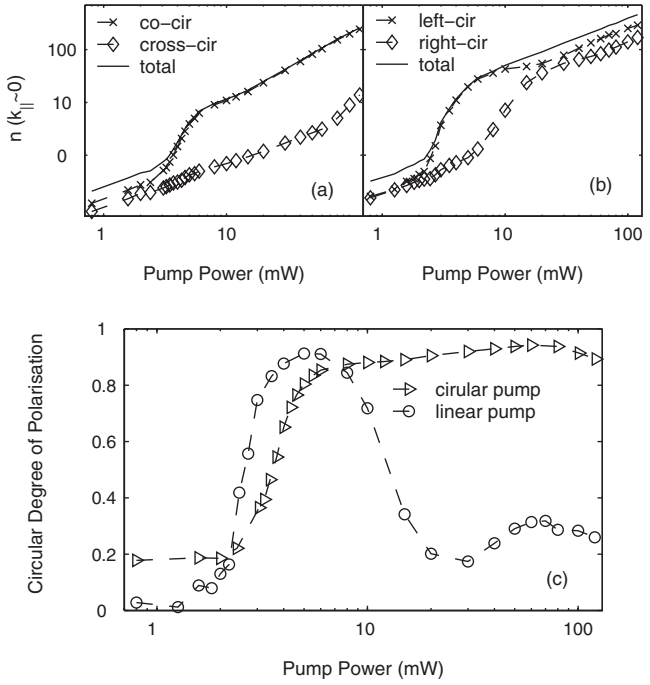

FIG. 23. The measured time-averaged polarization properties of a GaAs microcavity. Emitted light intensity of the LP ground state (a) for circularly polarized and (b) for linearly polarized pump light. (c) The circular degree of polarization is plotted for pumping with linear and circular polarizations. From Deng *et al.*, 2003.

=0 with cocircular polarization exhibits a clear condensation threshold [solid line in Fig. 22(a)], while the population with cross-circular polarization [dashed line in Fig. 22(a)] stays subcritical up to a total LP density of 10^{11} cm^{-2}, where it is about four orders of magnitude smaller than the cocircular density.

Next we calculate the ground-state LP population for left- and right-circular polarizations when the pump pulse is linearly polarized. Figure 22(b) shows that due to the TE-TM splitting the ground-state population for the left-circular LPs (solid line) has a lower threshold, while the right-circular LPs also condense but at about a factor of 3 higher pump rate. At the highest pump rates, the ground-state populations of both circular polarizations become equal. Finally, we plot in Fig. 22(c) the circular degree of polarization, i.e., the normalized difference between the ground-state populations of the left- and right-circular LPs for circularly and linearly polarized pump light. For circular pump the degree of polarization increases rapidly at the condensation threshold and approaches a value close to 1. For linearly polarized pumping the degree of polarization increases to a value of about 0.95 but decreases rapidly when the right-circular LPs condense and approach a value close to 0 at the highest pump rates. Comparison with the experimental results in Fig. 22 (Deng *et al.*, 2003) shows good qualitative agreement. In particular, the absence of a threshold for the cross-circularly polarized LPs for circular pumping is clearly shown in Figs. 22(a) and 23(a). Similarly the successive condensations of the left- and right-circular LPs separated by about a factor of 3 in corresponding threshold pump rates in Figs. 22(b) and 23(b) agree well. Finally, the degree of polarization for circular pumping remains high in both theory and experiment [see Figs. 22(c) and 23(c)], while the degree of polarization for linearly polarized pumping decreases above the threshold.

In Fig. 24 the calculated time evolution of the degree of circular polarization for a circular pump is shown for various total LP densities. The results can be compared with corresponding measurements of Renucci *et al.*

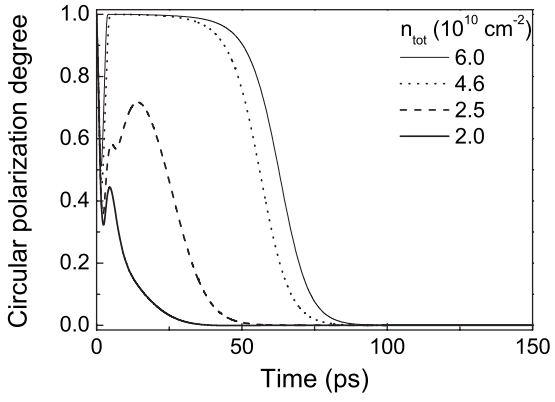

FIG. 24. Calculated time dependence of the circular degree of polarization for circularly polarized near-resonant 3 ps pump pulses which excite a total LP density of $N_{\mathrm{tot}}=2.0\times10^{10}$, 2.5×10^{10}, 4.6×10^{10}, and 6.0×10^{10} cm^{-2}. From Doan, Cao, *et al.*, 2008.

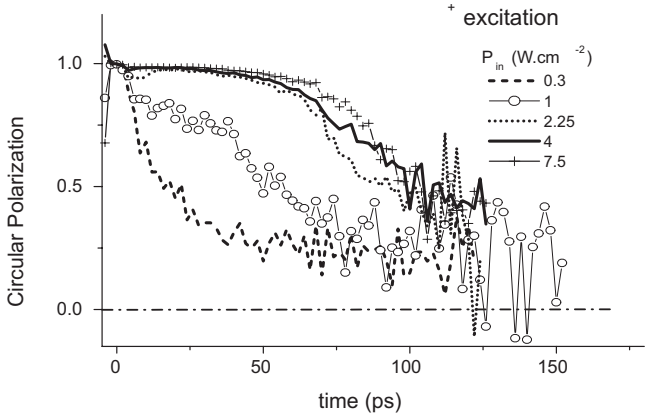

FIG. 25. Measured time dependence of the circular degree of polarization for circularly polarized pump pulses in GaAs microcavities. From Renucci *et al.*, 2005.

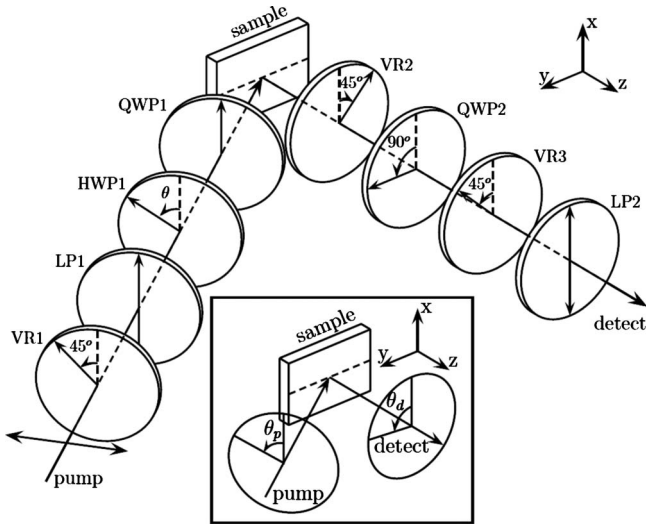

FIG. 26. The polarization measurement setup. Vectors label the fast or polarization axes of the optical components. The laser pump is initially horizontally polarized ($\theta_p=90°$) and is incident at an angle of 55° with respect to the growth direction z. Luminescence is collected along the z axis. The first variable retarder (VR1) and linear polarizer (LP1) work as a variable attenuator. By rotating a half wave plate (HWP1), and using a removable quarter wave plate (QWP1), we can implement various polarization states for the pump. The second variable retarder (VR2) is used as a zero, half, or quarter wave plate. The combination of a quarter wave plate (QWP2), variable retarder (VR3), and linear polarizer (LP2) is used for detection of a particular linear polarization state, depending on the retardance of VR3. Inset: Definition of angles θ_p and θ_d corresponding to the polarization axes of the pump and detection, respectively (Roumpos, Lai, *et al.*, 2009).

(2005) as shown in Fig. 25, where a resonant excitation has been used. In both theory and experiment, the degree of polarization decays rapidly below threshold but quickly approaches 1 around threshold. With increasing pump rate, the degree of polarization remains close to 1 for about 30–70 ps, followed by a steep decay. Particularly striking is the difference in time evolution below and above the threshold, as well as the trend of a longer lasting degree of polarization at higher pump rates.

C. Stokes vector measurement

The polarization state of emission, which has a one-to-one correspondence to the quasispin state of the internal polariton condensate, is characterized by the Stokes vector (S_1,S_2,S_3) defined as

$$S_1=\frac{I_{0°}-I_{90°}}{I_{0°}+I_{90°}},\quad S_2=\frac{I_{45°}-I_{-45°}}{I_{45°}+I_{-45°}},\quad S_3=\frac{I_L-I_R}{I_L+I_R}. \quad (75)$$

$I_{0°}$, $I_{90°}$, $I_{45°}$, and $I_{-45°}$ are the intensities of the linearly polarized components at detection angles $\theta_d=0°$, 90°, 45°, and −45°, respectively, as defined in Fig. 26. I_L and I_R are the intensities of the left- and right-circularly polarized components, respectively. The degree of linear polarization (DOLP) and the angle of the dominant linear polarization ψ are calculated as

$$\mathrm{DOLP}=\sqrt{S_1^2+S_2^2},\quad \psi=\frac{1}{2}\tan^{-1}\left(\frac{S_2}{S_1}\right). \quad (76)$$

The degree of circular polarization is simply given by the parameter S_3.

In Fig. 27(a), the measured intensity for the linearly polarized light along $\theta_d=0°$ and 90° is shown as a function of pump power in units of the injected polariton density per pulse QW (Roumpos, Lai, *et al.*, 2009). The pump is horizontally polarized ($\theta_p=90°$). The three Stokes parameters defined above are plotted in Fig. 27(b). Notice that the circular polarization (S_3) develops just above threshold but the linear polarization (S_1) takes over well above threshold. For circularly polarized pump [Fig. 27(c)], the emission is circularly polarized up to $S_3=-99.4\%$.

If we rotate the direction (θ_p) of the linearly polarized pump [Figs. 27(d) and 27(e)], the polarization direction is always rotated by ~90° from the pump polarization. Also, a circularly polarized component has S_3 changing sign for varying θ_p [Fig. 27(f)]. The sign change is correlated with the deviation of $\psi-\theta_p$ from 90° as shown in Fig. 27(e).

The above quasispin dynamics can be understood in terms of spin-dependent Boltzmann equations (Roumpos, Lai, *et al.*, 2009). In particular, the quantum interference effect between the repulsive scattering among isospins and the attractive scattering among heterospins is responsible for the observed 90° rotation of the linear polarization shown in Fig. 27(e). This is fully compatible with the discussion on the LP-LP interaction in Sec. III.B.

VII. COHERENCE PROPERTIES

In BEC, a macroscopic number of particles occupy a single-quantum state and manifest quantum correlations on the macroscopic scale. The wave function of the con-

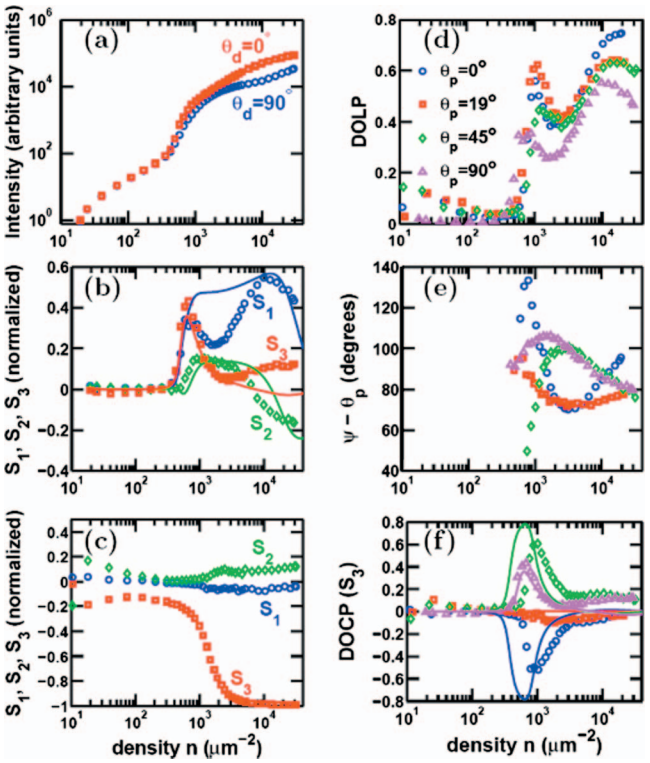

FIG. 27. (Color) Measurement of Stokes parameters (markers) compared with the theoretical model (solid lines). (a) Horizontal pumping ($\theta_p=90°$). Collected luminescence for $\theta_d=0°$ (red squares) and $\theta_d=90°$ (blue circles) vs injected particle density in μm^{-2} per pulse per QW. A clear threshold is observed at 5×10^2 μm^{-2}. Degree of polarization measurement for (b) $\theta_p=90°$ linear pumping and (c) left circularly polarized pumping. Blue circles: S_1, green diamonds: S_2, and red squares: S_3 defined in Eq. (75). Calculated polarization parameters from the measurement of the Stokes parameters for linear pumping [Eqs. (75) and (76)]. (d) DOLP. (e) Angle for major axis of linear polarization ψ relative to θ_p. (f) Degree of circular polarization (S_3) (Roumpos, Lai, *et al.*, 2009).

densate serves as the order parameter; its density matrix has finite off-diagonal elements, often referred to as off-diagonal long-range order (Penrose and Onsager, 1956; Beliaev, 1958; Yang, 1962), which can be measured through the first-order coherence functions. Second- and higher-order coherence functions of the state further characterize the nature of a quantum state and distinguish it from a thermal mixture (Glauber, 1963; Gardiner and Zoller, 2000). We review in this section studies of the coherence functions of the LP condensates and discuss next special properties of the macroscopic quantum state, such as the first-sound mode and superfluidity due to broken gauge symmetry, appearance of quantized vortices, and phase locking among multiple condensates.

A. The second-order coherence function

The temporal intensity-intensity correlation function is the lowest-order coherence function which characterizes the statistical nature of a quantum state. It has been of crucial importance in characterizing the coherence properties of laser light. For polaritons, it was first measured by Deng *et al.* (2002) for a GaAs microcavity with 2 ps photon lifetime. Recently it was measured for a GaAs microcavity with 80 ps LP lifetime by Roumpos, Hoefling, *et al.* (2009) and also for a CdTe microcavity by Kasprzak *et al.* (2008). A first attempt to explain the second-order coherence measurements was given by Laussy *et al.* (2004, 2006) in terms of a coupled Boltzmann equation and master equation kinetics. The model was extended by Doan, Cao, *et al.* (2008) to reach better agreement with experiments.

The time-domain second-order coherence function $g^{(2)}(\tau)$ is defined as (Glauber, 1963)

$$g^{(2)}(\tau)=\frac{\langle\hat{E}^{(-)}(t)\hat{E}^{(-)}(t+\tau)\hat{E}^{(+)}(t+\tau)\hat{E}^{(+)}(t)\rangle}{\langle\hat{E}^{(-)}(t)\hat{E}^{(+)}(t)\rangle^2}, \tag{77}$$

where $\hat{E}^{(-)}(t)$ and $\hat{E}^{(+)}(t)$ are the negative and positive frequency parts of the electric-field operator at time t, respectively. $g^{(2)}(\tau)$ measures intensity correlation of the field between time t and $t+\tau$. If $\hat{E}(t)$ and $\hat{E}(t+\tau)$ are uncorrelated but stationary,

$$g^{(2)}(\tau)=\frac{\langle\hat{E}^{(-)}(t)\hat{E}^{(+)}(t)\rangle\langle\hat{E}^{(-)}(t+\tau)\hat{E}^{(+)}(t+\tau)\rangle}{\langle\hat{E}^{(-)}(t)\hat{E}^{(+)}(t)\rangle^2}=1.$$

For a single-mode state, the maximum correlation (or anticorrelation) is obtained at $\tau=0$, i.e., by $g^{(2)}(\tau=0)$ which has the following property:

$$g^{(2)}(0)=2, \quad \text{thermal state},$$

$$g^{(2)}(0)=1-\frac{1}{n}, \quad \text{number state } |n\rangle,$$

$$g^{(2)}(0)=1, \quad \text{coherent state}.$$

Thus defined normalized second-order coherence functions are independent of linear losses between the source and detector. Moreover, while spectrally filtered thermal light can be brought into interference after a Michelson interferometer, its $g^{(2)}(0)$ value remains unchanged. These properties make $g^{(2)}(0)$ especially useful in identifying the quantum-statistical nature of a state.

Caution is needed, however, given the finite experimental time resolution. When τ is much longer the coherence time τ_c of the field, $g^{(2)}(\tau)$ decays to 1. Thus a detector time resolution much larger than τ_c will make accurate measurement of $g^{(2)}(0)$ difficult.

1. $g^{(2)}(0)$ of the LP ground state

Deng *et al.* (2002) first measured the second-order temporal coherence function of a condensate. A Hanbury Brown–Twiss-type setup (Hanbury Brown and Twiss, 1956) is adopted, mainly consisting of a 50/50 beam splitter and two single-photon counters (Fig. 28). In this pulsed experiment, since the polariton dynamics is much faster than the time resolution of the photon

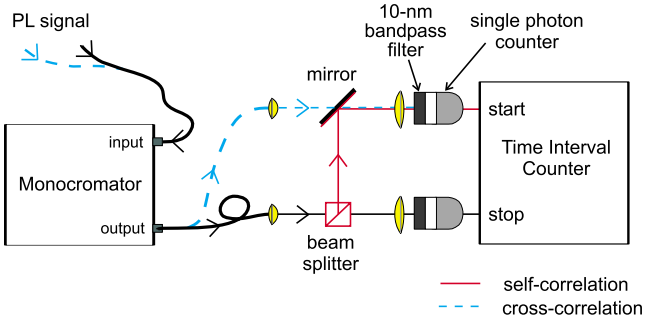

FIG. 28. (Color online) A realization Hanbury Brown–Twiss measurement with single-photon counters. For autocorrelation measurement, use a single-core fiber, beam splitter, and mirror (solid path). For cross correlation, use a double-core fiber bundle to carry the two input and output signals (dashed path).

counters, essentially the integrated area under each pulse was measured, which gives the numerator in the following equation:

$$\overline{g^{(2)}}(j) = \frac{\langle n_1(i)n_2(i+j)\rangle_i}{\langle n_1\rangle\langle n_2\rangle}, \tag{78}$$

where $n_1(i)$ and $n_2(i+j)$ are the photon numbers detected by the two-photon counters in pulses i and $i+j$, respectively. In the limit of low average count rates ($n < 0.01$ per pulse in our experiment), $\overline{g^{(2)}}(j)$ approximates time-averaged $g^{(2)}(\tau)$ over each pulse. For $j \neq 0$, coincidence counts are recorded from adjacent pulses which are uncorrelated and thus $\overline{g^{(2)}}(j) \equiv 1$ for $j \neq 0$. Assuming the same statistical properties of all pulses, the area of these peaks at $j \neq 0$ gives the denominator in Eq. (78).

The emission pulse of the LP ground state was first filtered by a monochromator with a resolution of $\Delta\lambda = 0.1$ nm, resulting in a pulse with a coherence time of $\Delta\tau_c = \sqrt{8\ln 2}\lambda^2/c\Delta\lambda \sim 4$ ps. Below threshold, the full width at half maximum (FWHM) temporal width of the pulse is about 350 ps, much longer than the coherence time of the pulse $\Delta\tau_c \sim 4$ ps. Since the measured $\overline{g^{(2)}}(0)$ is an integration of $g^{(2)}(0)$ over the whole pulse as given in Eq. (78) and $g^{(2)}(\tau) \approx 1$ during most of the pulse, $\overline{g^{(2)}}(0)$ is also close to 1 even though the system is expected to be in a thermal state. Poor time resolution is a common limitation in Hanbury Brown–Twiss-type measurements.

Fortunately, at threshold, the pulse width shortens to ~8 ps and becomes comparable to $\Delta\tau_c$. Hence $\overline{g^{(2)}}(0)$ becomes a good approximation of $g^{(2)}(0)$. Here bunching of the emitted photons was observed, with a maximum $\overline{g^{(2)}}(0)$ of 1.77 at $P/P_{\text{th}} \sim 1.1$ (Fig. 29). This bunching effect, which is obscured by the time-integration effect below threshold, is the signature of bosonic final-state stimulation. Far above threshold, the pulse width only decreases further, therefore $\overline{g^{(2)}}(0)$ remains a good estimate for $g^{(2)}(0)$. However, the $\overline{g^{(2)}}(0)$ measured in this region decreases, which demonstrates the formation of second-order coherence in the system or, in other words, the polariton gas starts to acquire macroscopic coherence.

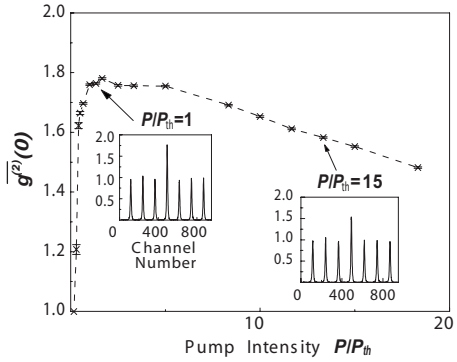

FIG. 29. The second-order coherence function $\overline{g^{(2)}}(0)$ vs pump intensity P/P_{th}. From Deng *et al.*, 2002.

$\overline{g^{(2)}}(0)$ decreases only very slowly with increasing density above threshold, indicating a relatively small condensate fraction which builds up only gradually with increasing total density of LPs. This is typical of two-dimensional systems with relatively strong interactions, where there is large quantum depletion of the condensate. Theoretical and numerical studies have predicted the same qualitative behavior (Sarchi *et al.*, 2008; Schwendimann and Quattropani, 2008).

Recently a similar measurement was performed with a CdTe-based microcavity (Kasprzak *et al.*, 2008). In this experiment, emission from the LP ground state, not filtered in energy, has a coherence time of ~2 ps below and around threshold. $\overline{g^{(2)}}(0)$ close to 1 was observed for excitation densities from below the threshold P_{th} to $\sim 2P_{\text{th}}$. At higher excitation densities, $\overline{g^{(2)}}(0)$ increases significantly to >2 at $\sim 10P_{\text{th}}$.

Kasprzak *et al.* (2008) also measured $g^{(2)}(0)$ under quasi-continuous-wave excitation (with an excitation pulse duration of ~1 μs). In this case, the time resolution is limited by that of the photon counters, which is 120 ps. A small bunching with $g_m^{(2)}(0) \sim 1.03$ was measured below and around P_{th}. If correcting for the coherence time and photon counter resolution, it corresponds to an actual $g^{(2)}(0) \approx 2.8 \pm 1$. No bunching above the noise level was observed at $1.5P_{\text{th}}$, which indicates a decrease in $g^{(2)}(0)$. $g_m^{(2)}(0) > 1$ is again measured above $2.3P_{\text{th}}$, consistent with the pulsed measurement.

2. Kinetic models of the $g^{(2)}$

Using a stochastic Boltzmann kinetic equation and master equation, we study the probability to find n LPs in the ground state (Doan, Cao, *et al.*, 2008). The quantum-statistical correlation function $g^{(2)}$ is given by the correlations of the condensate operators (Glauber, 1963)

$$g^{(2)}(\tau) = \frac{\langle b_0^\dagger(t)b_0^\dagger(t+\tau)b_0(t+\tau)b_0(t)\rangle}{\langle b_0^\dagger(t+\tau)b_0(t+\tau)\rangle\langle b_0^\dagger(t)b_0(t)\rangle}. \tag{79}$$

Note that the field operators are in the normal form with all creation operators to the right. In the number representation for zero delay

$$g^{(2)}(0) = \frac{\langle n_0(n_0-1)\rangle}{\langle n_0\rangle^2}. \tag{80}$$

The mean condensate density $\langle n_0(t)\rangle = \langle b_0^\dagger(t) b_0(t)\rangle$ is determined by a Boltzmann equation which governs the scattering kinetics in and out of the ground state,

$$\frac{\partial\langle n_0\rangle}{\partial t} = \langle R_{\rm in}(t)[1+n_0(t)]\rangle - \langle R_{\rm out}(t) n_0(t)\rangle. \tag{81}$$

The rate in is given by the scattering processes from the excited states to the ground state by LP-LP and LP-phonon scatterings,

$$R_{\rm in} = \sum_{k,k'} w^{\text{LP-LP}}_{0,k;k',k-k'}(1+n_k) n_{k'} n_{k-k'} + \sum_{q,\sigma=\pm1} w^{\text{LP-}ph}_{0,q\sigma} n_q N_{q,-\sigma}. \tag{82}$$

The rate out is given by

$$R_{\rm out} = \frac{1}{\tau_0} + \sum_{k,k'} w^{\text{LP-LP}}_{0,k;k',k-k'} n_k (1+n_{k'})(1+n_{k-k'}) + \sum_{q,\sigma=\pm1} w^{\text{LP-}ph}_{0,q\sigma}(1+n_q) N_{q,-\sigma}. \tag{83}$$

Formally one has exchange rates due to the scattering process $\vec{k},0\rightarrow 0,\vec{k}$. These exchange rates do not give rise to changes of the populations and thus should not be included in the kinetics. The mean rate equation can then be written as

$$\frac{\partial\langle n_0\rangle}{\partial t} = \langle R_{\rm in}(t)\rangle\langle[1+n_0(t)]\rangle - \langle R_{\rm out}(t)\rangle\langle n_0(t)\rangle. \tag{84}$$

To calculate the second moments of the condensate, we need a stochastic extension of the condensate's kinetic equation. There are at least four possible formulations of such an extension:

- One can supplement the Boltzmann equation for n_0 by Langevin fluctuations with shot-noise character (Haug and Haken, 1967; Lax, 1967; Haug, 1969). The second moments of density are then determined by the second moments of these shot-noise fluctuations. As it is known from laser theory, Langevin equations can be solved approximately by linearization below and above threshold, but there is no simple way to find solutions in the whole density regime.
- This is different for the associate Fokker-Planck equation in which the probability for a certain density value is calculated. In stationary equilibrium, one gets an analytic solution in terms of an exponential of a generalized Ginzburg-Landau potential [see Risken (1984)]. The change of the potential from below threshold with a minimum at $n=0$ to a potential with a sharp minimum at $n\neq 0$ above threshold describes the probabilities for all densities. In both approaches, the Langevin and Fokker-Planck methods, the density is considered to be a continuous variable which is valid if $n \gg 1$. Because in a BEC the condensate density varies from small values of $n \ll 1$ below threshold to large values above $n \gg 1$ this approximation is not well justified below and at threshold where $n = O(1)$.
- The third possible stochastic extension of the ground-state kinetics is the master equation of the probability to find n particles in this state. The master equation takes into account the discrete nature of the number of condensed particles (Carmichael, 2003) but disregards the phase of the condensed state. This semiclassical approach has been studied by Laussy *et al.* (2004). They calculated $g^{(2)}(0)$ for CdTe microcavities from numerical solutions of the time-dependent master equation and considered LP-phonon and LP-electron scatterings. Here we use a well-converging continued fraction method for the solution of the stationary master equation and calculate the results for GaAs microcavities, including both LP-phonon and LP-LP scattering. The results are compared with experimental observations (Deng *et al.*, 2002).
- Still another possibility is to treat the kinetics of the second-order function $\langle b_0^\dagger(t) b_0^\dagger(t) b_0(t) b_0(t)\rangle$ in addition to the kinetics (Sarchi *et al.*, 2008; Schwendimann and Quattropani, 2008).

3. Master equation with gain saturation

We now formulate the master equation for the probability $W_n(t)$ to find n particles in the condensate at time t, dropping the index 0 to ease the notation. With the gain saturation rate $G_n = R_n^{\rm in}(n+1)$ and decay rate $D_n = R_n^{\rm out}$, we have the master equation

$$\frac{dW_n}{dt} = -(G_n + D_n) W_n + D_{n+1} W_{n+1} + G_{n-1} W_{n-1} = \sum_{m=n-1}^{m=n+1} M_{n,m} W_m. \tag{85}$$

$M_{n,m}$ is a tridiagonal matrix (Risken, 1984). Its elements are

$$M_{n,n} = -(G_n - D_n), \quad M_{n,n+1} = D_{n+1}, \quad M_{n,n-1} = G_{n-1}. \tag{86}$$

The rate equation does not provide the full information for constructing the corresponding master equation because the transition rates are only known for the mean $\langle n\rangle$ but not for n [see, e.g., Carmichael (2003)]. Systematically, one would have to determine the populations of the excited states as a function of the pump rate and the number of LPs in the ground state. It can be done analytically for a homogeneously broaden three-level laser but only numerically in our case from the solution of the Boltzmann equation. Simple procedures to include this correction (Laussy *et al.*, 2004) are to expand the distributions of the excited states linearly around $\langle n\rangle$ as $n_k(n) = \langle n_k\rangle + (\partial n_k/\partial n)(n - \langle n\rangle)$ and estimate

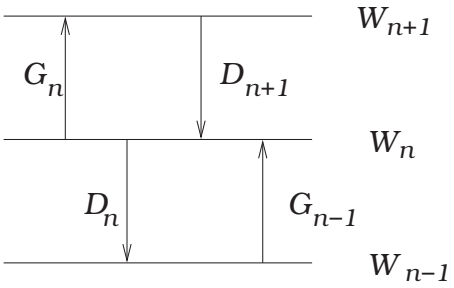

FIG. 30. Level diagram for master equation.

$$\left.\frac{\partial\langle n_k\rangle(n)}{\partial n}\right|_{\langle n\rangle} = \frac{\langle n_k\rangle}{\langle n\rangle - N}, \tag{87}$$

where N is the total number of polaritons. This yields

$$\langle n_k\rangle(n) = \langle n_k\rangle\left(1 + \frac{n-\langle n\rangle}{\langle n\rangle - N}\right). \tag{88}$$

These correction terms of the scattering rates in the master equation vanish approximately if one calculates with the modified master equation and with $\langle n\rangle = \Sigma_n n W_n$. We use these corrections of the scattering rates in the linear approximation. Because $\langle n_k\rangle \ll 1$ for all excited states, stimulated scattering into these states is negligible and $1+\langle n_k\rangle \sim \langle n\rangle$. Thus the LP-phonon-scattering rate $R_{\text{in}}^{\text{LP-}ph}$ has a correction term $F(n)=(n-\langle n\rangle)/(\langle n\rangle - N)$, while the LP-LP scattering rate $R_{\text{in}}^{\text{LP-LP}}$ has a correction factor $2F(n)$. In the rate out, only the LP-LP scattering rate $R_{\text{out}}^{\text{LP-LP}}$ is corrected by a factor $F(n)$, while other rates remain unchanged.

4. Stationary solution

Under stationary pumping, if a stationary state is reached, the rates in and out of the ground state no longer change with time. The stationary solution is maintained if the rates between two successive states balance. From Fig. 30 we see that the following detailed balance relation holds:

$$D_n W_n = G_{n-1} W_{n-1}, \tag{89}$$

which yields the detailed balance solution

$$W_n = \frac{G_{n-1}}{D_n} W_{n-1} = \prod_{k=1}^{k=n} \frac{G_{k-1}}{D_k} W_0. \tag{90}$$

W_0 is obtained from the normalization $\Sigma_n W_n = 1$.

In general, the stationary solutions are obtained from

$$\sum_{m=n-1}^{m=n+1} M_{n,m} W_m = 0. \tag{91}$$

Following Risken (1984), we introduce the ratio $S_n = W_{n+1}/W_n$ and rewrite Eq. (91) as

$$M_{n,n} + M_{n,n+1} S_n + \frac{M_{n,n-1}}{S_{n-1}} = 0. \tag{92}$$

By changing $n \to n+1$, we obtain

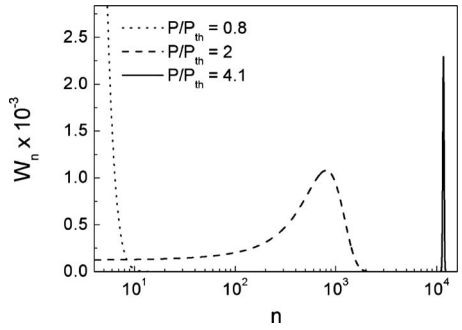

FIG. 31. Calculated distribution functions W_n for various normalized pump powers P/P_{th}. From Doan, Cao, *et al.*, 2008.

$$S_n = -\frac{M_{n+1,n}}{M_{n+1,n+1} + M_{n+1,n+2} S_{n+1}}. \tag{93}$$

Equation (93) is well suited for numerical iteration. By analytical iteration one obtains continued fractions for the ratio S_n and W_n is then given by

$$W_n = \prod_{k=0}^{k=n-1} S_k W_0. \tag{94}$$

The value of W_0 follows again from the normalization condition. One can start the iteration at a value $N \gg \langle n\rangle$ when $W_{N+1} = W_{N+2} = \cdots = 0$, so that $S_N = 0$. This iterative procedure can also be generalized for the solution of the time-dependent master equation (Risken, 1984) where detailed balance is no longer fulfilled.

5. Numerical solutions of the master equation

The stationary probability distributions obtained by iteration are shown in Fig. 31 for three pump powers. Below threshold, the distribution peaks at $n=0$ and decays monotonically. Slightly above threshold, the distribution peaks at a value $\langle n\rangle \gg 1$ but is still rather broad. Well above threshold for $P/P_{\text{th}}=4.1$, the distribution peaks sharply around a larger density value of about $\langle n\rangle \simeq 10^4$. We checked that the solutions obtained iteratively agree indeed with those obtained from the detailed balance condition.

Once all W_n are calculated including the normalization W_0, one obtains $g^{(2)}(0) = \langle n(n-1)\rangle/\langle n\rangle^2$. We see in Fig. 32 how the thermal limit with $g^{(2)}(0)=2$ is smoothly connected with $g^{(2)}(0)=1$. Surprisingly, the transition takes place not in the threshold region but around a pump power of $P \simeq 2P_{\text{th}}$. This delayed transition from the thermal to the coherent limit is due to the semiclassical approach which assumes an n-diagonal density matrix.

As discussed, the fast decay of the correlations above threshold is not observed in the experiments (Deng *et al.*, 2002). This can be understood qualitatively, taking into account that $g^{(2)}(\tau)$ varies as $g^{(2)}(\tau) = 2e^{(R_{\text{in}}-R_{\text{out}})\tau}$ as one can show, e.g., in a Langevin approach. An average over the delay times yields $\bar{g}_2(0) \propto g^{(2)}(0)/(R_{\text{out}}-R_{\text{in}})$. As the pump power decreases away from threshold R_{out}

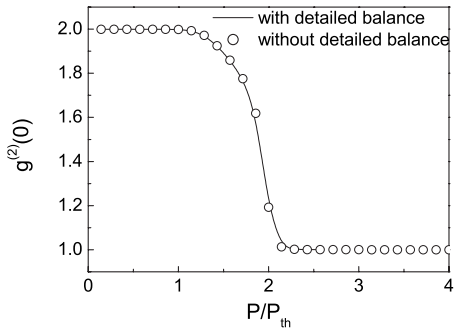

FIG. 32. Calculated second-order coherence function $g^{(2)}(0)$ vs normalized pump power P/P_{th}. The full line is obtained by iteration and the circles by the detailed balance relation. From Doan, Cao, *et al.*, 2008.

$-R_{\mathrm{in}}$ increases. Thus the averaged $\bar{g}_2(0)$ decreases rapidly below threshold, as seen in the experiment with the strongly fluctuating 2 ps GaAs microcavities. In a recent experiment with improved GaAs microcavities (Roumpos, Hoefling, *et al.*, 2009), the minimum of $g^{(2)}$ as a function of pump power seems to occur at threshold, and the range of correlations above the Poisson limit extends over a much wider pump range. Similar observations have been made in CdTe microcavities (Kasprzak *et al.*, 2008). Further many-body effects have to be found in order to account for the difference between these experimental findings and the theory.

6. Nonresonant two-polariton scattering (quantum depletion)

One way to improve the $g^{(2)}$ calculations is to include quantum depletion processes. Following the idea of Schwendimann and Quattropani (2008), one can consider a quadratic correction term in the form of a scattering of two condensate LPs to the excited states with the momenta q and $-q$. This process is nonresonant and only takes place when the linewidth is finite. The corresponding transition rate is

$$\sum_q w^{\mathrm{LP\text{-}LP}}_{0,0;q,-q}[n(n-1)(1+n_q)(1+n_{-q}) - (1+n)(2+n)n_q n_{-q}], \tag{95}$$

with $n \geqslant 1$. The energy-conserving delta function has to be replaced, e.g., by a Gaussian resonance

$$2\pi\delta(2e_0 - 2e_q) \Rightarrow \frac{2}{\gamma}e^{-4(e_0-e_q)^2/\gamma^2}. \tag{96}$$

This yields two-particle transition rates of the form

$$G^2_n = R^{\mathrm{in},(2)}(n+1)(n+2), \qquad R^{\mathrm{in},(2)} = \sum_q w^{\mathrm{LP\text{-}LP}}_{0,0;q,-q} n_q n_{-q} \tag{97}$$

and

$$D^2_n = R^{\mathrm{out},(2)} n(n-1), \tag{98}$$

$$R^{\mathrm{out},(2)} = \sum_q w^{\mathrm{LP\text{-}LP}}_{0,0;q,-q}(1+n_q)(1+n_{-q}).$$

The last finite decay rates are $D^2_1 = D^2_0 = 0$ and $D^2_2 = 2R^{\mathrm{out},(2)}$ because at least two LPs are needed in the ground state for a quadratic scattering process out of the ground state.

The two quadratic terms extend the three-diagonal master equation to a five-diagonal one,

$$\frac{dW_n}{dt} = -(G_n + D_n + G^{(2)}_n + D^{(2)}_n)W_n + D_{n+1}W_{n+1} + D^{(2)}_{n+2}W_{n+2} + G_{n-1}W_{n-1} + G^{(2)}_{n-2}W_{n-2} = \sum_{m=n-2}^{m=n+2} M_{n,m}W_m. \tag{99}$$

Solving this pentadiagonal master equation iteratively [for details see Doan, Thien Cao, *et al.* (2008)] one finds for realistic values of the collision broadening a rather small increase of $g^{(2)}$ above threshold. In contrast, Schwendimann and Quattropani (2008) found additional correlations above the coherent limit and a minimum of $g^{(2)}$ around threshold, as has been observed, under the assumption of a thermal exciton reservoir. If the kinetics of the excited states is included (Sarchi and Savona, 2008), the minimum in the threshold region is nearly eliminated but the extra correlations remain. The differences between the results of Doan, Thien Cao, *et al.* (2008) and Sarchi and Savona (2008) could be partly due to the fact that the quadratic corrections have been neglected in the Boltzmann equation.

In order to give an alternative explanation, Doan, Thien Cao, *et al.* (2008) considered a phenomenological kinetic saturation model. It is known that the 2D excitons ionize once their density is so high that the exciton wave functions start to overlap (Schmitt-Rink *et al.*, 1985). The critical saturation density due to phase-space filling has been evaluated from the reduction of the exciton oscillator strength to be $1/n_s = \frac{32}{7}\pi a^2_{2\mathrm{D}}$. This will also result in a reduction of the exciton density n to $n/[1+(n/n_s)^2]$. In order to incorporate the saturation effect kinetically in the master equation, we introduce phenomenologically a two-polariton ionization rate. Due to the overlap of the wave functions in a collision of two polaritons, the two polaritons are assumed to by ionized and thus lost for the condensate,

$$D^2_n = \frac{1}{\tau_0}n(n-1)\frac{r_s}{n_s}. \tag{100}$$

We have included a small numerical factor r_s in order to avoid an unphysically large ionization rate far below saturation. We used the lifetime τ_0 to set the scale for the ionization rate. Any direct backscattering from the ionization continuum to the condensate can be neglected.

In Fig. 33 the results are plotted for the saturation model. We see that with increasing interaction strength r_s the range where $g^{(2)} \geqslant 1$ extends to larger pumping

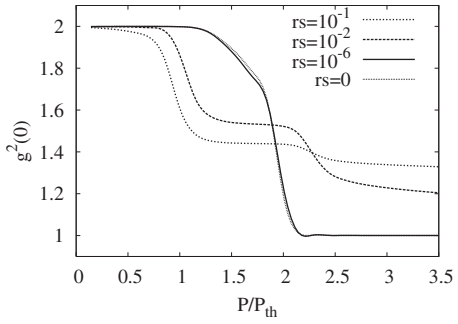

FIG. 33. Calculated second-order coherence function $g^{(2)}(0)$ vs normalized pump power P/P_{th} for the kinetic saturation model.

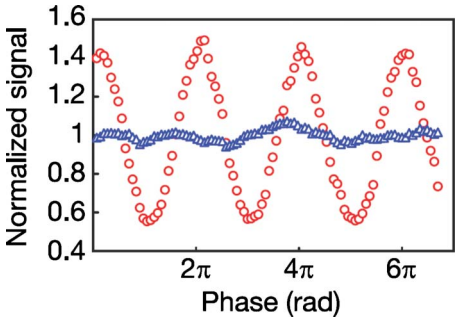

FIG. 34. (Color online) Interference fringes between two fragments ~6 μm apart, measured below (open triangles) and above (open circles) the nonlinear threshold, with contrasts of 5% and 46%, respectively. Horizontal axis is the relative phase. Adapted from Kasprzak *et al.*, 2006.

rates as has been observed in the experiment (Deng *et al.*, 2002). This simple model brings the results closer to those of the experiment.

B. First-order temporal coherence

The first-order temporal coherence is characterized by the energy linewidth of the LP emission. Interestingly, the linewidth above threshold does not decrease according to the Shallow-Townes formula but increases again (Porras and Tejedor, 2003) with increasing density of the LPs in the ground state. This observed effect can be calculated by the Langevin equations for the Bogoliubov model of weakly interacting bosons. The LP population in the ground state gives rise to a Kerr-effect-like behavior which in turn causes the linewidth increase (Tassone and Yamamoto, 2000).

C. First-order spatial coherence

First-order spatial coherence or the so-called off-diagonal long-range order (ODLRO) is studied by Penrose and Onsager (1956), Beliaev (1958), and Yang (1962).

1. Long-range spatial coherence in a condensate

The Bose field operator $\Psi(\boldsymbol{r})$ of an ideal gas is defined as

$$\Psi(\boldsymbol{r}) = \frac{1}{\sqrt{V}}\sum_i \hat{a}_i e^{i\boldsymbol{p}_i\boldsymbol{r}} = \frac{a_0 e^{i\boldsymbol{p}_0\boldsymbol{r}}}{\sqrt{V}} + \frac{1}{\sqrt{V}}\sum_{i\neq 0}\hat{a}_i e^{i\boldsymbol{p}_i\boldsymbol{r}}$$
$$= \Psi_0(\boldsymbol{r}) + \Psi_T(\boldsymbol{r}), \tag{101}$$

where $\boldsymbol{r}$ is the coordinate vector and $\boldsymbol{p}_i$ is the momentum vector of the state i. $\Psi_T(\boldsymbol{r})$ consists of terms of the excited states. In the thermodynamic limit of $V\to\infty$, $\Psi_T(\boldsymbol{r})$ vanishes for $r>0$. $\Psi_0(\boldsymbol{r})$ is the ground-state term. In a condensed phase, a_0 can be approximated by a c-number amplitude and $\Psi_0(\boldsymbol{r})$ has a finite and constant amplitude given by the square root of the condensate fraction. Thus $\Psi(\boldsymbol{r})$ also serves as the order parameter of BEC.

The off-diagonal element of the first reduced density matrix of $\Psi(\boldsymbol{r})$ is

$$\rho_1(\boldsymbol{r},\boldsymbol{r}') = \langle\Psi^\dagger(\boldsymbol{r}')\Psi(\boldsymbol{r})\rangle$$
$$= \langle\Psi_0^\dagger(\boldsymbol{r}')\Psi_0(\boldsymbol{r})\rangle + \langle\Psi_T^\dagger(\boldsymbol{r}')\Psi_T(\boldsymbol{r})\rangle$$
$$= \frac{N_0}{V}e^{i\boldsymbol{p}_0(\boldsymbol{r}-\boldsymbol{r}')} + \frac{1}{V}\sum_{i\neq 0}\langle\hat{a}_i^+\hat{a}_i\rangle e^{i\boldsymbol{p}_i(\boldsymbol{r}-\boldsymbol{r}')}. \tag{102}$$

$\rho_1(\boldsymbol{r},\boldsymbol{r}')$ describes the first-order coherence between the fields at positions $\boldsymbol{r}$ and $\boldsymbol{r}'$. We again can separate it into terms of the excited states and a term from the ground state. When $|\boldsymbol{r}-\boldsymbol{r}'|\to\infty$, the phase $\boldsymbol{p}_i(\boldsymbol{r}-\boldsymbol{r}')$ of the excited-state terms becomes random, and the summation of these terms vanishes when $V\to\infty$. The ground-state term, however, has a finite and constant amplitude of $0<n_0\leqslant n$ in the BEC phase regardless of the separation $|\boldsymbol{r}-\boldsymbol{r}'|$. Hence $|\rho_1(\boldsymbol{r},\boldsymbol{r}')|=n_0=|\Psi_0|^2$ is finite and uniform even over macroscopic distances. In other words, ρ_1 has an ODLRO. This is an essential character of BEC.

In two dimensions, long-wavelength thermal fluctuations of the phase destroy a genuine long-range order in the thermodynamic limit (Mermin and Wagner, 1966; Hohenberg, 1967). But quasi-BEC is established when coherence is established throughout the system size in an interacting Bose gas (Lauwers *et al.*, 2003), such as manifested in extended spatial coherence.

2. Spatial coherence among bottleneck LPs

Spatial coherence of LPs was first studied by Richard *et al.* (2005). In this experiment, a CdTe-based microcavity was used. Above a threshold excitation density P_{th}, LP lasing was observed in bottleneck states with in-plane wave number $k_\parallel=k_{\mathrm{bot}}$ and energy $E(k_{\mathrm{bot}})$. The 2D Fourier plane image of the LPs was uniform at $P<P_{\mathrm{th}}$. At $P>P_{\mathrm{th}}$, speckles appeared in the images, which was related to an increase in spatial coherence among the LP emitters. At the same time, the emission linewidth at $E(k_{\mathrm{bot}})$ was broadened in $k_\parallel$, and interference in $k_\parallel$ was observed by a Billet interferometer setup. It again indicated increased spatial coherence (Fig. 34).

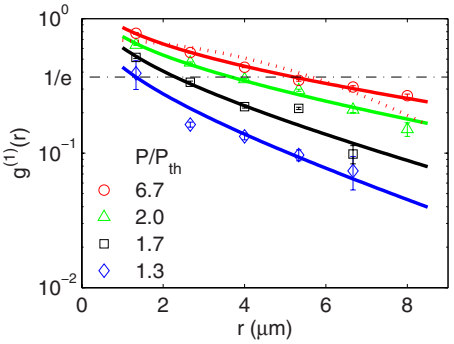

FIG. 35. (Color online) $g^{(1)}(r)$ vs r for different pump rates P/P_{th} as given in the legend. The symbols are measured $g^{(1)}(r)$. The solid lines are fits by the modified Bessel function of the first kind, corresponding to the 2D Fourier transform of the momentum distribution of $\propto k_B T/[E(k)-\mu]$. The dashed line at $P/P_{\mathrm{th}}=7$ is fit by the 2D Fourier transform of a Maxwell-Boltzmann distribution. The dash-dotted line marks where $g^{(1)}(r)=1/e$ (Deng *et al.*, 2007).

3. Spatial coherence between fragments of a condensate

Later Kasprzak *et al.* (2006) measured directly the spatial coherence of a fragmented condensate. LPs condensed into the $k_{\parallel}\sim 0$ state but at multiple localized small areas of ~ 4 μm in diameter within the 20–30 μm excitation spot. PL from different localized condensates was brought into interference after a Michelson interferometer. The fringe visibility gives the first-order coherence function $g^{(1)}(r)$,

$$g^{(1)}(\boldsymbol{r}) = \frac{\langle \hat{E}^{(-)}(\boldsymbol{r}_0)\hat{E}^{(+)}(\boldsymbol{r}_0+\boldsymbol{r})\rangle}{\sqrt{\langle \hat{E}^{(-)}(\boldsymbol{r}_0)\hat{E}^{(+)}(\boldsymbol{r}_0)\rangle\langle \hat{E}^{(-)}(\boldsymbol{r}_0+\boldsymbol{r})\hat{E}^{(+)}(\boldsymbol{r}_0+\boldsymbol{r})\rangle}} = \frac{\rho_1(\boldsymbol{r}_0,\boldsymbol{r}_0+\boldsymbol{r})}{\sqrt{\rho_1(\boldsymbol{r}_0,\boldsymbol{r}_0)\rho_1(\boldsymbol{r}_0+\boldsymbol{r},\boldsymbol{r}_0+\boldsymbol{r})}}. \tag{103}$$

Interestingly, between two fragments of condensate $r \approx 6$ μm apart, $g^{(1)}(r)$ increased sharply across the threshold from 5% to 8% below threshold to a maximum value of 46% at $\sim 2P_{\mathrm{th}}$ (Fig. 34). This verifies that although local disorder caused spatial fragmentation of the LP gas, different fragments are phase locked with each other.

4. Spatial coherence of a single-spatial mode condensate

A more systematic study of spatial coherence was carried out by Deng *et al.* (2007). A GaAs-based microcavity was used, where the LP condensate forms a single-spatial mode. A double slit was placed in the near-field image of the LPs, which passes PL from different spatial regions of the condensate. Far-field interference between light through the two slits was then recorded, which consists of a cosine oscillation imposed on a sinc function envelope due to the finite slit width. The amplitude of the cosine oscillation corresponds to $g^{(1)}(r)$, r given by the slit separation.

$g^{(1)}(r)$ increases sharply across the threshold and saturates at $P>3P_{\mathrm{th}}$. The maximum $g^{(1)}(r)$ of ~ 0.8 was measured for $r=1.3$ μm, which is approximately the intrinsic coherence length of a single LP. At $r=8$ μm, which is the size of the excitation spot, $g^{(1)}(r)$ remains above $e^{-\pi}$. From $r=1.3$ to 8 μm, decay of $g^{(1)}(r)$ is well modeled by the Fourier transform of the momentum distribution of LPs. The $e^{-\pi}$ decay length of $g^{(1)}(r)$ was about eight times the thermal de Broglie wavelength above threshold (Fig. 35). This demonstrates that coherence extends to a much longer range than both the average LP-LP spacing and LP's intrinsic coherence length. Finite coherence is maintained throughout the condensate. At the same time, there is a significant thermal excitation from the condensate.

5. Theory and simulations

An early attempt to calculate the first-order spatial correlation function is due to Sarchi and Savona (2007a, 2007b, 2008). With the condensation kinetics they obtained relatively large condensate densities which resulted in a strong off-diagonal long-range order. They incorporated many-body effects using the Popov approximation (Shi and Griffin, 1998) in order to calculate the depletion of the condensate. Here we calculate $g^{(1)}$ using $n_k(t)$ and $n_0(t)$ obtained through the Boltzmann equations.

We write the first-order spatial coherence function in terms of the LP field operator $\psi(\vec{r})$ as

$$g^{(1)}(\vec{r}_1,\vec{r}_2) = \frac{\langle \psi^{\dagger}(\vec{r}_1)\psi(\vec{r}_2)\rangle}{\langle \psi^{\dagger}(\vec{r}_1)\rangle\langle \psi(\vec{r}_2)\rangle}. \tag{104}$$

Inserting a plane-wave expansion

$$\psi(\vec{r}) = \frac{1}{\sqrt{S}}\left(b_0 + \sum_{\vec{k}} b_k e^{i\vec{k}\cdot\vec{r}}\right), \tag{105}$$

we find in the free-particle approximation

$$g^{(1)}(\vec{r}_1,\vec{r}_2) = \frac{n_0 + \sum_{\vec{k}} n_k e^{i\vec{k}\cdot(\vec{r}_1-\vec{r}_2)}}{n_0}. \tag{106}$$

With the calculated populations we can now evaluate the pump power dependence of $g^{(1)}(r=|\vec{r}_1-\vec{r}_2|)$ for various values of the distance r. We use a positive detuning of 4 meV and a system size of 100 μm in cross section. The pump power P is normalized to the threshold value P_{th}. Figure 36 shows how the range of the spatial coherence increases above threshold. These results are in excellent agreement with the double-slit experiment by Deng *et al.* (2007) as shown in Fig. 37.

As a next test we plot the distance dependence of $g^{(1)}(r)$ in Fig. 38 for various values of the pump power. We see a more or less exponential decay of the coherence function. The coherence length increases with pump power, i.e., with the degeneracy of the condensed LPs. The corresponding measurements shown in Fig. 35 are again in quantitative agreement with the calculated values of the coherence function.

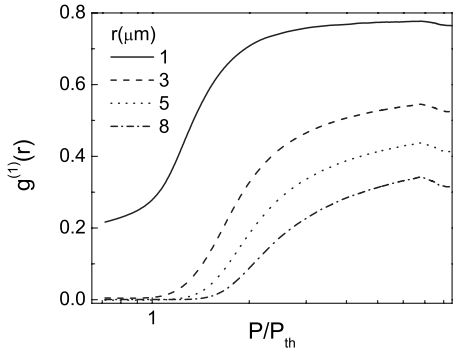

FIG. 36. Calculated first-order coherence function $g^{(1)}(r)$ vs normalized pump power P/P_{th} for various distances r. From Doan, Cao, *et al.*, 2008.

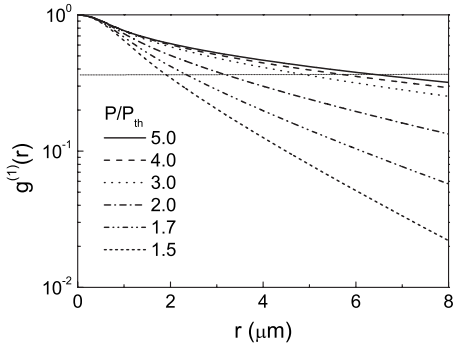

FIG. 38. Calculated first-order coherence function $g^{(1)}(r)$ vs distances r for various normalized pump powers P/P_{th}. From Doan, Cao, *et al.*, 2008.

D. Spatial distributions

The presence of a condensate with a long coherence length changes the spatial distribution of LPs in characteristic ways. If there is a harmonic potential, the spatial distribution features a Thomas-Fermi profile, and the width of the distribution scales inversely proportional to the width in the momentum space. In the absence of in-plane confinement potential, the spatial properties are governed by two factors: the spatial distribution due to the profile of the excitation laser and the finite extension of the macroscopic coherence as a 2D system.

1. Condensate size and critical density

If the excitation laser has a nonuniform profile, such as a Gaussian with a FWHM spot size of ω_p, the center of the spot reaches the degeneracy threshold first and forms a quasicondensate with a spatial extension $\omega_c \ll \omega_p$. With increasing excitation density, ω_c also increases. If the critical density is constant independent of the system size, ω_c will expand as

$$\omega_c = \omega_p \sqrt{1 - \log_2\left(1 + \frac{P_{\mathrm{th}}}{P}\right)}. \tag{107}$$

In two dimensions, however, a higher critical density of condensation $n_c(\omega_c)$ is required to maintain coherence over a larger area (Ketterle and van Druten, 1996). This effect was first observed by Deng *et al.* (2003). A planar microcavity was used without in-plane confinement potential. The excitation laser has a Gaussian profile with a FWHM spot size $\omega_p \approx 15\ \mu$m. While the LP emission follows the same profile below threshold, the emission spot size ω_{PL} shrank steeply when the center of the spot reached the critical density locally. At $P > P_{\mathrm{th}}$, the increase of ω_{PL} is much slower than predicted by Eq. (107).

Taking into account the size dependence of the critical density, Eq. (107) is modified as (Deng *et al.*, 2007)

$$\omega(P/P_{\mathrm{th}}) = \omega_p \sqrt{1 - \log_2\left(1 + \frac{1}{P/P_{\mathrm{th}}} \frac{n_c[\omega(P/P_{\mathrm{th}})]}{n_c(\omega_c)}\right)}. \tag{108}$$

Here $\omega_c \doteq \omega(P/P_{\mathrm{th}}=1)$ is the FWHM of the condensate when it first appears and corresponds to the smallest measured size. As a simplified model, consider n_c for a 2D boson gas confined in a finite size $L=2\omega$ (Ketterle and van Druten, 1996): $n_c(\omega) = (2/\Lambda_T^2)\ln(2\omega/\Lambda_T)$. One obtains

$$\omega(P/P_{\mathrm{th}}) = \omega_p \sqrt{1 - \log_2\left(1 + \frac{P_{\mathrm{th}}}{P} \frac{\ln(2\omega/\Lambda_T)}{\ln(2\omega_c/\Lambda_T)}\right)}. \tag{109}$$

Here Λ_T is the LP thermal de Broglie wavelength. The measured increase of the LP spot size was well described by Eq. (109), as shown in Fig. 39 (Deng *et al.*, 2007).

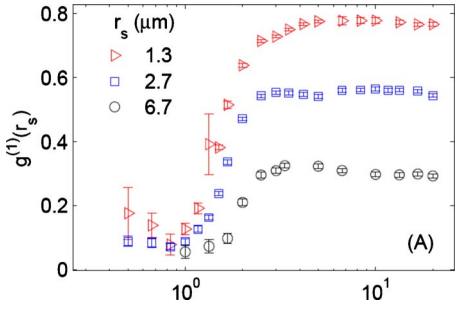

FIG. 37. (Color online) Measured first-order coherence function $g^{(1)}(r)$ vs normalized pump power P/P_{th} for various distances r. From Deng *et al.*, 2007.

2. Comparison to a photon laser

In the case of a photon laser (Deng *et al.*, 2003), a reduction in the spot size was also observed at the lasing threshold. In sharp contrast to the LP condensation, the increase of the spot size above threshold is much faster and was explained well by the classical local oscillator model of Eq. (107) [Fig. 39(c)]. This confirms that in a conventional photon laser gain is determined by local density of the electron-hole pairs with a threshold density independent of the system size.

Moreover, there are multiple transverse modes in the spatial profile above threshold [Fig. 39(b)], as is typical in large-area vertical cavity surface emitting lasers. Coherence in this case is present only in the photon field

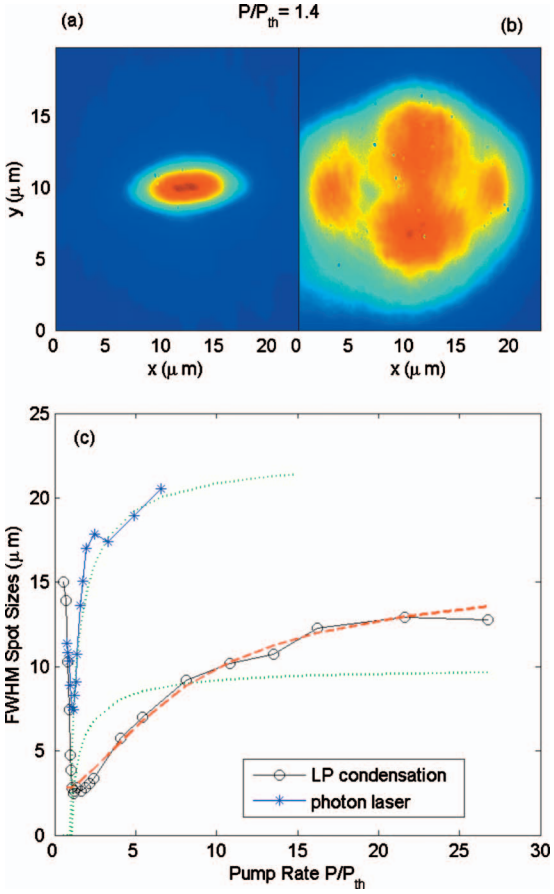

FIG. 39. (Color) Spatial distributions and spot sizes of a polariton laser vs a photon laser. (a) and (b) Spatial profiles of LPs and lasing cavity mode at 1.4 times the threshold pump powers, respectively. (c) Comparison of the expansion of the spot size vs pump rate for the LP condensate (circles) and the photon laser (stars). The red dashed line is fit by Eq. (108), with ω_p=16.5 μm, and ω_c=2.8 μm. The green dotted lines are fit by Eq. (107) assuming a pump spot size of ω_p=9 μm for the LP condensate and ω_p=23 μm for the photon laser. From Deng *et al.*, 2003.

but not in the electronic media. In the case of polariton condensation, however, a uniform Gaussian profile is maintained up to very high pump rates without obvious multiple transverse modes.

VIII. POLARITON SUPERFLUIDITY

The occurrence of BEC was originally predicted for an ideal gas of noninteracting bosonic particles (Einstein, 1925). However, particle-particle interaction and resulting peculiar excitation spectra are keys for understanding BEC and superfluidity physics (Tilley and Tilley, 1990; Pitaevskii and Stringari, 2003). A quantum field-theoretical formulation for a weakly interacting Bose condensed system was first developed by Bogoliubov, which predicted the phononlike linear excitation spectrum at low-momentum regime (Bogoliubov, 1947). The experimental verification of the Bogoliubov theory on a quantitative level was first performed for atomic BEC using two-photon Bragg scattering technique (Stamper-Kurn *et al.*, 1999). The particle-particle interaction and the Bogoliubov excitation spectrum have been studied theoretically for exciton polaritons (Shelykh *et al.*, 2005; Sarchi and Savona, 2008). Due to a short polariton lifetime, it is expected that the mode becomes diffusive and the dispersion is flat in a small momentum regime (Szymanska *et al.*, 2006; Wouters and Carusotto, 2007). In this section, we describe the observation of interaction effects on the condensate mean-field energy and the excitation spectra, which are in quantitative agreement with the Bogoliubov theory. The slope of the linear dispersion at the small momentum regime corresponds to a superfluid critical velocity according to Landau's criterion (Landau and Lifshitz, 1987). It is eight orders of magnitude faster than that for atomic BEC (Stamper-Kurn *et al.*, 1999). More direct evidence of polariton superfluidity came from recent observations of a quantized vortex pinned to a potential defect (Lagoudakis *et al.*, 2008) and a vortex-antivortex bound pair in a finite-size polariton BEC (Roumpos, Hoefling, *et al.*, 2009). Different from superfluidity arising from LP-LP interactions in a condensate, a superfluid LP was also created by coherent parametric pumping (Amo *et al.*, 2009).

A. Gross-Pitaevskii equation

The Hamiltonian of the exciton-polariton condensate expressed in terms of the LP field operator ψ is

$$\hat{H} = \int \left(\frac{\hbar^2}{2m} \nabla \hat{\psi}^+ \nabla \hat{\psi} \right) dr + \frac{1}{2} \int \hat{\psi}^+ \hat{\psi}'^+ V(r' - r) \hat{\psi} \hat{\psi}' dr' dr, \tag{110}$$

where $V(r)$ is the two-body interaction potential. The Heisenberg equation of motion of $\hat{\psi}$ is

$$i\hbar \frac{\partial}{\partial t} \hat{\psi}(r,t) = [\hat{\psi}(r,t), \hat{H}] = \left[-\frac{\hbar^2 \nabla^2}{2m} + \int \hat{\psi}^+(r',t) \times V(r' - r) \hat{\psi}(r',t) dr' \right] \hat{\psi}(r,t). \tag{111}$$

If the field operator is written in the form

$$\hat{\psi}(r) = \frac{1}{\sqrt{V}} \sum_p \hat{a}_p e^{ip \cdot r/\hbar}, \tag{112}$$

where V is a quantization volume and $\hat{a}_p$ is the annihilation operator for the single-particle state with a momentum p, Eq. (110) can be rewritten as

$$\hat{H} = \sum_p \frac{p^2}{2m}\hat{a}_p^+\hat{a}_p + \frac{1}{2V}\sum_{p_1}\sum_{p_2}\sum_q V_q \hat{a}_{p_1+q}^+\hat{a}_{p_2-q}^+\hat{a}_{p_1}\hat{a}_{p_2}, \tag{113}$$

where $V_q = \int V(r)\exp[-iq\cdot r/\hbar]dr$ is the Fourier transform of $V(r)$.

As far as the macroscopic properties of the condensate system are concerned, only small momenta are involved so that we are allowed to consider the $q=0$ value of V_q,

$$V_0 = g = \int V(r)dr, \tag{114}$$

and to rewrite the Hamiltonian in the form

$$\hat{H} = \sum_p \frac{p^2}{2m}\hat{a}_p^+\hat{a}_p + \frac{g}{2V}\sum_{p_1}\sum_{p_2}\sum_q \hat{a}_{p_1+q}^+\hat{a}_{p_2-q}^+\hat{a}_{p_1}\hat{a}_{p_2}. \tag{115}$$

According to the Bogoliubov prescription, we replace the operator $\hat{a}_0$ for the condensate with a c number,

$$\hat{a}_0 \equiv \alpha, \tag{116}$$

in Eq. (115). The corresponding c-number field amplitude (order parameter) $\psi_0(r,t)$ varies slowly over distances comparable to the range of the interparticle force, thus we substitute r' for r in Eq. (111) and obtain the Gross-Pitaevskii equation,

$$i\hbar\frac{\partial}{\partial t}\psi_0(r,t) = \left(-\frac{\hbar^2\nabla^2}{2m} + g|\psi_0(r,t)|^2\right)\psi_0(r,t). \tag{117}$$

B. Bogoliubov excitation spectrum

In a dilute and low-temperature limit, the occupation number for excited states with $p\neq 0$ is finite but small. In this first-order approximation, we neglect all terms in Eq. (115) containing $\hat{a}_p$ and $\hat{a}_p^+$ with $p\neq 0$. Then the ground-state energy is

$$E_0 = \frac{g}{2V}N^2. \tag{118}$$

The corresponding chemical potential or mean-field energy shift is given by

$$U(n) \equiv \frac{\partial E_0}{\partial N} = gn, \tag{119}$$

where $n=N/V$ is the particle density.

In order to obtain the excitation spectrum and study the quantum fluctuation, however, this level of approximation is insufficient. We have to work with higher accuracy using the normalization relation

$$\hat{a}_0^+\hat{a}_0 + \sum_{p\neq 0}\hat{a}_p^+\hat{a}_p = |\alpha|^2 + \sum_{p\neq 0}\hat{a}_p^+\hat{a}_p = N. \tag{120}$$

Substituting Eq. (120) into (115), we obtain the new Hamiltonian

$$\hat{H} = \frac{g}{2V}N^2 + \sum_{p\neq 0}\frac{p^2}{2m}\hat{a}_p^+\hat{a}_p + \frac{1}{2}gn\sum_{p\neq 0}(2\hat{a}_p^+\hat{a}_p + \hat{a}_p^+\hat{a}_{-p}^+ + \hat{a}_p\hat{a}_{-p}). \tag{121}$$

The above Hamiltonian can be diagonalized by the linear transformation (Bogoliubov, 1947)

$$\hat{a}_p = u_p\hat{b}_p + v_{-p}^*\hat{b}_{-p}^+, \quad \hat{a}_p^+ = u_p^*\hat{b}_p^+ + v_{-p}\hat{b}_{-p}. \tag{122}$$

If the two coefficients u_p and v_{-p} satisfy

$$|u_p|^2 + |v_{-p}|^2 = 1, \tag{123}$$

a new set of operators $\hat{b}_p$ and $\hat{b}_p^+$ satisfies the bosonic commutation relation $[\hat{b}_p, \hat{b}_{p'}^+] = \delta_{pp'}$. In order to make the non-number conserving terms $\hat{b}_p^+\hat{b}_{-p}^+$ and $\hat{b}_p\hat{b}_{-p}$ in Eq. (121) vanish, the coefficients u_p and v_{-p} must satisfy

$$\frac{U(n)}{2}(|u_p|^2 + |v_{-p}|^2) + \left(\frac{p^2}{2m} + U(n)\right)u_p v_{-p} = 0. \tag{124}$$

From Eqs. (123) and (124), we can solve u_p and v_{-p} as follows:

$$u_p = \sqrt{\frac{p^2/2m + U(n)}{\varepsilon(p)} + \frac{1}{2}}, \tag{125}$$

$$v_{-p} = -\sqrt{\frac{p^2/2m + U(n)}{\varepsilon(p)} - \frac{1}{2}}, \tag{126}$$

where

$$\varepsilon(p) = \sqrt{\frac{U(n)}{m}p^2 + \left(\frac{p^2}{2m}\right)^2}. \tag{127}$$

With this linear transformation, the Hamiltonian (121) is reduced to the diagonal form

$$\hat{H} = E_0 + \sum_{p\neq 0}\varepsilon(p)\hat{b}_p^+\hat{b}_p. \tag{128}$$

$\varepsilon(p)$ is the well-known Bogoliubov dispersion law for the elementary excitations from the condensate system.

C. Blueshift of the condensate mean-field energy

The $k=0$ LP mean-field energy is blueshifted with increasing number of LPs as shown in Fig. 40. This is a direct manifestation of the repulsive interaction among LPs. The $k=0$ LP energy shift $U(n)$ is calculated by Eq. (39). If we assume a constant size of the condensate, the theoretical energy shift is shown by the light blue line in Fig. 40. We can numerically solve the Gross-Pitaevskii (GP) equation [Eq. (117)] to incorporate the condensate expansion due to repulsive interaction. The results are shown by red dots in Fig. 40. These two theoretical predictions are compared to the experimental results (blue diamonds). Note that the above mentioned nonlinear model based on weakly interacting bosons (Schmitt-Rink *et al.*, 1985; Ciuti *et al.*, 1998; Rochat *et al.*, 2000) can reproduce the experimental data only in low LP

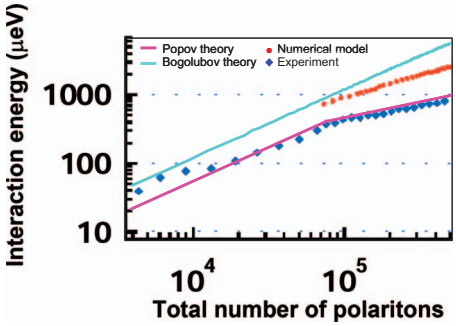

FIG. 40. (Color) The measured mean-field energy shift vs total number of polaritons (dark blue diamond). The analytical (blue solid line) and numerical (red dot) results based on Bogoliubov approximation (Utsunomiya *et al.*, 2008). The analytical result based on Popov approximation (pink solid line) is provided by Savona *et al.* (private communication).

density regimes. Recently the Popov approximation is applied to the LP system and quantitative agreement with the experimental data on $U(n)$ is obtained as shown by the pink solid line (Sarchi and Savona, 2008). We use the experimental values (not theoretical values) for $U(n)$ as the interaction energy in subsequent discussions for the universal feature of the Bogoliubov excitations.

D. Energy vs momentum dispersion relation

Using a microcavity with a very long cavity-photon lifetime of 80 ps, Roumpos, Hoefling, *et al.* (2009) measured again the excited-state energy E dispersion versus in-plane wave number k, as shown in Fig. 41 for a pump rate $P/P_{\mathrm{th}}=3$. The pump spot size is ~30 μm in diameter. The LP condensate is formed in an area determined by the pump spot size and the pump rate due to the limited lateral diffusion and varying spatial density of the LPs (Deng *et al.*, 2007; Lai *et al.*, 2007). Figure 41(a) represents a linear plot of the luminescence intensity, while Figs. 41(b)–41(d) employ logarithmic plots of the intensity to magnify the excitation spectra. Above threshold, two drastic changes are noticed compared to the standard quadratic dispersion observed below threshold. One is the blueshift of the $k=0$ LP energy as discussed in Sec. VIII.C and the other is the phononlike linear dispersion relation at low-momentum regime $|k\xi|<1$, where $\xi=\hbar/\sqrt{2mU(n)}$ is the healing length. White and black lines in Fig. 41(b) represent the two quadratic dispersion relations, $E_{\mathrm{LP}}=-U(n)+(\hbar k)^2/2m$ and $E'_{\mathrm{LP}}=(\hbar k)^2/2m$, where m is the effective mass of the $k=0$ LP. Here we choose the zero energy as the (blueshifted) condensate mean-field energy for convenience. Neither of the two theoretical curves can explain the measurement result. A solid pink line in Fig. 41(b) is Bogoliubov excitation energy (127), which can be rewritten as (Pitaevskii and Stringari, 2003; Ozeri *et al.*, 2005)

$$E_B=\sqrt{E'_{\mathrm{LP}}[E'_{\mathrm{LP}}+2U(n)]}=U(n)\sqrt{(k\xi)^2[(k\xi)^2+2]}. \tag{129}$$

The measured dispersion relation for the excitation energy versus in-plane wave number is in good agreement with the Bogoliubov excitation spectrum without any fitting parameter.

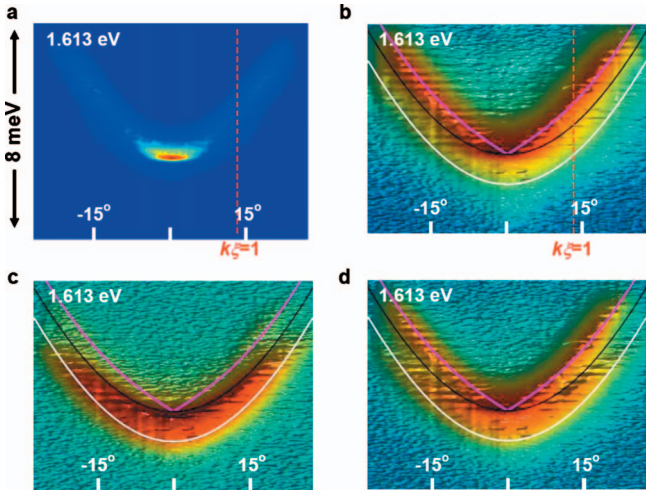

FIG. 41. (Color) Polarization dependence of the excitation spectrum for an untrapped condensate system. (a) A linear plot of the intensity, while (b)–(d) employ three-dimensional logarithmic plots of the intensity to magnify the excitation spectra. A circularly polarized pump beam was incident with an angle of 60°. Three detection schemes: (a) and (b) detection of the leakage photons with the cocircular polarization as the pump beam, (c) detection of the cross-circular polarization, and (d) detection of a small amount of mixture of the cocircular polarization with the cross-circular polarization. The theoretical curves represent the Bogoliubov excitation energy E_B (pink line), the quadratic dispersion relations E'_{LP} (black line) which starts from the condensate energy, and the noninteracting free LP dispersion relation E_{LP} (white line) which is experimentally determined by the data taken far below the threshold $P=0.001P_{\mathrm{th}}$. From Utsunomiya *et al.*, 2008.

A circularly polarized pump-laser beam was used to inject spin-polarized LPs in this experiment. In this case, the LP condensate preserves the original spin polarization of optically injected LPs as described in Sec. VIII.C (Deng *et al.*, 2003; Roumpos, Hoefling, *et al.*, 2009). The result shown in Fig. 41(b) was taken for detecting the leakage photons with the same circular polarization as that of the pump (cocircular detection). A small amount of cross-circularly polarized photons was also detected because of spin relaxation during the cooling process (Deng *et al.*, 2003; Roumpos, Hoefling, *et al.*, 2009). However, the standard quadratic dispersion was observed but with slightly lower energy, compared to the condensate energy, as shown in Fig. 41(c). With increasing pump rate, the number of the condensed LPs is increased so that the weak attractive interaction between the condensate and excited states with the opposite spin results in a slight redshift compared to E'_{LP} (black line) in Fig. 41(c). In Fig. 41(d) we simultaneously detected a small amount of the cocircular polarized photons with the cross-circular polarized photons. The difference between the Bogoliubov excitations with cocircular polarization and the standard but redshifted quadratic excitation with cross-circular polarization is clearly seen.

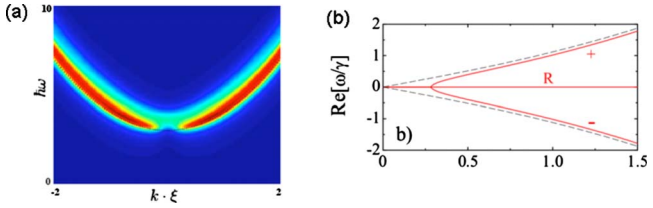

FIG. 42. (Color online) Excitations of a condensate. (a) False color contour plot of the density of states for elementary excitations of a finite-size polariton condensate (Utsunomiya *et al.*, 2008). (b) The dispersion of elementary excitations of a dissipative polariton condensate (Wouters and Carusotto, 2007).

As shown in Fig. 41(b), the condensate at an energy E'_{LP} stretches to a finite wave number $k \neq 0$, which is not expected from the Bogoliubov dispersion law [Eqs. (127) and (128)]. This experimental result has two possible explanations. One explanation is the Heisenberg uncertainty relationship between the position and the momentum of condensate particles. The spatial extent of the polariton condensate is determined by the pump spot size and the size-dependent critical density (Deng *et al.*, 2003), as discussed in Sec. VII. It is expected that the condensate has a finite momentum uncertainly Δp when it is confined in a finite space region. Indeed, the measured product of the spot size Δx and the spread in momentum Δp is close to the minimum allowable value, $\Delta x \Delta p = \hbar/2$, within a factor of 2–4 above the threshold (Utsunomiya *et al.*, 2008). It is also shown by the spatially inhomogeneous Gross-Pitaevskii equation that the density of states for the excitation spectrum disappears in a small momentum regime $|\Delta p| \leqslant \hbar/2\Delta x$ as shown in Fig. 42(a), for which the condensate at E'_{LP} fills in the vacant momentum regime (Utsunomiya *et al.*, 2008).

The other possible explanation is the finite lifetime of condensate particles. Using a generalized Gross-Pitaevskii equation with polariton loss and gain terms, it can be found that the dispersion of elementary excitations around the condensate becomes diffusive, i.e., is flat in a small momentum regime and then rises up to approach the Bogoliubov spectrum (superfluidity-diffusion crossover), as shown in Fig. 42(b) (Szymanska *et al.*, 2006; Wouters and Carusotto, 2007). It is not well understood at present which of the above two factors, a finite condensate size or a finite condensate lifetime, is mainly responsible for the observed flat dispersion near $k=0$.

E. Universal features of Bogoliubov excitations

As indicated by Eq. (129), the Bogoliubov excitation energy normalized by the mean-field energy shift $E_B/U(n)$ is a universal function of the wave number normalized by the healing length $k\xi$. In Fig. 43(a), this universal relation (green solid line) is compared to the experimental results for four different condensate systems with varying detuning parameters. In both the phononlike regime at $|k\xi| < 1$ and the free-particle regime at $|k\xi| > 1$, the experimental results agree well with the universal curve except for the region of small momenta $|k\xi| \ll 1$ as mentioned above. On the other hand, at a pump rate far below threshold, the measured dispersion relation is completely described by the single LP dispersion E_{LP} (red solid line).

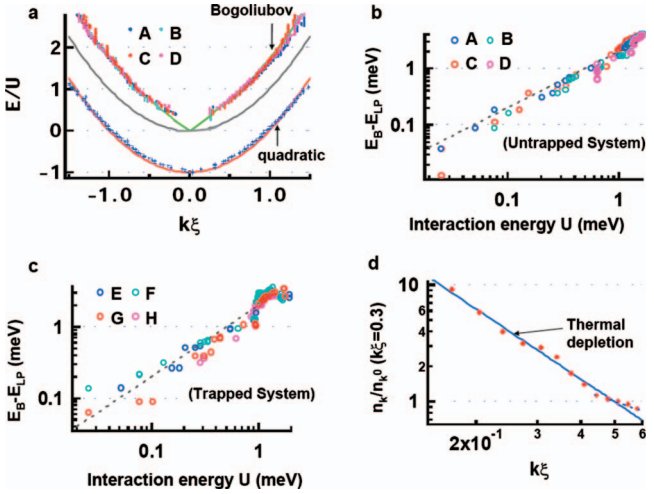

FIG. 43. (Color) Universal features of Bogolinbor excitations. (a) Excitation energy normalized by the interaction energy $E/U(n)$ as a function of normalized wave number $k\xi$ for four different untrapped condensate systems. A (blue dot): $\Delta = 1.41$ meV, $P = 4P_{\mathrm{th}}$ ($P_{\mathrm{th}} = 6.3$ mW); B (light blue dot): $\Delta = 0.82$ meV, $P = 8P_{\mathrm{th}}$ ($P_{\mathrm{th}} = 8.2$ mW); C (red dot): $\Delta = 4.2$ meV, $P = 4P_{\mathrm{th}}$ ($P_{\mathrm{th}} = 6.4$ mW); and D (pink dot): $\Delta = -0.23$ meV, $P = 24P_{\mathrm{th}}$ ($P_{\mathrm{th}} = 8.2$ mW). The experimental data far below threshold are also plotted by blue crosses for system A. Three theoretical dispersion curves normalized by the interaction energy are plotted; the Bogoliubov excitation energy $E_B/U(n)$ (green solid line), the quadratic dispersion curves $E'_{\mathrm{LP}}/U(n)$ (gray solid line), and the free LP dispersion $E_{\mathrm{LP}}/U(n)$ (red solid line). (b) and (c) The energy shift $E_B - E_{\mathrm{LP}}$ in the free-particle regime ($|k\xi| = 1$) plotted as a function of the interaction energy $U(n)$ for the same four different untrapped systems as in (a) and (b) and four different trapped systems (c), where trapped condensate systems are labeled as below: E (blue circle): d(diameter) $= 7$ μm, $\Delta = 3.3$ meV; F (light blue circle): $d = 7$ μm, $\Delta = 2.9$ meV; G (red circle): $d = 8$ μm, $\Delta = 1.6$ meV; and H (pink circle): $d = 8$ μm, $\Delta = 2.5$ meV. The dashed line represents the theoretical prediction $E_B - E_{\mathrm{LP}} = 2U(n)$. (d) LP population distribution normalized by the value at $k\xi = 0.3$ for the trapped system G [in (c)] at the pump rate; $P = 2P_{\mathrm{th}}$ ($P_{\mathrm{th}} = 4$ mW). Theoretical $1/k^2$ dependence for the thermal depletion is shown by the blue line and $1/k$ dependence for the quantum depletion is shown by the blue dotted line. From Utsunomiya *et al.*, 2008.

The sound velocity deduced from the phononlike linear dispersion spectrum is of the order of $\sim 10^8$ cm/s and is proportional to the square root of the condensate population ($\propto \sqrt{n_0}$) at reasonable pump rates. This value is eight orders of magnitude larger than that of atomic BEC and four orders of magnitude larger than that of superfluid ^{4}He. This enormous difference comes from the fact that the LP mass is nine to ten orders of magnitude smaller than the atomic mass and the LP interaction energy is six to seven orders of magnitude larger

than the atomic interaction energy. According to Landau's criterion (Landau and Lifshitz, 1987), the observation of this linear dispersion at low-momentum regime is an indication of superfluidity in the exciton-polariton system. It has recently been reported that the scattering rate for the moving exciton-polariton condensate is dramatically suppressed when the initial velocity given to the polariton system is lower than this critical velocity (Amo *et al.*, 2009). It was also observed that the Bogoliubov theory does not fit to the measured dispersion of elementary excitations at very high pump rates. This is an expected result because the Bogoliubov theory is based on the weakly interacting Bose gas and this approximation is violated at a pump rate far above threshold.

In the free-particle regime ($|k\xi|>1$), the excitation energy associated with the condensate is larger by $2U(n)$ than that of a single LP energy for the same wave number. A factor of 2 difference between the mean-field energy shifts of the condensate and excited states originates from a doubled exchange interaction energy among different modes. The fact was already manifested in the kink observed in Fig. 40. In Figs. 43(b) and 43(c), this important prediction of the Bogoliubov theory is compared to the experimental results for four different untrapped and trapped condensate systems, respectively. The experimental data were determined as the difference between the measured excitation energy with the presence of the condensate and the standard quadratic dispersion for a single LP state, which is determined by the experimental data obtained for a pump rate far below threshold ($P/P_{\mathrm{th}}\ll 1$). The experimental data are in good agreement with the theoretical curve (gray dashed line) for both untrapped and trapped cases.

F. Thermal and quantum depletion

Figure 43(d) shows the normalized excitation population n_k/n_k^0 versus the normalized wave number $|k\xi|$ for a trapped condensate, where n_k^0 is evaluated at $|k\xi|=0.3$ for convenience. The LP occupation number n_k in the excitation spectrum can be calculated by applying the Bose-Einstein distribution for the Bogoliubov quasiparticles and subsequently taking the inverse Bogoliubov transformation (Pitaevskii and Stringari, 2003),

$$n_k = |v_{-k}|^2 + \frac{|u_k|^2 + |v_{-k}|^2}{\exp(\beta E_B) - 1}, \tag{130}$$

where

$$u_k, v_{-k} = \pm \left[\frac{(\hbar k)^2/2m + U(n)}{2E_B} \pm \frac{2}{1} \right]^{1/2}$$

and $\beta=1/k_BT$. The first and second terms on the right-hand side of Eq. (130) represent the real particles (LPs) created by the quantum depletion and the thermal depletion, respectively. In the present LP condensate system, the thermal depletion is much stronger than the quantum depletion so that the second term on the right-hand side of Eq. (130) dominates over the first term. In this case, the LP population is given by $n_k \approx mk_BT/(\hbar k)^2$ at $|k\xi|\ll 1$ regime, while $n_k \approx (1/2\sqrt{2})/k\xi$ if the quantum depletion is dominant (Pitaevskii and Stringari, 2003). The theoretical prediction of the $1/k^2$ dependence of n_k for thermal depletion is compared to the experimental data in Fig. 43(d) and reasonable agreement was obtained.

G. Quantized vortices

A hallmark of superfluidity is quantized vortices. In a BEC phase, vortices appear when finite angular momentum is transferred to the condensate. A uniform 2D system of bosons does not undergo BEC at finite temperatures. However, such a system turns superfluid in the BKT phase (see discussion in Sec. II.D.1). Elementary excitations of this superfluid phase are bound pairs of vortices with opposite winding numbers. The BKT to normal-fluid-phase transition is identified by the dissociation of the vortex pair into free vortices (Hadzibabic *et al.*, 2006; Posazhennikova, 2006).

A quantized vortex of LPs was first observed in a CdTe microcavity. The vortex seemed to be created during the thermalization process and was pinned by a crystal defect induced potential fluctuation (Lagoudakis *et al.*, 2008). A fixed winding direction of the observed vortex was attributed to a specific potential landscape.

Recently vortex-antivortex pairs were observed in a finite-size GaAs microcavity (Roumpos, Hoefling, *et al.*, 2009). According to the numerical analysis of the Gross-Pitaevskii equation, a vortex-antivortex pair in the BKT topological order moves in parallel with a velocity close to the sound velocity of the Bogoliubov excitation spectrum if the 2D system is uniform. If the 2D system is trapped to a finite size, the vortex-antivortex pair is also trapped with a residual micromotion inside a trap (Fraser *et al.*, 2009). The experiment of Roumpos, Hoefling, *et al.* (2009) observed this behavior. In the experiment, the ensemble-averaged 2D distributions of the population $n(r)$, phase $\phi(r)$, and first-order spatial coherence function $g^{(1)}(r)$ are measured simultaneously by a Michelson interferometer. The existence of a vortex-antivortex pair is identified by the population dip, π phase shift, and reduced spatial coherence at the boundary of the pair. These experimental results are successfully reproduced by the numerical analysis of the Gross-Pitaevskii equation with a gain-loss term.

IX. POLARITON CONDENSATION IN SINGLE TRAPS AND PERIODIC LATTICE POTENTIALS

Most of the experiments we discussed in this review used planar microcavities without an intentional in-plane trapping potential. The size of the system is largely determined by the spot size of the pump laser. In comparison, a trapped polariton system may offer several advantages. With a trapping potential, genuine BEC becomes possible in two dimensions, and spatial condensation accompanies the configuration-space condensa-

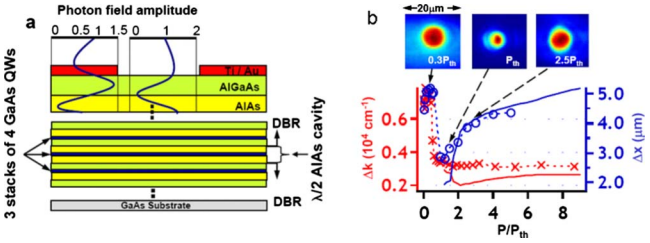

FIG. 44. (Color online) Polariton condensation in an optical trap by metal masks. (a) A schematic of a polariton trap. (b) The measured standard deviations of LP distribution in coordinate Δx (circles) and in wave number Δk (crosses) are plotted as a function of P/P_{th}. Theoretical values for Δx and Δk obtained by the GP equation are shown by the solid lines (Utsunomiya *et al.*, 2008).

tion. A strong trapping potential may lead to discrete polariton modes, hence single-mode BEC. Signatures of BEC should be more pronounced in all these cases. The trap can also serve as a tuning knob for the system. With a lattice potential, coherence and interactions among multiple condensates can be studied. In this section, we review the efforts to implement single and lattice potentials for polaritons.

A. Polariton traps

A single isolated trap for polaritons is implemented by modifying either the cavity photon or the QW exciton energies.

1. Optical traps by metal masks

A rather versatile type of polariton trap is based on modulating the cavity layer thickness and transmission with a thin metal mask deposited on the surface of the microcavity (Lai *et al.*, 2007; Kim *et al.*, 2008; Utsunomiya *et al.*, 2008).

As shown in Fig. 44(a), a trap potential of ~200 μeV is provided by a hole surrounded by a thin metal (Ti/Au) film (Lai *et al.*, 2007; Utsunomiya *et al.*, 2008). The cavity resonant field has normally an antinode at the AlGaAs-air interface. However, the antinode position is shifted inside the AlGaAs layer with the metal film as shown in Fig. 44(a), which results in the blueshift of the cavity photon and subsequently LP resonances. The LPs were confined in circular holes of varying diameters from 5 to 100 μm. In a trap with 5–10 μm diameter, a single fundamental transverse mode dominates the condensation dynamics over higher-order transverse modes due to the relatively weak confining potential. A weak confining potential helps to cool polaritons efficiently because high-energy polaritons created by two-body scattering are quickly expelled from the trap region.

The top panels in Fig. 44(b) show the near-field-emission patterns from a trap with 8 μm diameter at pump rates below, just above, and well above condensation threshold. The measured standard deviations for the LP position Δx and wave number Δk are plotted as a function of P/P_{th} in Fig. 44(b). The sudden decreases in Δx and Δk were clearly observed at threshold $P \cong P_{\text{th}}$. Just above threshold, the measured uncertainty product $\Delta x \Delta k$ is ~0.98, which is compared to the Heisenberg limit ($\Delta x \Delta k \sim 0.5$) for a minimum uncertainty wave packet. Here $\sim 10^3$ LPs condense into a nearly minimum uncertainty wave packet at threshold. The monotonic increase in Δx and $\Delta x \Delta k$ at higher pump rates stems from the repulsive interaction among LPs in a condensate and is well reproduced by the numerical analysis using the spatially inhomogeneous GP equation as shown by solid lines in Fig. 44(b).

2. Optical traps by fabrication

Strong optical confinement, hence discrete polariton modes, has been realized by modifying the microcavity structure. Earlier efforts focused on etching small pillar structures out of a planar microcavity to achieve strong transverse confinement of the photon modes. In pillars of a few microns across, discrete polariton modes (Bloch *et al.*, 1998; Gutbrod *et al.*, 1998; Obert *et al.*, 2004) and polariton parametric scattering (Dasbach *et al.*, 2001) were observed. In very small pillars, leakage of the cavity-photon fields and loss of excitons at the side walls prevent strong coupling.

Alternatively, in a similar spirit as the metal masks, Daif *et al.* (2006) devised a way to grow small regions with thicker cavity layers and lower photon (and thus polariton) energies. Compared to using metal masks, the energy difference between inside and outside the trap region is large enough to discretize the polariton modes. Compared to the etching method, the QW excitons are untouched and will not suffer surface recombination; transport and interactions are possible between untrapped and trapped polaritons. Discrete polariton spectra were observed in such a structure, in agreement with calculations (Kaitouni *et al.*, 2006).

3. Exciton traps by mechanical stress

A polariton trap with a relatively larger area has been formed by mechanically pressing a planar microcavity wafer (Balili *et al.*, 2006). The mechanical stress introduces a strain field which acts as a harmonic potential on the QW excitons (Negoita *et al.*, 1999) and thus on the polaritons as well. A potential up to about 5 meV deep was created by a stressing tip of about 50 μm in radius. LPs excited away from the trap center drifted over more than 50 μm into the trap (Balili *et al.*, 2006). Condensation of LPs in the trap was also observed, with a threshold density lower than that required when without the trap and with a contracted spatial profile (Balili *et al.*, 2007).

B. Polariton array in lattice potential

Extending a single trap potential to a lattice potential, the long-range spatial coherence leads to the existence

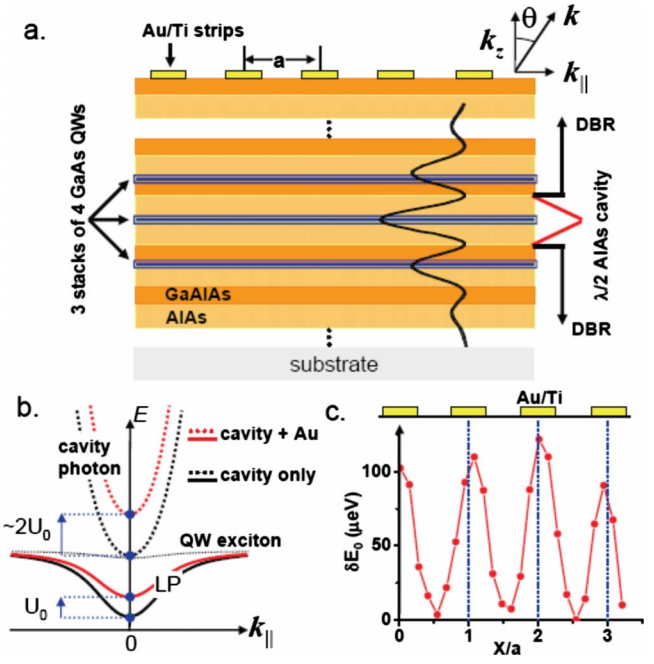

FIG. 45. (Color online) Formation of a polariton array. (a) A schematic of a polariton array formed by depositing periodic thin metallic strips (Au/Ti) on top of a microcavity structure. (b) Dispersion curves of the cavity-photon mode and LP. (c) Spatial LP energy modulation is detected from the position-dependent central energy of LP emissions. From Lai *et al.*, 2007.

of phase-locked multiple condensates, such as in an array of superfluid helium (Davis and Packard, 2002), superconducting Josephson junctions (Hansen and Lindelof, 1984; Hadley *et al.*, 1988; Cataliotti *et al.*, 2001), and atomic BECs (Anderson and Kasevich, 1998; Cataliotti *et al.*, 2001; Orzel *et al.*, 2001; Greiner *et al.*, 2002). Under certain circumstances, a quantum phase difference of π is predicted to develop among weakly coupled Josephson junctions (Bulaevskii *et al.*, 1977). Such a metastable π state was discovered in a weak link of superfluid ^{3}He, which is characterized by a p-wave order parameter (Backhaus *et al.*, 1998). Possible existence of such a π state in weakly coupled atomic BECs has also been proposed (Smerzi *et al.*, 1997) but remains undiscovered in atomic systems. Recently Lai *et al.* (2007) observed spontaneous buildup of in-phase (zero-state) and antiphase (π-state) coherent states in a polariton condensate array connected by weak periodic potential barriers. These states reflect the band structure of the one-dimensional periodic potential for polaritons and feature the dynamical competition between metastable and stable polariton condensates.

1. One-dimensional periodic array of polaritons

Employing the same metal deposition technique described in Sec. IX.B, an array of one-dimensional cigar-shaped polaritons is created by the deposition of periodic strips of a metallic thin film on the top surface of a microcavity structure, as shown in Fig. 45(a). Under the metallic layer, the cavity resonance energy $E_{\rm cav}$ (for $k_\parallel=0$) is expected to increase by ~400 μeV according to the transfer-matrix analytical method (Yeh, 2005). When the cavity photon ($E_{\rm cav}$) is near resonance with the QW exciton ($E_{\rm exc}$) at $k_\parallel=0$, the shift of the LP energy induced by the metallic layer is ~200 μeV, approximately one-half of the cavity-photon resonance shift [Fig. 45(b)]. Therefore, the LPs are expected to be trapped in the gap region where the LP energy is lower. The measured spatial modulation of LP energy is ~100 μeV, which is less than the theoretical prediction due to the diffraction-limited spatial resolution (~2 μm) of our optical detection system [Fig. 45(c)].

The microcavity is excited by a mode-locked Ti:sapphire laser with an ~2.5 ps pulse near the QW exciton resonance at an incident angle of 60°, corresponding to an in-plane wave number $k_\parallel \approx 7\times10^4$ cm^{-1} in air. The large $k_\parallel$ of the pump assures that the coherence of the pump laser is lost by multiple phonon emissions before the LPs scatter into $k_\parallel \approx 0$ states.

Considering a periodic and coherent array of condensates aligned along the x axis, we can approximate the order parameter in momentum space as (Pedri *et al.*, 2001)

$$\psi(k_x) = \psi_0(k_x) \sum_{n=0,\pm1,\ldots,\pm n_M} e^{{\rm i}n(k_x a+\phi)} = \psi_0(k_x)\frac{\sin[Nk_x a/2]}{\sin[k_x a/2]} \quad (\text{if } \phi=0), \tag{131}$$

where n labels the condensate array element, $N=2n_M+1$ is the total number of periodic array elements, a is the pitch distance between two neighboring elements, and $\psi_0(k_x)$ is the momentum-space wave function of an individual element. The overall momentum distribution $\rho(k_x)=|\psi(k_x)|^2$ reflects the coherence properties and nature of the condensate arrays through distinctive interference patterns. In the presence of the periodic lattice, the momentum distribution displays narrow peaks at $k_x=m\times 2\pi/a$ ($m\in$ integer) with an envelope function given by $|\psi_0(k_x)|^2$. If all the elements are locked in phase ($\phi=0$), at a LP wavelength $\lambda=780$ nm and a grating pitch distance $a=2.8$ μm, a Fraunhofer diffraction pattern has a central peak at $\theta=0°$ and two side lobes at $\theta=\sin^{-1}\lambda/a\approx\pm16°$ ($k_\parallel=\pm2\pi/a$, $m=\pm1$ first-order diffraction). The LP emissions from a polariton condensate array are expected to display such an interference pattern in momentum space, just like in an atomic BEC experiment (Anderson and Kasevich, 1998; Cataliotti *et al.*, 2001; Orzel *et al.*, 2001; Greiner *et al.*, 2002).

The observed LP distributions in both coordinate and momentum space of the condensate array are shown in Figs. 46(a) and 46(b). Below the condensation threshold, the near-field image reveals the cigar-shaped LP emissions through the 1.4-μm-wide gaps between the metallic strips. The corresponding LP momentum distribution is broad and isotropic, independent of the periodic modulation of LP population and the elliptically shaped pumping spot. The result indicates that there is negli-

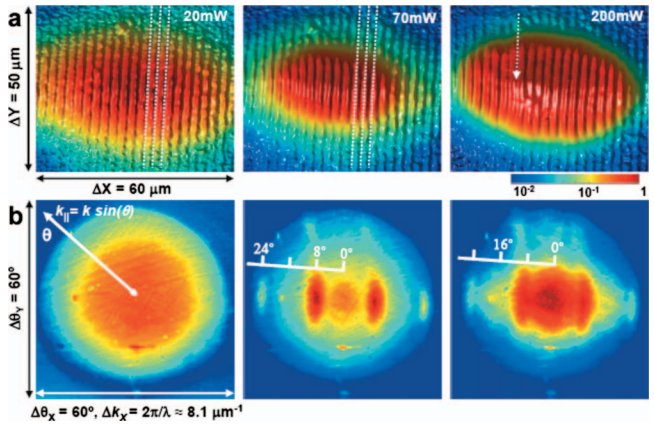

FIG. 46. (Color) Near-field and far-field images of polaritons in a one-dimensional array. (a) Near-field images showing the LP distribution across a polariton array in coordinate space under pumping powers of 20, 70, and 200 mW (left to right). The threshold pumping power is about 45 mW. (b) Corresponding far-field images showing the LP distribution in momentum space. From Lai *et al.*, 2007.

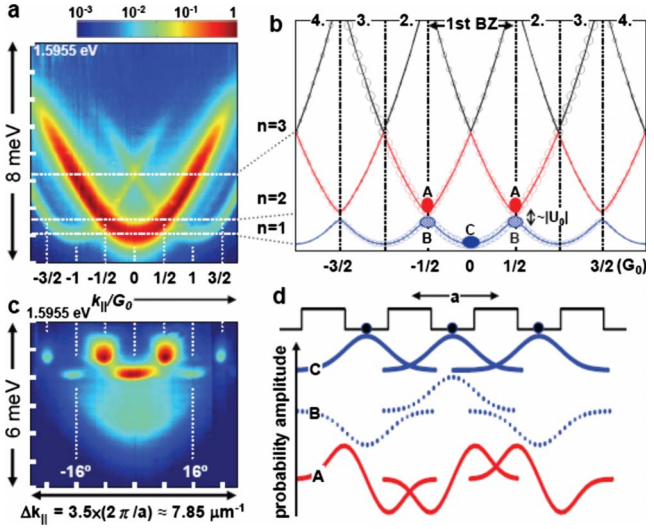

FIG. 47. (Color online) Energy-momentum dispersions and real space wave functions of polaritons in a one-dimensional array. (a) Time-integrated energy vs in-plane momentum of a polariton array at near resonance $E_{cav} \approx E_{exc}$. The pumping power is $P=10$ mW (below threshold). (b) Extended-zone scheme of the band structure for the polariton array under a weak periodic potential with a lattice constant a. (c) Energy vs in-plane momentum of a polariton condensate array at blue detuning $E_{cav}-E_{exc} \approx 6$ meV above threshold ($P=40$ mW). (d) Schematic of the Bloch wave functions for states labeled as A–C in (b). From Lai *et al.*, 2007.

gible phase coherence among different cigar-shaped LPs. With an increasing pumping rate, two strong and two weak side lobes emerge at $\theta \approx \pm 8°$ and $\pm 24°$, which correspond to $k_{\parallel} = \pm \pi/a$ and $\pm 3\pi/2a$, respectively. The particular diffraction pattern suggests that the phase difference of adjacent condensates in the array is locked exactly to π [i.e., $\phi = \pi$ in Eq. (131)]. Moreover, the corresponding near-field image [Fig. 46(a)] reveals that strong LP emission is generated from under the metallic strips rather than from the gaps. The dramatic contrast is better observed near the boundary of the central condensate and the outside thermal LP emissions, which come through the gaps. The dominant LP emission through the metallic layers despite the lower transmission indicates that LP condensates are strongly localized under the metallic strips. With a further increasing pumping rate, the intensity of the central peak near $\theta = 0°$, with weak side lobes at $\theta \approx \pm 16°$, gradually surpasses the peaks at $\theta \approx \pm 8°$ and $\pm 24°$ [Fig. 46(b)]. Simultaneously, the dominant LP emission is observed through the gaps.

These two distinct interference patterns suggest the transition from an antiphase state localized under the metallic strips to an in-phase state localized in the gaps. Both the zero and π state can be observed for a polariton condensate array consisting of more than 30 strips of condensates (total array dimension ~ 100 μm). These collective states are manifestations of the long-range spatial coherence as well as phase locking across the array.

2. Band structure, metastable π state, and stable zero-state

Figure 47(a) shows the energy versus in-plane momentum dispersion relation for a one-dimensional LP array near resonance $E_{cav} \approx E_{exc}$ and below threshold. From the dispersion curve, we deduce the LP kinetic energy at $k_{\parallel} = G_0/2 = \pi/a$ (one-half of the primitive reciprocal-lattice vector), $E_k = \hbar^2 (G_0/2)^2 / 2m^* \approx 500$ μeV, where the LP effective mass $m^* = 9 \times 10^{-5} m_e$. We deduce the band structure of the polariton array assuming a "nearly free polariton" in the presence of the periodic square-well potential. Given a one-dimensional periodic potential $U(X)$ with a lattice constant a, the band structure can be obtained using the standard Bloch wave-function formalism. Only those LPs with in-plane momentum close to the Bragg condition ($k_{\parallel} = mG_0/2$, $m \in$ integer) are subject to backscattering due to the periodic potential, and gaps appear at these Bragg planes where standing waves are formed. Similar to the standard extended-zone scheme (Madelung, 1996), the band structure can be constructed by starting with original and displaced parabolas $E_{LP}(k_{\parallel} \pm mG_0)$ as shown in Fig. 47(b). Here the size of from thermal population of LPs. This is well reproduced in the observed LP energy versus in-plane momentum with a below threshold pumping rate [Fig. 47(a)]. The first band gap is on the order of the barrier potential, $|U_0| \simeq 200$ μeV, between the first and second bands near the zone boundaries (Bragg planes). This small gap is masked in the measured spectra by the large inhomogeneous broadening of the LP emission lines (linewidth ~ 500 μeV).

In Fig. 47(c), the energy versus in-plane momentum of a polariton condensate array above threshold and $E_{cav} - E_{exc} \approx \pm 6$ meV is shown. Above threshold, LP emissions occur in two states with an energy difference of about 1 meV. These two states with emission peaks at

$k_{\parallel}=0,\pm G_0$ and at $k_{\parallel}=\pm G_0/2,\pm 3G_0/2$ correspond to the aforementioned zero and π state, respectively.

On referring to the multivalley band structure [Fig. 47(b)], the dynamic condensation process of the polariton array becomes transparent. Without the spatial modulation, the quasistationary state of the LP condensate is the lowest-energy state at $k_{\parallel}=0$. Here the bottom of LP dispersion parabola serves as a trap of LPs in momentum space. When the spatial potential modulation is introduced, a metastable dynamic condensate can occur near the bottom of the second band [point A in Fig. 47(b)] when the pumping rate is just above threshold. In these points, LPs experience a relaxation bottleneck, resulting in metastable condensates. Eventually, the LP system will relax to the lowest-energy state [point C in Fig. 47(b)] as the pumping rate is increased.

To understand the spatial distributions of LPs in the array [near-field images shown in Fig. 46(a)], the Bloch wave functions must be considered for the above two states. The Bloch wave functions for these eigenstates exhibit not only opposite relative phase between adjacent elements in the array but also different orbital wave functions. Schematic Bloch wave functions for selected eigenstates labeled as A–C in Fig. 47(b) are shown in Fig. 47(d). The zero state at point C carries to the *s*-like wave with maximal amplitude in potential wells and identical phase between adjacent elements across the array. The wave functions of A and B at $k_{\parallel}=G_0/2$ both exhibit a relative π phase difference between adjacent elements. The lower energy unstable state at point B corresponds to antibonding of *s* waves, while the higher energy metastable state at point A corresponds to antibonding of *p* waves. As the atomic *p* wave, the LP density vanishes at the center of the potential well for this π state. This explains the near-field imaging shown in Fig. 46(a). Under the weak potential modulation, the Bloch wave functions are superpositions of forward-and-backward traveling plane waves at the zone boundary and have a relatively broad distribution in space compared to the standard tight-binding model of a normal condensed-matter system.

The metastability of the π state (antibonding of *p* waves) is a unique property for dynamic polariton condensates. Under strong pumping rates, the zero state (bonding of *s* waves) dominates eventually due to enhanced cooling by stimulated LP-LP scattering at high densities. A typical evolution from the metastable π state to the stable zero state is illustrated by the LP momentum distribution profiles for various pumping rates in Fig. 48. At a high pumping rate, the LP emission from the zero state surpasses that from the π state by more than one order of magnitude.

3. Dynamics and mode competition

The π state consisting of local *p*-type wave functions is a metastable state with a higher energy than the zero state consisting of local *s*-type wave functions. Both states decay to the crystal ground state by emitting photons with a finite lifetime. After high-energy excitonlike

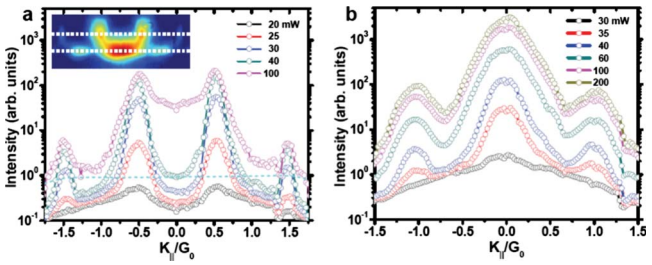

FIG. 48. (Color online) Momentum distribution profiles of the π phase connected *p* state and zero phase connected *s* state of polaritons in a one-dimensional array. (a) Profiles of the "π state" as a function of in-plane momentum taken at a cross section in the dispersion curve (inset) for a polariton condensate array for various pumping rates. (b) Profiles of the "zero state." The intensity of the zero state surpasses that of the π state at around $P=45$ mW. From Lai *et al.*, 2007.

LPs with large in-plane wave number $k_{\parallel}$ are optically injected into the system, they cool down to the metastable π state first by continuously emitting phonons or via LP-LP scattering. If the decay rate of the π state is slower than the loading rate into the π state, the population of the π state exceeds 1 (quantum degeneracy condition) and induces the bosonic final-state stimulated scattering into this mode. This is similar to a so-called bottleneck condensation effect (Tartakovskii *et al.*, 2000; Huang *et al.*, 2002). Here the LPs with finite *k* dynamically condense due to the slow relaxation rate into the $k\approx 0$ region, where the density of states is reduced.

When the pump rate is further increased, the zero state eventually acquires the population greater than 1. The onset of stimulated scattering into the zero state from the metastable π state favors the condensation at the zero state. The reverse stimulated process from the zero to the π state requires the absorption of phonons and thus is energetically unfavorable. This mode competition behavior is well described by the coupled Boltzmann (rate) equation analysis (Lai *et al.*, 2007).

Assuming reasonable numerical parameters, the qualitative agreement with the experimental results is obtained. With increasing pumping, the π state appears first and then is surpassed by the dominant zero state, consistent with experimental observation. The time-resolved LP emissions from the zero and π state are shown in Fig. 49. The simple rate equations with parameters fixed for all pumping rates can describe the observed mode competition.

X. OUTLOOK

With regard to fundamental physics of polariton BEC, it is important to understand the ground state as well as the excitations of the quantum phases to establish the experimental phase diagram of the polariton system and to compare experiments with theoretical analysis taking into account both thermal and quantum depletions of a condensate. The dynamical nature of the polariton condensate due to the short polariton lifetime imposes chal-

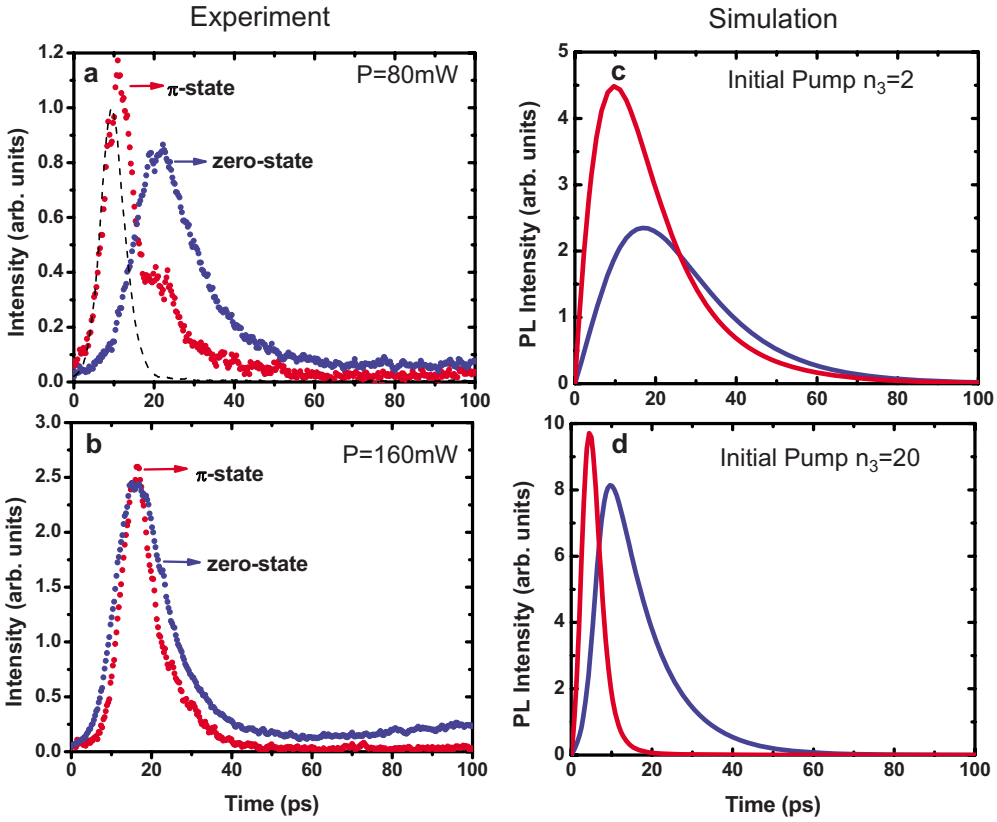

FIG. 49. (Color online) Dynamics of the zero and π state. (a) LP dynamics measured by a streak camera system. The black dashed curve in (a) is the system response measured with scattered laser pulse from the sample. (b) Simulation. From Lai *et al.*, 2007.

lenges on this kind of study. Fortunately, the Q value of a GaAs microcavity has been dramatically improved recently (Reitzenstein *et al.*, 2007), so one may expect a quantitative comparison between theory and experiment in the near future.

The quantum-statistical properties of the BEC ground state are expected to be influenced by phase locking between the condensed particles at $k_{\|}=0$ and excitations at $\pm k_{\|}\neq 0$ (Nozieres, 1995). The current polariton BEC is still limited by thermal depletion, but with high-Q microcavities and more efficient cooling schemes the quantum nature of the BEC ground state should be elucidated soon.

Superfluidity associated with polariton BEC is another urgent issue. A first sign has been reported on the sound velocity (Utsunomiya *et al.*, 2008), and preliminary results on quantized vortices have been reported recently (Lagoudakis *et al.*, 2008). A more quantitative study on quantized vortices, in particular, dynamical formation process of vortices in a rotating polariton condensate, is needed.

The crossover from polariton BEC in a relatively small 2D polariton system to a BKT phase in a relatively large 2D system is an interesting topic in studying the polariton phase diagram. The decay of the first-order spatial coherence, the recombination of thermally excited vortices, as well as the temperature dependence of a fractional condensate will be decisive experimental signatures for the BEC-BKT crossover. The crossover from polariton BEC to electron-hole BCS phase is another intriguing topic. With increasing exciton density to above the Mott density, excitons overlap with each other and both the electron and hole liquids are normal except at the Fermi surface. The remaining binding energy is expected to create a gap at the Fermi energy. A measurement of the eigenenergies will help elucidate the crossover behavior.

The complex phase diagram and rich physics of the polariton system make it a unique candidate for the quantum simulation of many-body Hamiltonians in one and two dimensions. The superfluid to Mott insulator (or Bose glass) phase transition in two dimensions and Tanks gas in one-dimensional polariton systems have been addressed theoretically so far, while intense experimental research is underway.

With regard to applications of polariton BEC, most promising is a polariton BEC as a low-threshold source of coherent light. A fundamental limit on the threshold of a standard semiconductor laser is required to create an electronic population inversion in the gain medium: $n\sim a_B^{*-2}$, where a_B^* is the exciton Bohr radius. On the other hand, the polariton BEC threshold is given by $n\sim\lambda_T^2$, where λ_T is the thermal de Broglie wavelength. Since a_B^*/λ_T is on the order of 10^{-2}, the fundamental limit of the polariton BEC threshold density is 10^{-4} of that of a counterpart semiconductor laser. A proof of principle comparison between the two types of lasers

was made by Deng *et al.* (2003) with a GaAs microcavity at liquid helium temperature. Recently Tsintzos *et al.* (2008) demonstrated electronically pumped polariton light-emitting diode operating at 235 K. An electrically pumped BEC with a *p-n* junction diode at high temperatures may soon be within experimental reach.

ACKNOWLEDGMENTS

We wish to acknowledge and thank present and former members of the Stanford group for their contributions to the polariton research reported herein. These researchers include H. Cao, R. Huang, N. Y. Kim, C. W. Lai, S. Pau, G. Roumpos, F. Tassone, L. Tian, S. Utsunomiya, and G. Weihs. We also wish to acknowledge and thank T. D. Doan, H. Thien Cao, and D. B. Tran Thoai at the Vietnam Centre for Natural Science and Technology for their contributions to the theoretical and numerical works reported herein. The research at Stanford at present is supported by the JST/SORST program and Special Coordination Funds for Promoting Science and Technology from University of Tokyo, Japan.

APPENDIX: CALCULATION OF SCATTERING COEFFICIENTS

In this appendix we list the LP-phonon and LP-LP scattering rates for the quasispin kinetics [Eqs. (65) and (68)] of Sec. VI. In the Markov approximation, the LP-phonon-scattering rate of the polariton population $n_{k,i}$ is given by

$$\left.\frac{\partial n_{k,i}}{\partial t}\right|_{\text{scatt}}^{p\text{-ph}} = -\frac{2\pi}{\hbar}\sum_{k'}\{W_{k',k}[n_{k,i}(1+n_{k',i}) + \vec{S}_k\vec{S}_{k'}] - W_{k,k'}[n_{k',i}(1+n_{k,i}) + \vec{S}_k\vec{S}_{k'}]\} \tag{A1}$$

and the LP-phonon-scattering rate of the pseudospin $\vec{S}_k$ is given by

$$\left.\frac{\partial \vec{S}_k}{\partial t}\right|_{\text{scatt}}^{p\text{-ph}} = -\frac{2\pi}{\hbar}\sum_{k'}\left\{W_{k',k}\left(\vec{S}_k + \frac{1}{2}\sum_{i=1,2}(n_{k',i}\vec{S}_k + n_{k,i}\vec{S}_{k'})\right) - W_{k,k'}\left(\vec{S}_{k'} + \frac{1}{2}\sum_{i=1,2}(n_{k,i}\vec{S}_{k'} + n_{k',i}\vec{S}_k)\right)\right\}. \tag{A2}$$

Here the LP-phonon transition rate $W_{k,k'}$ is given in Eq. (37). Similarly, the LP-LP scattering rates are given by

$$\begin{aligned}\left.\frac{\partial n_{k,i}}{\partial t}\right|_{\text{scatt}}^{p\text{-}p} = -\frac{2\pi}{\hbar}\sum_{k',q}\Bigg\{&\delta(e_{k'-q}+e_{k+q}-e_k-e_{k'})\Bigg[|V(k,k',k'-q,k+q)|^2[n_{k,i}n_{k',i}(1+n_{k'-q,i}+n_{k+q,i}) \\ &- n_{k'-q,i}n_{k+q,i}(1+n_{k,i}+n_{k',i})] + |U(k,k',k'-q,k+q)|^2\Bigg[(n_{k,i}n_{k',\bar{i}} + \vec{S}_k\vec{S}_{k'})\Big(2+\sum_{j=1,2}(n_{k'-q,j}+n_{k+q,j})\Big) \\ &- (1+n_{k,i}+n_{k',\bar{i}})\Big(2\vec{S}_{k'-q}\vec{S}_{k+q} + \sum_{j=1,2} n_{k'-q,\bar{j}}n_{k+q,j}\Big)\Bigg] + T(k,k',k'-q,k+q)\Big(\sum_{j=1,2}[(n_{k',j}-n_{k'-q,j})\vec{S}_{k+q}\vec{S}_k \\ &+ (n_{k',j}-n_{k+q,j})\vec{S}_{k'-q}\vec{S}_k] + 2[n_{k,i}(\vec{S}_{k'}\vec{S}_{k'-q} + \vec{S}_{k'}\vec{S}_{k+q}) - n_{k'-q,i}\vec{S}_{k'}\vec{S}_{k+q} - n_{k+q,i}\vec{S}_{k'}\vec{S}_{k'-q}]\Big)\Bigg]\Bigg\},\end{aligned} \tag{A3}$$

$$\begin{aligned}\left.\frac{\partial \vec{S}_k}{\partial t}\right|_{\text{scatt}}^{p\text{-}p} = -\frac{\pi}{\hbar}\sum_{k',q}\Bigg\{&\delta(e_{k+q}+e_{k'-q}-e_k-e_{k'})\Bigg[|V(k,k',k'-q,k+q)|^2\Big(\vec{S}_k\sum_{i=1,2}[n_{k',i}(1+n_{k'-q,i}+n_{k+q,i}) - n_{k'-q,i}n_{k+q,i}] \\ &- 2[\vec{S}_{k+q}(\vec{S}_{k'}\vec{S}_{k'-q}) + \vec{S}_{k'-q}(\vec{S}_{k'}\vec{S}_{k+q}) - \vec{S}_{k'}(\vec{S}_{k'-q}\vec{S}_{k+q})]\Big) \\ &+ |U(k,k',k'-q,k+q)|^2\Bigg[\sum_{i=1,2}(\vec{S}_k n_{k',i} + \vec{S}_{k'}n_{k,i})\Big(2+\sum_{i=1,2}(n_{k'-q,i}+n_{k+q,i})\Big) \\ &- 2(\vec{S}_k+\vec{S}_{k'})\Big(\sum_{i=1,2}(n_{k'-q,i}n_{k+q,\bar{i}}) + 2\vec{S}_{k'-q}\vec{S}_{k+q}\Big)\Bigg] + T(k,k',k'-q,k+q)\Bigg\{4\vec{S}_k(\vec{S}_{k'}\vec{S}_{k'-q} + \vec{S}_{k'}\vec{S}_{k+q}) \\ &+ \vec{S}_{k'-q}\Bigg[\sum_{i=1,2}n_{k,i}\Big(\sum_{i=1,2}(n_{k',i}-n_{k+q,i})\Big) \\ &- 2\sum_{i=1,2}n_{k+q,i}(1+n_{k',i})\Bigg]\vec{S}_{k+q}\Bigg[\sum_{i=1,2}n_{k,i}\Big(\sum_{i=1,2}(n_{k',i}-n_{k'-q,i})\Big) - 2\sum_{i=1,2}n_{k'-q,i}(1+n_{k',i})\Bigg]\Bigg\}\Bigg]\Bigg\}.\end{aligned} \tag{A4}$$

The matrix elements for the relative triplet and singlet configurations are given in Eq. (60).

REFERENCES

Amo, A., D. Sanvitto, F. P. Laussy, D. Ballarini, E. del Valle, M. D. Martin, A. Lemaitre, J. Bloch, D. N. Krizhanovskii, M. S. Skolnick, C. Tejedor, and L. Viña, 2009, Nature (London) **457**, 291.

Anderson, B. P., and M. A. Kasevich, 1998, Science **282**, 1686.

Backhaus, S., S. Pereverzev, R. W. Simmonds, A. Loshak, J. C. Davis, and R. E. Packard, 1998, Nature (London) **392**, 687.

Bagnato, V., and D. Kleppner, 1991, Phys. Rev. A **44**, 7439.

Bajoni, D., P. Senellant, E. Wertz, I. Sagnes, A. Miard, A. Lemaitre, and J. Bloch, 2008, Phys. Rev. Lett. **100**, 047401.

Balili, R., V. Hartwell, D. Snoke, L. Pfeiffer, and K. West, 2007, Science **316**, 1007.

Balili, R. B., D. W. Snoke, L. Pfeiffer, and K. West, 2006, Appl. Phys. Lett. **88**, 031110.

Bányai, L., and P. Gartner, 2002, Phys. Rev. Lett. **88**, 210404.

Bányai, L., P. Gartner, O. M. Schmitt, and H. Haug, 2000, Phys. Rev. B **61**, 8823.

Beliaev, S. T., 1958, Sov. Phys. JETP **34**, 417.

Berezinskii, V. L., 1971, Sov. Phys. JETP **32**, 493.

Berezinskii, V. L., 1972, Sov. Phys. JETP **34**, 610.

Berman, P. R., 1994, *Cavity Quantum Electrodynamics (Advances in Atomic, Molecular and Optical Physics)* (Academic, Boston).

Björk, G., A. Karlsson, and Y. Yamamoto, 1994, Phys. Rev. A **50**, 1675.

Björk, G., S. Machida, Y. Yamamoto, and K. Igeta, 1991, Phys. Rev. A **44**, 669.

Bloch, J., F. Boeuf, J. M. Grard, B. Legrand, J. Y. Marzin, R. Planel, V. Thierry-Mieg, and E. Costard, 1998, Physica E (Amsterdam) **2**, 915.

Bloch, J., and J. Y. Marzin, 1997, Phys. Rev. B **56**, 2103.

Bockelmann, U., 1993, Phys. Rev. B **48**, 17637.

Bogoliubov, N. N., 1947, J. Phys. (USSR) **11**, 23.

Bulaevskii, L. N., V. V. Kuzii, and A. A. Sobyanin, 1977, JETP Lett. **25**, 290.

Butte, R., G. Christmann, E. Feltin, J. F. Carlin, M. Mosca, M. Ilegems, and N. Grandjean, 2006, Phys. Rev. B **73**, 033315.

Cao, H. T., T. D. Doan, D. Thoai, and H. Haug, 2004, Phys. Rev. B **69**, 245325.

Cao, H. T., T. D. Doan, D. B. T. Thoai, and H. Haug, 2008, Phys. Rev. B **77**, 075320.

Carmichael, H. J., 2003, *Statistical Methods in Quantum Optics 1: Master Equations and Fokker-Planck Equations*, 2nd ed. (Springer, Berlin).

Cataliotti, F. S., S. Burger, C. Fort, P. Maddaloni, F. Minardi, A. Trombettoni, A. Smerzi, and M. Inguscio, 2001, Science **293**, 843.

Chen, J. R., T. C. Lu, Y. C. Wu, S. C. Lin, W. R. Liu, W. F. Hsieh, C. C. Kuo, and C. C. Lee, 2009, Appl. Phys. Lett. **94**, 061103.

Christmann, G., R. Butte, E. Feltin, J.-F. Carlin, and N. Grandjean, 2008, Appl. Phys. Lett. **93**, 051102.

Christopoulos, S., G. B. H. von Hogersthal, A. J. D. Grundy, P. G. Lagoudakis, A. V. Kavokin, J. J. Baumberg, G. Christmann, R. Butte, E. Feltin, J. F. Carlin, and N. Grandjean, 2007, Phys. Rev. Lett. **98**, 126405.

Citrin, D. S., and J. B. Khurgin, 2003, Phys. Rev. B **68**, 205325.

Ciuti, C., V. Savona, C. Piermarocchi, A. Quattropani, and P. Schwendimann, 1998, Phys. Rev. B **58**, 7926.

Ciuti, C., P. Schwendimann, and A. Quattropani, 2003, Semicond. Sci. Technol. **18**, S279.

Comte, C., and P. Nozières, 1982, J. Phys. (France) **43**, 1069.

Dasbach, G., M. Schwab, M. Bayer, and A. Forchel, 2001, Phys. Rev. B **64**, 201309(R).

Davis, J. C., and R. E. Packard, 2002, Rev. Mod. Phys. **74**, 741.

Deng, H., D. Press, S. Gotzinger, G. S. Solomon, R. Hey, K. H. Ploog, and Y. Yamamoto, 2006, Phys. Rev. Lett. **97**, 146402.

Deng, H., G. Solomon, R. Hey, K. H. Ploog, and Y. Yamamoto, 2007, Phys. Rev. Lett. **99**, 126403.

Deng, H., G. Weihs, C. Santori, J. Bloch, and Y. Yamamoto, 2002, Science **298**, 199.

Deng, H., G. Weihs, D. Snoke, J. Bloch, and Y. Yamamoto, 2003, Proc. Natl. Acad. Sci. U.S.A. **100**, 15318.

Doan, T. D., H. T. Cao, D. B. T. Thoai, and H. Haug, 2008, Phys. Rev. B **78**, 205306.

Doan, T. D., C. Huy Thien, D. Thoai, and H. Haug, 2005, Phys. Rev. B **72**, 085301.

Doan, T. D., H. Thien Cao, D. B. Tran Thoai, and H. Haug, 2008, Solid State Commun. **145**, 48.

Eastham, P. R., and P. B. Littlewood, 2001, Phys. Rev. B **64**, 235101.

Einstein, A., 1925, Sitzungsber. Preuss. Akad. Wiss., Phys. Math. Kl. **1925**, 3.

El Daif, O., A. Baas, T. Guillet, J. P. Brantut, R. I. Kaitouni, J. L. Staehli, F. Morier-Genoud, and B. Deveaud, 2006, Appl. Phys. Lett. **88**, 061105.

Feshbach, H., 1962, Sugaku **19**, 287.

Fraser, M. D., G. Roumpos, and Y. Yamamoto, 2009, New J. Phys. **11**, 113048.

Gardiner, C. W., and P. Zoller, 2000, *Quantum Noise* (Springer-Verlag, New York).

Glauber, R. J., 1963, Phys. Rev. **130**, 2529.

Greiner, M., O. Mandel, T. Esslinger, T. W. Hänsch, and I. Bloch, 2002, Nature (London) **415**, 39.

Griffin, A., D. W. Snoke, and S. Stringari, 1995, *Bose-Einstein Condensation* (Cambridge University Press, Cambridge).

Gutbrod, T., M. Bayer, A. Forchel, J. P. Reithmaier, T. L. Reinecke, S. Rudin, and P. A. Knipp, 1998, Phys. Rev. B **57**, 9950.

Hadley, P., M. R. Beasley, and K. Wiesenfeld, 1988, Phys. Rev. B **38**, 8712.

Hadzibabic, Z., P. Krger, M. Cheneau, B. Battelier, and J. Dalibard, 2006, Nature (London) **441**, 1118.

Hanamura, E., and H. Haug, 1977, Phys. Rep. **33**, 209.

Hanbury Brown, R., and R. Q. Twiss, 1956, Nature (London) **178**, 1046.

Hansen, J. B., and P. E. Lindelof, 1984, Rev. Mod. Phys. **56**, 431.

Haug, H., 1969, Phys. Rev. **184**, 338.

Haug, H., and H. Haken, 1967, Z. Phys. A: Hadrons Nucl. **204**, 262.

Haug, H., and A. Jauho, 2008, *Quantum Kinetics in Transport and Optics of Semiconductors*, 2nd ed. (Springer, Berlin).

Hohenberg, P., 1967, Phys. Rev. **158**, 383.

Hopfield, J. J., 1958, Phys. Rev. **112**, 1555.

Houdré, R., C. Weisbuch, R. P. Stanley, U. Oesterle, P. Pellandini, and M. Ilegems, 1994, Phys. Rev. Lett. **73**, 2043.

Huang, R., F. Tassone, and Y. Yamamoto, 2000, Phys. Rev. B **61**, R7854.

Huang, R., Y. Yamamoto, R. André, J. Bleuse, M. Muller, and H. Ulmer-Tuffigo, 2002, Phys. Rev. B **65**, 165314.

Imamoglu, A., R. J. Ram, S. Pau, and Y. Yamamoto, 1996, Phys. Rev. A **53**, 4250.

Inoue, J.-i., T. Brandes, and A. Shimizu, 2000, Phys. Rev. B **61**,

2863.
Inouye, S., T. Pfau, S. Gupta, A. P. Chikkatur, A. Görlitz, D. E. Pritchard, and W. Ketterle, 1999, Nature (London) **402**, 641.
Kaitouni, R. I., O. El Daif, A. Baas, M. Richard, T. Paraiso, P. Lugan, T. Guillet, F. Morier-Genoud, J. D. Ganiere, J. L. Staehli, V. Savona, and B. Deveaud, 2006, Phys. Rev. B **74**, 155311.
Kasprzak, J., M. Richard, A. Baas, B. Deveaud, R. André, J. P. Poizat, and L. S. Dang, 2008, Phys. Rev. Lett. **100**, 067402.
Kasprzak, J., *et al.*, 2006, Nature (London) **443**, 409.
Kavokin, A., G. Malpuech, and M. Glazov, 2005, Phys. Rev. Lett. **95**, 136601.
Kavokin, A., G. Malpuech, P. G. Lagoudakis, J. J. Baumberg, and K. Kavokin, 2003, Phys. Status Solidi A **195**, 579.
Kavokin, K. V., I. A. Shelykh, A. V. Kavokin, G. Malpuech, and P. Bigenwald, 2004, Phys. Rev. Lett. **92**, 017401.
Keeling, J., F. Marchetti, M. Szymanska, and P. Littlewood, 2007, Semicond. Sci. Technol. **22**, R1.
Keldysh, L., and A. N. Kozlov, 1968, Sov. Phys. JETP **27**, 521.
Kena-Cohen, S., M. Davanco, and S. R. Forrest, 2008, Phys. Rev. Lett. **101**, 116401.
Ketterle, W., and N. J. van Druten, 1996, Phys. Rev. A **54**, 656.
Khalatnikov, I. M., 1965, *An Introduction to the Theory of Superfluidity* (Benjamin, New York).
Khurgin, J. B., 2001, Solid State Commun. **117**, 307.
Kim, N. Y., C.-W. Lai, S. Utsunomiya, G. Roumpos, M. Fraser, H. Deng, T. Byrnes, P. Recher, N. Kumada, T. Fujisawa, and Y. Yamamoto, 2008, Phys. Status Solidi B **245**, 1076.
Kosterlitz, J., and D. Thouless, 1972, J. Phys. C **5**, L124.
Kosterlitz, J., and D. Thouless, 1973, J. Phys. C **6**, 1181.
Kozuma, M., Y. Suzuki, Y. Torii, T. Sugiura, T. Kuga, E. W. Hagley, and L. Deng, 1999, Science **286**, 2309.
Krizhanovskii, D. N., D. Sanvitto, I. A. Shelykh, M. M. Glazov, G. Malpuech, D. D. Solnyshkov, A. Kavokin, S. Ceccarelli, M. S. Skolnick, and J. S. Roberts, 2006, Phys. Rev. B **73**, 073303.
Kuhn, T., 1997, in *Theory of Transport Properties of Semiconductor Nanostructures*, edited by E. Scholl (Springer, New York), p. 113.
Kuwata-Gonokami, M., S. Inouye, H. Suzuura, M. Shirane, R. Shimano, T. Someya, and H. Sakaki, 1997, Phys. Rev. Lett. **79**, 1341.
Lagoudakis, K. G., M. Wouters, M. Richard, A. Baas, I. Carusotto, R. André, L. S. Dang, and B. Deveaud-Pledran, 2008, Nat. Phys. **4**, 706.
Lai, C., N. Kim, S. Utsunomiya, G. Roumpos, H. Deng, M. Fraser, T. Byrnes, P. Recher, N. Kumada, T. Fujisawa, and Y. Yamamoto, 2007, Nature (London) **450**, 529.
Landau, L. D., and E. M. Lifshitz, 1987, *Fluid Mechanics* (Pergamon, Oxford).
Laussy, F. P., G. Malpuech, A. Kavokin, and P. Bigenwald, 2004, Phys. Rev. Lett. **93**, 016402.
Laussy, F. P., I. A. Shelykh, G. Malpuech, and A. Kavokin, 2006, Phys. Rev. B **73**, 035315.
Lauwers, J., A. Verbeure, and V. A. Zagrebnov, 2003, J. Phys. A **36**, L169.
Lax, M., 1967, IEEE J. Quantum Electron. **3**, 37.
Lidzey, D. G., D. D. C. Bradley, M. S. Skolnick, T. Virgili, S. Walker, and D. M. Whittaker, 1998, Nature (London) **395**, 53.
Lidzey, D. G., D. D. C. Bradley, T. Virgili, A. Armitage, M. S. Skolnick, and S. Walker, 1999, Phys. Rev. Lett. **82**, 3316.
Littlewood, P. B., P. R. Eastham, J. M. J. Keeling, F. M. Marchetti, B. D. Simon, and M. H. Szymanska, 2004, J. Phys.: Condens. Matter **16**, S3597, and references therein.
Madelung, O., 1996, *Introduction to Solid-State Theory* (Springer, Berlin).
Malpuech, G., A. Kavokin, A. Di Carlo, and J. J. Baumberg, 2002, Phys. Rev. B **65**, 153310.
Malpuech, G., Y. G. Rubo, F. P. Laussy, P. Bigenwald, and A. V. Kavokin, 2003, Semicond. Sci. Technol. **18**, S395.
Mermin, N. D., and H. Wagner, 1966, Phys. Rev. Lett. **17**, 1133; **17**, 1307(E) (1966).
Muller, M., J. Bleuse, R. André, and H. Ulmer-Tuffigo, 1999, Physica B **272**, 476.
Negoita, V., D. W. Snoke, and K. Eberl, 1999, Appl. Phys. Lett. **75**, 2059.
Nozieres, P., 1995, in *Bose-Einstein Condensation*, edited by A. Griffin, D. W. Snoke, and S. Stringari (Cambridge University Press, Cambridge), Vol. 15A.
Obert, M., J. Renner, A. Forchel, G. Bacher, R. Andre, and D. L. S. Dang, 2004, Appl. Phys. Lett. **84**, 1435.
Orzel, C., A. K. Tuchman, M. L. Fenselau, M. Yasuda, and M. A. Kasevich, 2001, Science **291**, 2386.
Ozeri, R., N. Katz, J. Steinhauer, and N. Davidson, 2005, Rev. Mod. Phys. **77**, 187.
Pau, S., G. Björk, H. Cao, E. Hanamura, and Y. Yamamoto, 1996, Solid State Commun. **98**, 781.
Pau, S., G. Björk, J. Jacobson, H. Cao, and Y. Yamamoto, 1995, Phys. Rev. B **51**, 7090.
Pau, S., J. Jacobson, G. Bjrk, and Y. Yamamoto, 1996, J. Opt. Soc. Am. B **13**, 1078.
Pawlis, A., A. Khartchenko, O. Husberg, D. J. As, K. Lischka, and D. Schikora, 2002, Solid State Commun. **123**, 235.
Pedri, P., L. Pitaevskii, S. Stringari, C. Fort, S. Burger, F. S. Cataliotti, P. Maddaloni, F. Minardi, and M. Inguscio, 2001, Phys. Rev. Lett. **87**, 220401.
Penrose, O., and L. Onsager, 1956, Phys. Rev. **104**, 576.
Pethick, C. J., and H. Smith, 2001, *Bose-Einstein Condensation in Dilute Gases* (Cambridge University Press, Cambridge).
Piermarocchi, C., F. Tassone, V. Savona, A. Quattropani, and P. Schwendimann, 1996, Phys. Rev. B **53**, 15834.
Pitaevskii, L. P., and S. Stringari, 2003, *Bose Einstein Condensation* (Clarendon, Oxford).
Porras, D., C. Ciuti, J. J. Baumberg, and C. Tejedor, 2002, Phys. Rev. B **66**, 085304.
Porras, D., and C. Tejedor, 2003, Phys. Rev. B **67**, 161310.
Posazhennikova, A., 2006, Rev. Mod. Phys. **78**, 1111.
Reitzenstein, S., C. Hofmann, A. Gorbunov, M. Strauss, S. H. Kwon, C. Schneider, A. Loffler, S. Hofling, M. Kamp, and A. Forchel, 2007, Appl. Phys. Lett. **90**, 251109.
Renucci, P., T. Amand, X. Marie, P. Senellart, J. Bloch, B. Sermage, and K. V. Kavokin, 2005, Phys. Rev. B **72**, 075317.
Richard, M., J. Kasprzak, R. Romestain, R. Andre, and L. S. Dang, 2005, Phys. Rev. Lett. **94**, 187401.
Risken, H., 1984, *The Fokker-Planck Equation: Methods of Solutions and Applications* (Springer, Berlin).
Rochat, G., C. Ciuti, V. Savona, C. Piermarocchi, A. Quattropani, and P. Schwendimann, 2000, Phys. Rev. B **61**, 13856.
Roumpos, G., S. Hoefling, A. Forchel, and Y. Yamamoto, 2009, APS March Meeting (unpublished), Paper No. H1600010.
Roumpos, G., C. W. Lai, T. C. H. Liew, Y. G. Rubo, A. V. Kavokin, and Y. Yamamoto, 2009, Phys. Rev. B **79**, 195310.
Sarchi, D., and V. Savona, 2006, e-print arXiv:cond-mat/0411084.
Sarchi, D., and V. Savona, 2007a, Phys. Rev. B **75**, 115326.

Sarchi, D., and V. Savona, 2007b, Solid State Commun. **144**, 371.
Sarchi, D., and V. Savona, 2008, Phys. Rev. B **77**, 045304.
Sarchi, D., P. Schwendimann, and A. Quattropani, 2008, Phys. Rev. B **78**, 073404.
Savvidis, P. G., J. J. Baumberg, R. M. Stevenson, M. S. Skolnick, D. M. Whittaker, and J. S. Roberts, 2000, Phys. Rev. Lett. **84**, 1547.
Schmitt-Rink, S., D. S. Chemla, and D. A. B. Miller, 1985, Phys. Rev. B **32**, 6601.
Schouwink, P., H. V. Berlepsch, L. Dhne, and R. F. Mahrt, 2001, Chem. Phys. Lett. **344**, 352.
Schwendimann, P., and A. Quattropani, 2008, Phys. Rev. B **77**, 085317.
Shelykh, I. A., G. Malpuech, and A. V. Kavokin, 2005, Phys. Status Solidi A **202**, 2614.
Shi, H., and A. Griffin, 1998, Phys. Rep. **304**, 1.
Shimada, R., J. Xie, V. Avrutin, U. Ozgur, and H. Morkoc, 2008, Appl. Phys. Lett. **92**, 011127.
Smerzi, A., S. Fantoni, S. Giovanazzi, and S. R. Shenoy, 1997, Phys. Rev. Lett. **79**, 4950.
Solnyshkov, D., I. Shelykh, M. Glazov, G. Malpuech, T. Amand, P. Renucci, X. Marie, and A. Kavokin, 2007, Semiconductors **41**, 1080.
Stamper-Kurn, D. M., A. P. Chikkatur, A. Görlitz, S. Inouye, S. Gupta, D. E. Pritchard, and W. Ketterle, 1999, Phys. Rev. Lett. **83**, 2876.
Szymanska, M. H., J. Keeling, and P. B. Littlewood, 2006, Phys. Rev. Lett. **96**, 230602.
Szymanska, M. H., P. B. Littlewood, and B. D. Simons, 2003, Phys. Rev. A **68**, 013818.
Takada, N., T. Kamata, and D. D. C. Bradley, 2003, Appl. Phys. Lett. **82**, 1812.
Tartakovskii, A. I., M. Emam-Ismail, R. M. Stevenson, M. S. Skolnick, V. N. Astratov, D. M. Whittaker, J. J. Baumberg, and J. S. Roberts, 2000, Phys. Rev. B **62**, R2283.
Tassone, F., C. Piermarocchi, V. Savona, A. Quattropani, and P. Schwendimann, 1996, Phys. Rev. B **53**, R7642.
Tassone, F., C. Piermarocchi, V. Savona, A. Quattropani, and P. Schwendimann, 1997, Phys. Rev. B **56**, 7554.
Tassone, F., and Y. Yamamoto, 1999, Phys. Rev. B **59**, 10830.
Tassone, F., and Y. Yamamoto, 2000, Phys. Rev. A **62**, 063809.
Tawara, T., H. Gotoh, T. Akasaka, N. Kobayashi, and T. Saitoh, 2004, Phys. Rev. Lett. **92**, 256402.
Tilley, D. R., and J. Tilley, 1990, *Superfluidity and Superconductivity* (Hilger, New York).
Tran Thoai, D. B., and H. Haug, 2000, Solid State Commun. **115**, 379.
Tsintzos, S. I., N. T. Pelekanos, G. Konstantinidis, Z. Hatzopoulos, and P. G. Savvidis, 2008, Nature (London) **453**, 372.
Utsunomiya, S., L. Tian, G. Roumpos, C. W. Lai, N. Kumada, T. Fujisawa, M. Kuwata-Gonokami, A. Loffler, S. Hofling, A. Forchel, and Y. Yamamoto, 2008, Nat. Phys. **4**, 700.
Weihs, G., H. Deng, R. Huang, M. Sugita, F. Tassone, and Y. Yamamoto, 2003, Semicond. Sci. Technol. **18**, S386.
Weisbuch, C., M. Nishioka, A. Ishikawa, and Y. Arakawa, 1992, Phys. Rev. Lett. **69**, 3314.
Wouters, M., and I. Carusotto, 2007, Phys. Rev. Lett. **99**, 140402.
Wouters, M., and V. Savona, 2009, Phys. Rev. B **79**, 165302.
Yamamoto, Y., G. Björk, K. Igeta, and Y. Horikoshi, 1989, in *Coherence and Quantum Optics VI*, edited by R. Loudon, J. H. Eberly, L. Mandel, and E. Wolf (Plenum, New York), p. 1249.
Yang, C. N., 1962, Rev. Mod. Phys. **34**, 694.
Yeh, P., 2005, *Optical Waves in Layered Media* (Wiley, Hoboken).